論文 / 著書情報
Article / Book Information

題目(和文)	フレネルゾーン数を指標として高周波の局所性を組み込んだ電磁波散乱問題の数値解析法に関する研究
Title(English)	Numerical Analyses of Electromagnetic Scattering Considering High Frequency Locality in Terms of Fresnel Zone Number Criteria
著者(和文)	小濱臣将
Author(English)	Takayuki Kohama
出典(和文)	学位:博士(工学), 学位授与機関:東京工業大学, 報告番号:甲第10149号, 授与年月日:2016年3月26日, 学位の種別:課程博士, 審査員:安藤 真,廣川 二郎,高田 潤一,西方 敦博,阪口 啓,Matteo Albani
Citation(English)	Degree:Doctor (Engineering), Conferring organization: Tokyo Institute of Technology, Report number:甲第10149号, Conferred date:2016/3/26, Degree Type:Course doctor, Examiner:,,,,,
学位種別(和文)	博士論文
Type(English)	Doctoral Thesis

Doctoral Dissertation

Numerical Analyses of Electromagnetic Scattering Considering High Frequency Locality in Terms of Fresnel Zone Number Criteria

February, 2016

Under the supervision of

Professor Makoto Ando

Presented by

Takayuki Kohama

Department of Electrical and Electronic Engineering
Tokyo Institute of Technology

Abstract

Computational costs for electromagnetic scattering analyses by the Physical Optics (PO) or the Method of Moments (MoM) become extremely heavier in higher frequency. In this dissertation, some techniques to embed the high frequency locality of scattering phenomena into PO or MoM, named "Localization method," are studied for the reduction of the computational loads. The scatterer surface is localized and truncated according to the Fresnel zone number criteria and the localization leads to suppression of frequency dependence of computational costs without degradation of computational accuracy. In Chapter 2, the fundamental property of Fresnel zone localization is investigated. In order to suppress the truncation error, a raised cosine function, named "EYE function," whose argument is also the Fresnel zone number is introduced. From Chapter 3 to Chapter 5, some specific localization methods are presented and numerically examined for 3-dimensional scattering analysis of simple structures such as a rectangular plate or a part of sphere. In Chapter 3, localization of radiation integral is discussed. In order to define the local area around edge diffraction points, the modified surface-normal vector is adopted. In Chapter 4, frequency-independent segmentation in PO radiation integral, which consists of the localization method and the adaptive sampling, is discussed. This technique is at first applied to 2-D problem, and then, the expansion to 3-D problem is examined. In Chapter 5, MoM analysis of the localized scatterer, named "Local-MoM," is discussed. It is proposed that the square root of EYE function should be applied to a source side and an observer side. Local-MoM enables a MoM analysis for very large scatterer with $112\lambda \times 112\lambda$ which cannot be analyzed by the standard MoM due to the memory capacity of 32GB. In Chapter 6, the summary and future works are presented.

Contents

Chapter 1 Introduction

1.1 Representative Methods for Scattering Analysis

Electromagnetic scattering problem and its analysis have been important research subjects in various areas such as antennas and propagation, RADAR (Radio Detecting and Ranging), electromagnetic compatibility (EMC), wireless communication, geoscience and remote sensing, and so on. Scattering analysis is of course to analyze a scattering phenomenon or a scattered field in electromagnetics. Methods for scattering analysis are mainly classified into two categories: high frequency approximations (HFA) and numerically-accurate methods. The latter one is also called low frequency methods. The classification of the representative methods for scattering analysis is summarized in Fig. 1.1

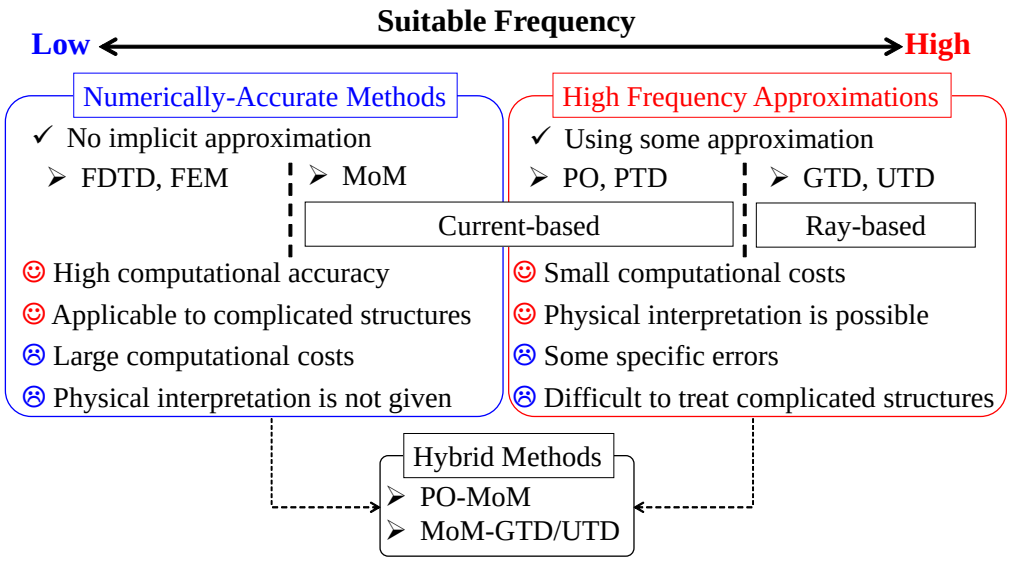

Figure 1.1: Representative methods for scattering analysis.

1.1.1 High Frequency Approximation (HFA)

HFA itself is mainly divided into two ways: current-based methods and ray-based methods. The physical optics (PO) approximation is one of the representative current-based methods.

The PO is the method based on Kirchhoff approximation. When Kirchhoff introduced an integral formula to express a scattering (diffraction) from an aperture, he assumed that

a scattered field was derived by an integration of equivalent sources on the aperture. And he used the approximation that equivalent sources can be directly given by an incident field [1.2]. Note that this approximation can be traced back to Huygens-Fresnel principle. Huygens' Principle published in 1690 stated that every point where a primary spherical wave reaches without any disturbance becomes a secondary source of spherical wave. In 1818, Fresnel extended his principle so that a diffraction wave was covered. Fresnel replaced Huygens' isolated spherical waves by purely periodic trains of them and made use of the principle of interference [1.3, 4].

The basic idea of PO itself was firstly proposed by Macdonald in 1912 [1.5]. Formulations and explanations of PO were reinforced through a variety of researches and are summarized well in some professional books [1.6–8]. In PO, a scattered field is given by an integration of induced currents on an illuminated side of the scatterer. In most of the cases the scatterer is regarded as PEC and the currents is given by $2\hat{n} \times \boldsymbol{H}_i$ where $\hat{n}$ is an unit vector normal to the scatterer surface and $\boldsymbol{H}_i$ is an incident magnetic field. PO currents for dielectric materials are also known [1.9].

PO provides reasonable results of radiation patterns of reflector antennas in the angles near main beam direction, but it was pointed out that the accuracy in shadow region is not good [1.10]. A main cause is that PO doesn't take the edge effects into account. In 1955, the physical theory of diffraction (PTD) [1.11] was proposed by Ufimtsev as an extension of PO. He introduced non-uniform edge currents named as fringe wave (FW) currents near the edge of the scatterer. It led to the enhancement of accuracy of radiation pattern. Because of these historical background, PO and PTD have often appeared in radiation pattern analyses of reflector antennas and radar cross section (RCS) [1.12–14].

Ray-based methods are based on ray optics which was already proposed before Christ and have been evolved through the studies and designs of lens. Ray optics is also called as Geometrical Optics (GO). In ray optics, propagation of a light is regarded as ray, in other words, a particle. Until Young's work, ray optics had treated only incident field and phenomena following the Snell's law, that is, reflection and refraction. So the sum of these three components is sometimes called as GO components. In 1802, Young defined a diffraction which is a component of the scattered field radiated from the edge of scatterer [1.15]. Maggi [1.16] and Rubinowicz [1.17] independently provided an idea that the Kirchhoff's integral can be decomposed into a GO component and a diffraction component and that diffraction comes from every point of the boundary of the aperture.

In the 1940s and 1950s, Luneburg and Kline pointed out that GO term corresponds to the leading terms of the asymptotic expansion in inverse powers of the wavenumber k [1.18, 19]. From the 1950s to 1960s, Keller proposed and developed the geometrical theory of diffraction (GTD) as an extension of GO. He derived diffraction coefficients by applying

the generalization of the Luneburg-Kline expansion to the Sommerfeld's solution. According to GTD's idea, diffraction may be regarded as rays arising from edges, wedges, corners, tips, smooth curved surfaces, and so on. He provided diffraction coefficients for edges and wedges [1.21] although these coefficient yields divergence at incident and reflection shadow boundaries (RSB/ISB), caustics, and focuses. After Keller's formulation, variety techniques have been proposed to overcome GTD's difficulties. The uniform asymptotic theory of diffraction (UAT) [1.22–24] and the uniform geometrical theory of diffraction (UTD) [1.26] are the representative methods. They were at first introduced to obtain edge or wedge diffraction coefficients and they have currently been extended for various diffraction phenomena although all of the difficulties have not necessarily been eliminated. These ray optics techniques are utilized mainly in analyses of radio propagation environment as well as RCS prediction in terms of ray tracing method [1.27–29]. Recently, the shooting and bouncing rays (SBR) method [1.30, 31] has become very popular as efficient technique for ray tracing [1.32, 33].

In a sense that both of the GO and diffraction components correspond to the leading term in inverse powers of k, ray-based methods are interpreted as one of HFA. On the other hand, the reason why PO and PTD are also classified with HFA is that PO's currents approach the exact induced currents when the size of scatterer becomes larger and the curvature of each point on the scatterer becomes smaller in terms of wavelength, that is, frequency gets higher. One advantage of HFA is that physical interpretation of a field can be given. HFA provides information of which component is dominant, where it comes from, and how much the contribution of it is. Another advantage is that the frequency dependence of computational costs in HFA is very small. That of ray-based methods is usually independent of frequency f while PO and PTD has f^2 dependence since they include numerical surface integrals. However this dependence is much smaller than that of the numerically-accurate methods as mentioned later. Because of these advantages, HFA is regarded as powerful tools for scattering analysis even now although HFA is classical method and some disadvantages such as inaccuracy and inapplicability for some of structures have not been overcome yet.

1.1.2 Numerically-Accurate Methods (Low Frequency Methods)

The numerically-accurate methods are those to solve Maxwell's Equations without any implicit approximations unlike HFA. The Method of Moments (MoM) [1.34], Finite Element Method (FEM) [1.35, 36], and Finite-Difference Time-Domain (FDTD) [1.37, 38] are the representative methods. They have been significantly developed with the growth of computer performances.

The MoM is a method to solve electromagnetic boundary or volume integral equations and is based on the field equivalence theorem. Among them, the MoM is the most suitable for radiation and scattering problem because it is able to treat a open region having infinite volume of space without any assumption. In scattering analysis by the MoM, unknown induced currents are at first assumed on the surface of the scatterer and are obtained by solving a linear equation. These MoM currents play the similar role as PO's currents. That is, radiation integrals of induced currents give a scattered field.

The FDTD is a method to solve Maxwell's time-dependent vector-rotation equations (Faraday's law and Ampere's law with Maxwell's addition) using finite difference. In the FDTD, the electromagnetic field in a finite volume is at first sampled at distinct points in a space and time domain. Next, the field is updated by using the two out of four of Maxwell's equations. The FDTD is suitable for waveguide problems, wave propagation in complex dielectrics, and EMC problems. However, in order to deal with open-region radiation and scattering problems, some special treatments (assumptions) are required: absorbing boundary conditions [1.39, 40] or perfectly matched layer (PML) formulations [1.41, 42] and so on. This is because analysis domain in the FDTD must be a finite volume of space. Moreover, these treatments are not perfect in the sense that a very small reflection from the boundary is unavoidable from the theoretical point of view. Note that many techniques to suppress the reflection have been proposed, such as the convolutional PML [1.43] and the higher-order PML [1.44]. Therefore it is currently recognized that the applicability of FDTD to radiation and scattering problems is high enough.

The FEM was originally proposed and developed in the area of structural mechanics [1.45]. Later it was imported into analysis of electromagnetic fields [1.46]. The FEM is a method to solve boundary value problems for partial differential equations. In the FEM, the partial differential equations are at first transformed to equivalent variational or weak forms. After that, coefficients for elements are obtained by solving a linear equation. The FEM is often used in the frequency domain analysis of the electromagnetic field distribution in complex, closed regions such as cavities and waveguides. In common with the FDTD, the solution domain must be a finite volume of space. So the special treatments such as PML or radiation boundaries are necessary.

The reason why the numerically-accurate methods are also called as low frequency methods is that they are not suitable for high frequency problems in terms of computational costs. The computational costs such as required time and memory capacity are dominated by the value of $L = kR_s$ where R_s is the radius of the smallest sphere circumscribing the analysis domain. The costs are usually proportional to L^3 to L^6. If the physical size of the problem is fixed and only frequency f gets higher, L simply increases in proportional to f. It leads to explosive increase in computational costs for higher frequency So the

numerically-accurate methods were restricted to the problem with less than $L \sim 100$ until the early of 1990s [1.47].

That difficulty has been overcome to some extent with the rapid development of computer performances such as operating frequency and the number of cores of central processing unit (CPU), capacity of random access memory (RAM), and bandwidth of memory bus. Recently, graphics processing unit (GPU) computing and parallel computing have also been adopted to accelerate numerical analysis. In addition to that, a variety of fast and efficient techniques have been developed in the 1990s and 2000s. For instance, the fast multipole method (FMM) [1.48], multilevel fast-multipole method (MLFMM) [1.49], and the characteristic basis function method (CBFM) [1.50] have proposed to enhance the efficiency of MoM analysis. Through these developments, many commercial simulator to realize the numerically-accurate methods for practical problems have been released. Currently, the commercial simulators are widely and frequently used by many researchers and engineers. However, the intrinsic disadvantage of the numerically-accurate methods has not been overcome yet. That is, the physical interpretation is still impossible for the results obtained by these methods.

1.1.3 Hybrid Methods and Emergence of Fresnel Zone Number Criterion

Together with the development of the HFA and the numerically-accurate methods, hybrid methods between them have attracted attention among researchers. Most of the hybrid methods are those between the MoM and some of HFA. MoM-GTD was one of the first hybrid methods [1.51]. In the MoM-GTD, complicated structures or vicinities of antenna excitations are analyzed by MoM and the other contributions are taken into account by using GTD. As researches on UTD progressed, MoM-UTD was also proposed and developed [1.52–54]. PO-MoM is another way to reduce the number of unknowns in MoM [1.55–58]. A scatterer is divided into a PO region and an MoM region and then unknowns are assumed only on the MoM region. These hybrid methods are now available in some of commercial simulators such as FEKO®[1.59].

However, to the best knowledge of the author of this dissertation, there is no explicit criterion of how to select whether HFA or MoM is applied to a part of structures, although hybrid methods are still studied actively as [1.60, 61]. Fig. 1.2 shows the concept of hybrid methods cited from [1.52]. The scatterer surface is decomposed into three regions with different analysis methods; MoM, PO, and UTD. However, a criterion to decompose it uniquely and specifically has not been given in any papers already referred.

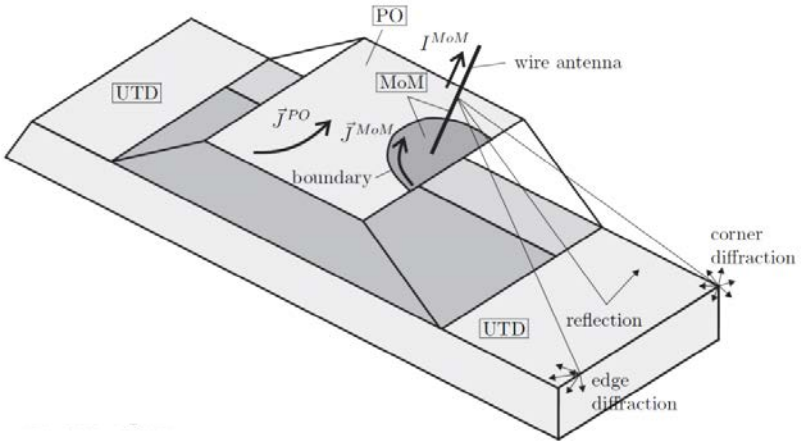

Figure 1.2: Treatment of scatterer in the conventional hybrid methods (Figure 1 of [1.52] is cited).

The first trial to give the criterion was done by Shijo and Ito [1.62, 63]. They proposed the Fresnel zone number criterion to implement the high frequency locality into the MoM analysis. Fresnel zone number itself is used to evaluate path losses of radio propagation in a long-distance wireless communication [1.65]. The use of Fresnel zone number in the calculation of PO or MoM can be traced back to the visualization of scattering phenomena [1.64]. In [1.64], the Fresnel zone number was utilized to evaluate how large an integration area is necessary for convergence of brightness of scattered field. The Fresnel zone number criterion again appeared in the discussion of the large-size local-domain basis function for the method of moments [1.66]. The relationship between Fresnel zone number and the degree of sparsity of impedance matrices was investigated in this paper.

The papers of [1.62, 63] gave the criterion to determine an appropriate boundary between MoM and PO regions using Fresnel zone number which is the function of source and observer position, and frequency. In addition to that, the novel MoM named "Local-MoM" was proposed in these papers. In the Local-MoM, the scatterer is at first localized and truncated based upon the Fresnel zone number criterion. Next, unknown currents are assumed only on the localized scatterer and are obtained by the MoM analysis. Finally, scattered fields are obtained by radiation integrals with an appropriate windowing function. In [1.62, 63], the fundamental idea of Fresnel zone localization was shown and the PO-MoM and Local-MoM with Fresnel zone number criterion were applied to two-dimensional problems.

One of the advantages of Fresnel zone number criterion is that physical interpretation is available because the localized area corresponds to a certain scattering center such as a reflection or diffraction point. Another advantage is reduction in frequency dependence of

computational costs due to truncation. The frequency dependence of electrical size (unit: wavelength squared) of truncated (localized) area is suppressed unlike that of original problems and it leads to a great reduction in computational cost as frequency gets higher. Moreover, this Fresnel zone number criterion may become a bridge between HFA and low frequency methods as shown in Fig. 1.3. According to the Fresnel zone number criterion, localized analysis areas cover the whole of surface when frequency is low enough. As frequency becomes higher, the localized areas shrink and become some of portions of surface. Finally, the localized areas become a some of specific points. This characteristic means that the localization method based on the Fresnel zone number criterion approaches normal MoM with lower frequency. On the other hand, the scatterer will be treated as the localized one in higher frequency, that is, a scattered field depends on local properties of scattering centers such as unit normal vectors or curvatures as idea of GTD or UTD. As frequency changes, the treatment of scatterer also will change automatically and smoothly due to the Fresnel zone number criteria.

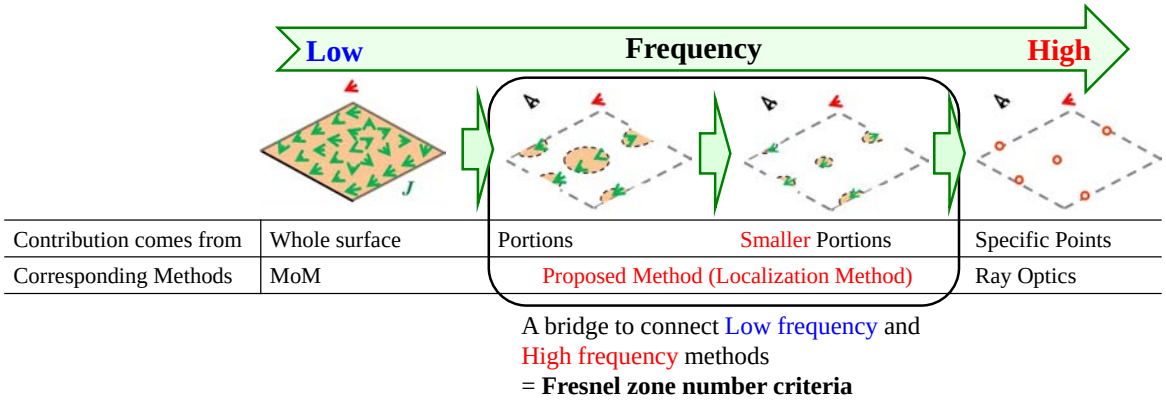

Figure 1.3: A role of Fresnel zone number criteria: localization method may become a bridge to connect low frequency and high frequency method.

1.2 Objectives

The localization techniques based upon the Fresnel zone number criteria may be a breakthrough in scattering analysis for the electrically-large scatterer in terms of the reduction of computational costs. Moreover, the Fresnel zone number criteria may realize a novel numerically-accurate method where the physical interpretation of obtained results is possible. In order to realize these, the problems left in the works of [1.62, 63] must be resolved. For instance, the localization method were not applied to three-dimensional problems in their works. The theoretical investigation on the Fresnel zone number criteria were not

conducted. Frequency dependence of computational costs must be discussed quantitatively. With these in mind, the applicability of several localization methods is checked for scattering problems of some simple structures such as a rectangular plate and a part of sphere. The localization methods are basically suitable for smooth surfaces, so the discussion on rough surface is out of this dissertation. Only a scattered field at infinite distance (far field) is discussed in this dissertation.

The objectives of this study are as follows:

- To investigate physical meanings and theoretical properties of Fresnel zone number criteria.
- To propose and establish a good application way of localization methods to three-dimensional problems.
- To check numerical accuracy and its characteristics of these proposed methods.
- To check frequency dependence of computational costs for these proposed methods.

1.3 Outline of Remaining Chapters

The outline of the remaining chapters in shown in Fig. 1.4

In Chapter 2, the physical meaning of localization method and Fresnel zone number criteria is given. The relationship between the stationary phase method and the localization method is explained. The importance of windowing function is also reviewed. It is proposed that Fresnel zone number is used as the argument of windowing function. The error due to localization is evaluated numerically and analytically. Other properties such as frequency dependence of computational costs is analytically derived .

In Chapter 3, a localization technique for radiation integrals is presented. The treatment of edge or corner diffraction points in terms of localization technique is explained as well as that of overlapped local areas. Numerical results for a rectangular plate and a part of sphere are presented. This chapter together with Chapter 2 provides the basis of the other chapters.

In Chapter 4, one method is shown, which realizes radiation integrals with the frequency-independent number of divisions by jointly using the Fresnel zone localization and adaptive sampling methods. Main numerical discussion is done for two-dimensional problems. Frequency dependence of computational time and accuracy is numerically checked. The extension to three-dimensional problems is also discussed.

In Chapter 5, the Local-MoM is extended for three-dimensional problems. The use of windowing function is reconsidered and application of windowing function to the inci-

dent field from the source is proposed. The implementation of Local-MoM into a MoM-based commercial simulator WIPL-D®[1.67]. Scattering analysis for electrically-very-large problems with reasonable accuracy is realized. Computational cost reduction, especially memory capacity saving, is confirmed.

In Chapter 6, conclusions of the thesis are given and future works are presented.

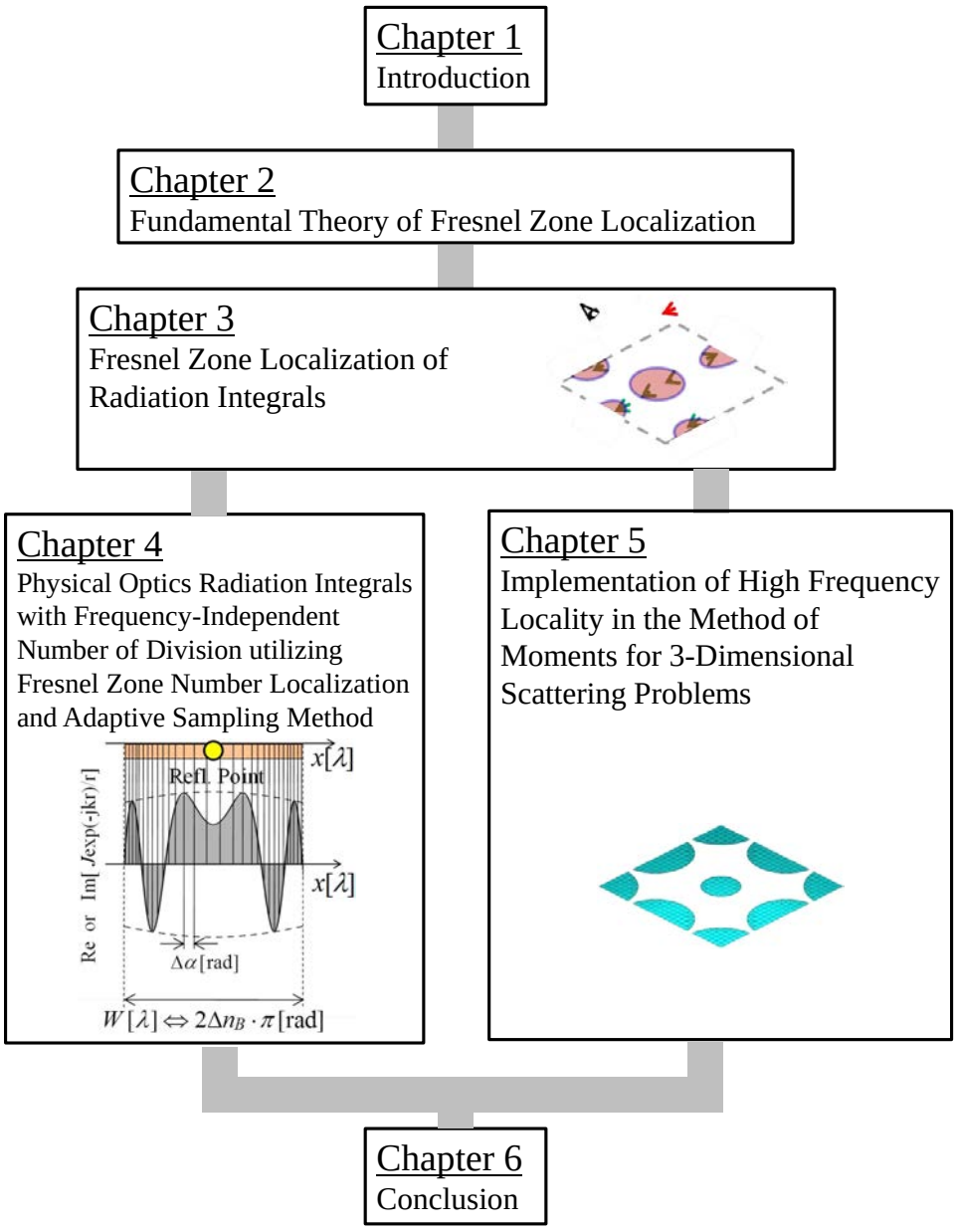

Figure 1.4: Outline of the thesis.

References

[1.1] J. J. Bowman, T. B. A. Senior, and P. L. E. Uslenghi, *Electromagnetic and Acoustic Scattering by Simple Shapes*, North-Holland Publishing Co., 1969.

[1.2] G. Kirchhoff, *Lectures on Mathematical Optics*, Part II, ed. L. Boltzmann, Teubner, Leopzig, 1891.

[1.3] A. Fresnel, "Lettre d'Augustin Fresnel a FrancoisArago sur l'influence du movement terrestre dans quelque phenomenes d'optique," Annales de chimic el de physique, 9, pp.55-66, 1818.

[1.4] A. Fresnel, "Memoir on the Diffraction of Light," *The Wave Theory of Light Memoirs by Huygens, Young and Fresnel*, American Book Company, pp.79-156, 1819.

[1.5] H. M. Macdonald "The Effect Produced by an Obstacle on a Train of Electric Waves," *Philosophical Transactions of the Royal Society of London*, Series A, Containing Papers of a Mathematical or Physical Character, vol. 212, pp. 299-337, 1912.

[1.6] S. Silver, *Microwave Antenna Theory and Design*, McGraw-Hill, New York, pp.148-158, 1949.

[1.7] R. F. Harrington, Time-Harmonic Electromagnetic Fields, pp.127-130, *McGraw-Hill*, New York. 1961

[1.8] C. A. Balanis, *Advanced Engineering Electromagnetics*, John Wiley and Sons, pp.338-346, 1989.

[1.9] S. R. Rengarajan, E. S. Gillespie, Jr., "Asymptotic approximations in radome analysis," *IEEE Transaction on Antennas and Propagation*, vol.36, no.3, pp.405-414, Mar. 1988.

[1.10] M. Ando, "Radiation pattern analysis of reflector antennas -Discussions and hybrid use of physical optics and aperture field integration method," *IEICE Transactions on Communications*, vol.88, no.5, pp.1790-1800, 2005.

[1.11] P. Y. Ufimtsev, "Elementary edge waves and the physical theory of diffraction," *Electromagnetics*, vol.11, iss.2, pp.125160, 1991.

[1.12] M. Ando, "Radiation pattern analysis of reflector antennas," *IEICE Transaction on Communication (Japanese Edition)*, J67-B, no.8, pp.853-860, Aug. 1984.

[1.13] T. Griesser, and C. A. Balanis. "Backscatter analysis of dihedral corner reflectors using physical optics and the physical theory of diffraction," *IEEE Transaction on Antennas and Propagation*, vol.35, no.10, pp.1137-1147, Oct. 1987

[1.14] L. Diaz, and T. Milligan, *Antenna Engineering Using Physical Optics: Practical CAD Techniques and Software*, Nonvood, MA, Artech House, 1996.

[1.15] T. Young, "The Bakerian lecture: On the theory of light and colours." *Philosophical transactions of the Royal Society of London*, vol.92, pp.12-48, 1802.

[1.16] G. A. Maggi, *Ann. Mathematica, part II*, vol.16, p.21, 1888

[1.17] A. Rubinowicz, "The Miyamoto-Wolf diffraction wave," *Progress in Optics*, vol.4, pp.201-240, 1965.

[1.18] R. K. Luneburg, *Mathematical Theory of Optics*, University of California Press. 1966

[1.19] M. Kline, "An asymptotic solution of Maxwell's equations." *Communications on Pure and Applied Mathematics*, vol. 4, pp.225-262, 1951

[1.20] A. Sommerfeld, Math. Ann., 47, 317.

[1.21] J. B. Keller, "Geometrical theory of diffraction," *Journal of the Optical Society of America*, vol.52, pp116-130, 1962.

[1.22] D. S. Ahluwalia, R. M. Lewis, and J. Boersma. "Uniform asymptotic theory of diffraction by a plane screen," *SIAM Journal on applied mathematics*, vol.16, pp.783-807, 1968.

[1.23] R. M. Lewis, and J. Boersma. "Uniform asymptotic theory of edge diffraction," *Journal of Mathematical physics*, vol.10, pp.2291-2305, 1969.

[1.24] D. S. Ahluwalia, "Uniform asymptotic theory of diffraction by the edge of a three-dimensional body," *SIAM Journal on Applied Mathematics*, vol.18, pp.287-301, 1970.

[1.25] S. W. Lee, and G. A. Deschamps. "A uniform asymptotic theory of electromagnetic diffraction by a curved wedge," *IEEE Transaction on Antennas and Propagation*, vol.24, pp.25-34, 1976.

[1.26] R. G. Kouyoumjian, and R. H. Pathak, "A uniform geometrical theory of diffraction for an edge in a perfectly conducting surface," *Proceedings of the IEEE*, vol.62, no.11, pp.1448-1461, Nov. 1974.

[1.27] K. R. Schaubach, N. J. Davis IV, and T. S. Rappaport. "A ray tracing method for predicting path loss and delay spread in microcellular environments," *42nd IEEE Vehicular Technology Conference*, pp.932-935, May 1992.

[1.28] R. A. Valenzuela, "A ray tracing approach to predicting indoor wireless transmission," *43rd IEEE Vehicular Technology Conference*, pp.214-218, May 1993.

[1.29] M. Porretta, P. Nepa, G. Manara, and F. Giannetti, "Location, Location, Location," *IEEE Vehicular Technology Magazine*, vol.3, no.2, pp.20-29, June 2008.

[1.30] S. L. H. Ling, and R. Chou, "Shooting and bouncing rays: Calculating the RCS of an arbitrarily shaped cavity," *IEEE Transaction on Antennas and Propagation*, vol. 37, no.2, pp.194-205, Feb. 1989.

[1.31] S. L. H. Ling, and R. Chou, "High-frequency RCS of open cavities with rectangular and circular cross sections," *IEEE Transaction on Antennas and Propagation*, vol. 37, no.5, pp.648-654, May 1989.

[1.32] A. Amornthipparat, H. Shirai, K. Yonezawa, T. Inoue, and Y. Nakamura, "Estimation of high frequency NLOS path loss in street-cell environment," *the Proceedings of 2008 International Conference on Communications and Electronics (ICCE)*, pp.336-340, June 2008.

[1.33] Y. Tao, H. Lin, and H. Bao, "GPU-Based Shooting and Bouncing Ray Method for Fast RCS Prediction," *IEEE Transaction on Antennas and Propagation*, vol.58, no.2, pp.494-502, Feb. 2010.

[1.34] R.F. Harrington, *Field Computation by Moment Methods*, IEEE Press, New York, 1993.

[1.35] J. Jin, *The Finite Element Method in Electromagnetics*, John Wiley and Sons, 1993.

[1.36] J. L. Volakis, A. Chatterjee, and L. C. Kempel, *Finite Element Method for Electromagnetics* IEEE Press, 1998.

[1.37] A. Taflove, and S. C. Hagness, *Computational Electrodynamics: The Finite-Difference Time-Domain Method*, Artech House, 3rd editon, 2005.

[1.38] K. Kunz, and R. Luebbers, *The Finite Difference Time Domain Method for Electromagnetics*, CRC Press, 1993.

[1.39] G. Mur, "Absorbing Boundary Conditions for the Finite-Difference Approximation of the Time-Domain Electromagnetic-Field Equations," *IEEE Transactions on Electromagnetic Compatibility*, vol. 23, no.4, pp.377-382, Nov. 1981.

[1.40] Z. P. Liao, H. L. Wong, B. P. Yang, and Y. F. Yuan, "A transmitting boundary for transient wave analysis," *Scientia Sinica*, vol.27, no.10, pp.1063-1076, 1984.

[1.41] J. P. Berenger, "A perfectly matched layer for the absorption of electromagnetic waves," *Journal of Computational Physics*, vol.114, no.2, pp.185-200, 1994.

[1.42] S. D. Gedney, "An anisotropic perfectly matched layer-absorbing medium for the truncation of FDTD lattices," *IEEE Transaction on Antennas and Propagation*, vol.44, no.12, pp.1630-1639, Dec. 1996.

[1.43] J. A. Roden, and S. D. Gedney, "Convolutional PML (CPML): An efficient FDTD implementation of the CFS-PML for arbitrary media." *Microwave and Optical Technology Letters*, vol.27, no.5, pp.334-338, 2000.

[1.44] D. Correia, and J. Jian-Ming, "On the development of a higher-order PML," *IEEE Transaction on Antennas and Propagation*, vol.53, no.12, pp.4157-4163, Dec. 2005.

[1.45] M. J. Turner, "Stiffness and deflection analysis of complex structures," *Journal of the Aeronautical Sciences*, vol. 23, pp. 805-824, 1956.

[1.46] M. V. K. Chari, and P. P. Silvester, *Finite Elements in Electrical and Magnetic Field Problems*, John Wiley & Sons, 1980.

[1.47] K. Umashankar, and A. Taflove, *Computational electromagnetics*, Artech House, 1993.

[1.48] R. Coifman, V. Rokhlin, and S. Wandzura, "The fast multipole method for the wave equation: a pedestrian prescription," *IEEE Antennas and Propagation Magazine*, vol.35, no.3, pp.7-12, June 1993

[1.49] J. M. Song, and W. C. Chew, "Multilevel fast-multipole algorithm for solving combined field integral equations of electromagnetic scattering," *Microwave and Optical Technology Letters*, Vol.10, No.1, pp.14-19, Sep. 1995.

[1.50] V. V. S. Prakash, and Raj Mittra, "Characteristic basis function method: A New Technique for Efficient Solution of Method of Moments Matrix Equations," *Microwave and Optical Technology Letters*, Vol.36, No.2, Jan. 2003.

[1.51] W. D. Burnside, C. L. Yu, and R. J. Marhefka, "A technique to combine the geometrical theory of diffraction and the moment method," *IEEE Transaction of Antennas and Propagatation*, vol.23, no.4, pp.551-558, July 1975.

[1.52] U. Jakobus, and F. M. Landstorfer, "A combination of current-and ray-based techniques for the efficient analysis of electrically large scattering problems," *Proceedings of 13th Annual Review of Progress in Applied Computational Electromagnetics*, Monterey, CA, pp. 748-755, Mar. 1997.

[1.53] H.-T. Chou, P. H. Pathak, and M. Hsu. "Extended uniform geometrical theory of diffraction solution for the radiation by antennas located close to an arbitrary, smooth, perfectly conducting, convex surface," *Radio Science* vol.32, no.4, pp.1297-1317, 1997.

[1.54] I. P. Theron, D. B. Davidson, and U. Jakobus, "Extensions to the hybrid method of moments/uniform GTD formulation for sources located close to a smooth convex surface," *IEEE Transaction on Antennas and Propagation*, vol.48, no.6, pp.940-945, Jun. 2000.

[1.55] C. S. Kim, and Y. Rahmat-Samii, "Low profile antenna study using the physical optics hybrid method (POHM)", *in the Digest of IEEE International Symposium on Antennas and Propagation (AP-S)*, vol. 29, pp.1350-1353, June 1991.

[1.56] R. E. Hodges, and Y. Rahmat-Samii, "Theory of physical optics hybrid method (POHM)," *in the Digest of IEEE International Symposium on Antennas and Propagation (AP-S)*, vol.3, pp.20-24, June 1994.

[1.57] U. Jakobus, and F.M. Landstorfer, "Improved PO-MM hybrid formulation for scattering from three-dimensional perfectly conducting bodies of arbitrary shape," *IEEE Transaction on Antennas and Propagation*, vol.43, no.2, pp.162-169, Feb. 1995.

[1.58] U. Jakobus, and F.M. Landstorfer, "Improvement of the PO-MoM hybrid method by accounting for effects of perfectly conducting wedges," *IEEE Transaction on Antennas and Propagation*, vol.43, no.10, pp.11231129, Oct. 1995.

[1.59] FEKO, "Numerical Methods," [online], available: https://www.feko.info/product-detail/numerical_methods

[1.60] Z.-L. Liu, and C.-F. Wang, "Efficient Iterative Method of Moments—Physical Optics Hybrid Technique for Electrically Large Objects," *IEEE Transaction on Antennas and Propagation*, vol.60, no.7, pp.3520-3525, July 2012.

[1.61] Z.-L. Liu, X. Wang, and C.-F. Wang, "Installed Performance Modeling of Complex Antenna Array Mounted on Extremely Large-Scale Platform Using Fast MoM-PO Hybrid Framework," *IEEE Transaction on Antennas and Propagation*, vol.62, no.7, pp.3852-3858, July 2014.

[1.62] T. Shijo, M. Oishi, Y. Katakai, N. Omaki, K. Yukimasa, L. Rodriguez, and M. Ando, "Application of the Locality Principle in the Method of Moments for Induced Currents or Fields in Electrically Large Scattering Problems," *IEICE Technical Report*, vol.106, no.561, AP2006-169, pp.109-112, Mar. 2007.

[1.63] K. Ito, T. Shijo, and M. Ando, "Fresnel zone criterion to implement locality in the method of moments and PO-MoM hybrid method for the reduction of unknowns," *IEICE Transaction on Electronics*, vol.E94-C, no.1, pp72-79, Jan. 2011.

[1.64] T. Shijo, T. Itoh, and M. Ando, "Visualization of high frequency diffraction based on physical optics," *IEICE Transaction on Electronics* vol.E87-C, no.9, pp.1607-1614, Sep. 2004.

[1.65] T. S. Rappaport, *Wireless Communication: Principal and Practice,* 1st Ed., Prentice Hall PTR, pp.89-99, 1996.

[1.66] T. Shijo, T. Hirano, and M. Ando, "Large-Size Local- Domain Basis Functions with Phase Detour and Fresnel Zone Threshold for Sparse Reaction Matrix in the Method of Moments," *IEICE Transaction on Electronics.*, Vol.E88-C, No.12, pp.2208-2215, Dec. 2005.

[1.67] WIPL-D, "WIPL-D -Electromagnetic Simulation Software," [online], available: http://www.wipl-d.com/

Chapter 2

Fundamental Theory of Fresnel Zone Localization

2.1 Introduction

A concept of Fresnel zone has been frequently and widely used to evaluate path losses due to a reflection from a ground, a knife edge diffraction by a moutain, a blocking effect by obstacles, and so on in a long-distance wireless communication [2.1]. Fresnel zone itself is a three-dimensional ellipsoidal volume and is defined around transmitter and receiver antennas. The size of Fresnel zone is expressed by the Fresnel zone number n as follows (See Fig. 2.1);

$$n = \frac{L_{SI} + L_{IO} - L_{SO}}{\lambda/2} \tag{2.1}$$

where λ is the wavelength. In many cases, $n = 1$ or 2 is chosen as the criterion to evaluate the path losses. That is, when there are obstacles within the 1st or 2nd Fresnel zone, it is interpreted that they disturb line of sight (LoS) propagation even if they are not located on the direct line path between transmitter and receiver antennas.

As shown in (2.1), Fresnel zone number is directly related with an optical path length from the source (S) to the observer (O) via a point of interest (I) (See Fig. 2.1). An optical path length itself is a key parameter in ray optics such as the geometrical theory of diffraction (GTD) [2.2] and uniform theory of diffraction (UTD) [2.3]. For instance, a reflection wave propagates along the shortest or longest path from a source to observer via a certain point on a surface of a scatterer. From a point of view of some theories of diffraction, an edge diffraction wave also propagates through the path with the local shortest or longest length via a certain point on a periphery of a scatterer.

On the other hand, the wave optics such as the physical optics (PO) [2.5, 6] originally does not put importance on a path length. It is when an asymptotic technique such as the stationary phase method (SPM) is applied to the integral (e.g. [2.7]) that the optical path length becomes important. It means that a surface integral form is approximated by a sum of point contribution from the scattering centers, namely, the stationary phase points (SPP) which correspond to reflection and edge diffraction points in terms of ray optics. Note that an optical path length has been a keyword in the result by the SPM as well as that by ray optics, but the term of Fresnel zone number had seldom appeared

in these discussions until the paper [2.8]. This is because only the (local) minimum (or maximum) length of optical path makes sense in these discussions, thus there was no need to translate a path length into the Fresnel zone number.

Asymptotic evaluation of radiation integral using Fresnel zone number was firstly conducted for a visualization of scattering phenomena in Shijo and Ito's paper [2.8]. In their work, they focused on not only the extreme values of path lengths (shortest or longest) but also on the path length difference from these. For instance, a reflection point looks the brightest and edge diffraction points looks the second brightest as shown in Fig. 2.2. Moreover the vicinity of these points also look brighter than the other area. In his paper, it was proposed that Fresnel zone number should be used as the criterion to evaluate how large an integration area is necessary for converging the brightness, although their work was not aimed at the calculation of the scattered field pattern. Fresnel zone number was again introduced in the discussion of the large-size local-domain basis function for the method of moments [2.9]. Although the paper focused on scattering analyses, Fresnel zone number was not directly used for analyses; the relationship between Fresnel zone number and the degree of sparsity of impedance matrices was investigated in the paper. The first paper is [2.10] where Fresnel zone number was directly used for analyses. In a series of these researches, the insight into Fresnel zone number as well as discussion on how to apply it had been deepened.

In this chapter, some explanations about the SPM are at first given. Next, the relationship between the SPM and the localization based on Fresnel zone number will be explained. After that the detail of the localization and windowing function will be introduced. The validation of the Fresnel zone localization will be investigated through numerical and analytical approaches in the following subsection.

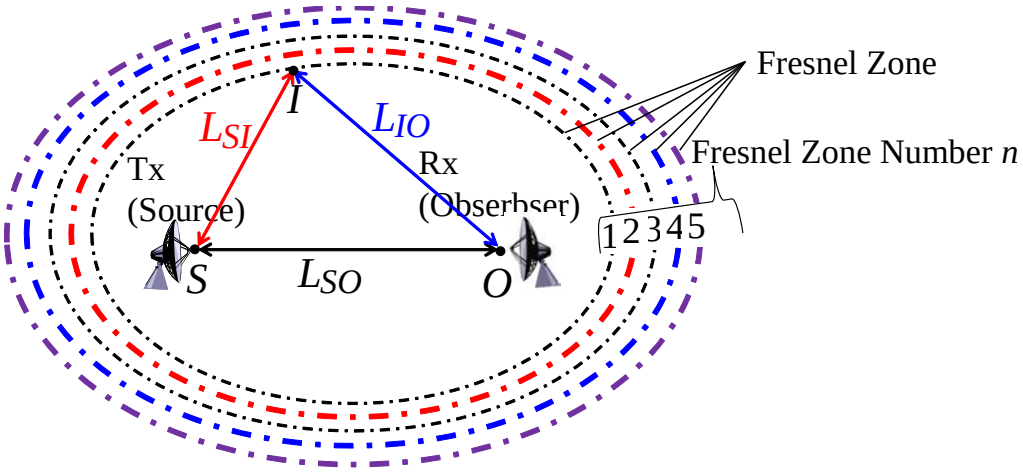

$$n = \frac{L_{SI} + L_{IO} - L_{SO}}{\lambda / 2}$$

Figure 2.1: Definition of Fresnel zone numbers

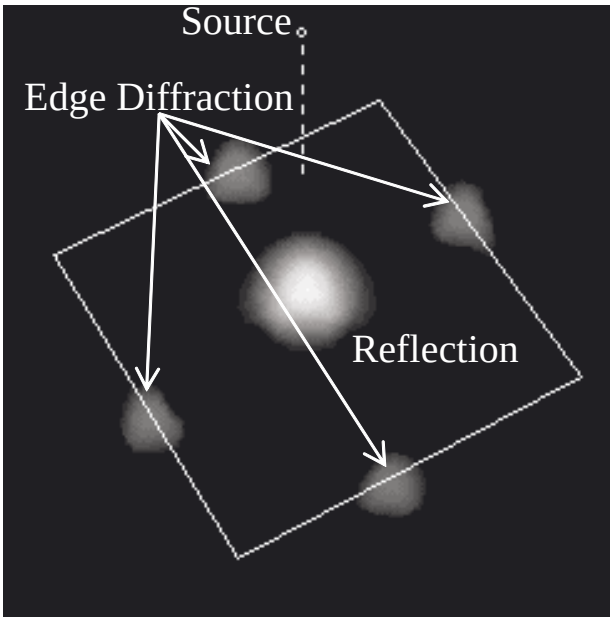

Figure 2.2: Visualization of locality in scattering from plate illuminated by a dipole (cited from [2.8])

2.2 Stationary Phase Method

The stationary phase method [2.4, 11] is one of the mathematical asymptotic techniques to evaluate integrals of highly-oscillating functions as

$$I = \int_{x_1}^{x_2} f(x) e^{-jkg(x)} dx, \tag{2.2}$$

where k is a real and a large positive parameter. This type of integrals often appear in radiation integrals for induced currents on a surface of a scatterer (e.g. electromagnetic scattering analysis by PO or MoM). In many cases of calculation in scattering analysis, k and $g(x)$ usually correspond to the wave number ($= 2\pi/\lambda$, where λ is the wavelength) and the path length from the source to the observer via the integration point, respectively. Based on the SPM, the integration of (2.2) can be approximated as

$$I \sim \begin{cases} \dfrac{f(x_2)}{jkg'(x_2)} e^{-jkg(x_2)} - \dfrac{f(x_1)}{jkg'(x_1)} e^{-jkg(x_1)} + O\left(k^{-2}\right) & g'(x) \neq 0 \ (x_1 \leq x \leq x_2) \\ \sqrt{\dfrac{-\pi}{2kg''(x_s)}} f(x_s) e^{-jkg(x_s)+\frac{\pi}{4}j} + O\left(k^{-1}\right) & g'(x_s) = 0, g''(x_s) \neq 0 \text{ and } x_s = x_1. \end{cases} \tag{2.3}$$

The physical meaning of (2.3) in radiation integrals is visualized in Fig. 2.3. In wave optics, an integrand in radiation integrals may often be a highly-oscillating function whose $g(x)$ can be approximated as $g(x) = L_{SI} + L_{IO}$. The middle of Fig. 2.3 depicts the behavior of the real (or imaginary) part of the integrand. This phase change becomes more rapid at higher frequencies. The contribution from the area with rapid phase changes is almost zero due to the cancellation effect. Therefore, the radiation integral over the entire area is well approximated by contribution from the inner stationary phase point (SPP) with the slowest phase change ($g(x) = 0$) and/or the edges of integration area. The former contribution corresponds to the first term of the second line of (2.3) (the $O\left(k^{-0.5}\right)$ term) and is often called "a relfected wave." The latter one corresponds to the first and second terms of the first line of it ($O\left(k^{-1}\right)$ terms) and is called "edge diffracted waves." These points are collectively called "scattering centers." When a frequency is high enough and k gets larger, the contribution from the inner SPP is the most dominant and the edge's ones are the second dominant. Note that the results by the SPM looks the contribution only from the scattering centers in analogy with ray optics, while components from the vicinities of the scattering centers are still considerable level in actual scattering phenomena as shown in Fig. 2.2.

Another key role of the SPM is to reduce a dimension of integrals. Although (2.2) is a form of one-dimensional integral, radiation integrals for practical scattering problems are usually a two-dimensional form. There are two ways to apply the SPM to surface

(2-D) integrals. First one is to approximate it by the sum of the contributions from a finite number of the points such as an inner SPP and edge diffraction points. This way is interpreted to apply the SPM to both of two axes which construct a coordinate system for a surface of scatterer at the same time (e.g. x- and y-axes of the Cartesian coordinate system and ρ- and ϕ- axes of the polar coordinates system for a planar surface). Another way is to convert the surface integral into the line integral along the periphery of scatterer. This is interpreted to apply it to either of the two axes and is often called "a line integral form." Note that if the SPM is applied to the latter one's result once again, the final results may be identical to that of former one. Both of the ways have been widely used to asymptotically (in some cases rigorously) evaluate the radiation integrals. The application examples of the former one are seen in [2.7, 12–15] and those of the latter one are also seen in [2.16–21].

Although the SPM has been a useful technique for scattering analyses, there are some problems. One of the representative problems is divergences of the results in some specific cases [2.22]. For instance, such singularities appear in the field at geometrical-optics incident and reflection shadow boundaries (ISB/RSB) and caustics. There are several techniques to avoid some of these singularities [2.7, 23, 24]. The similar singularities also appear in the diffracted field by the GTD although uniform versions of GTD have been proposed [2.3, 25, 26]. Note that the localization technique does not reduce the dimension of integral therefore such singularities never appear.

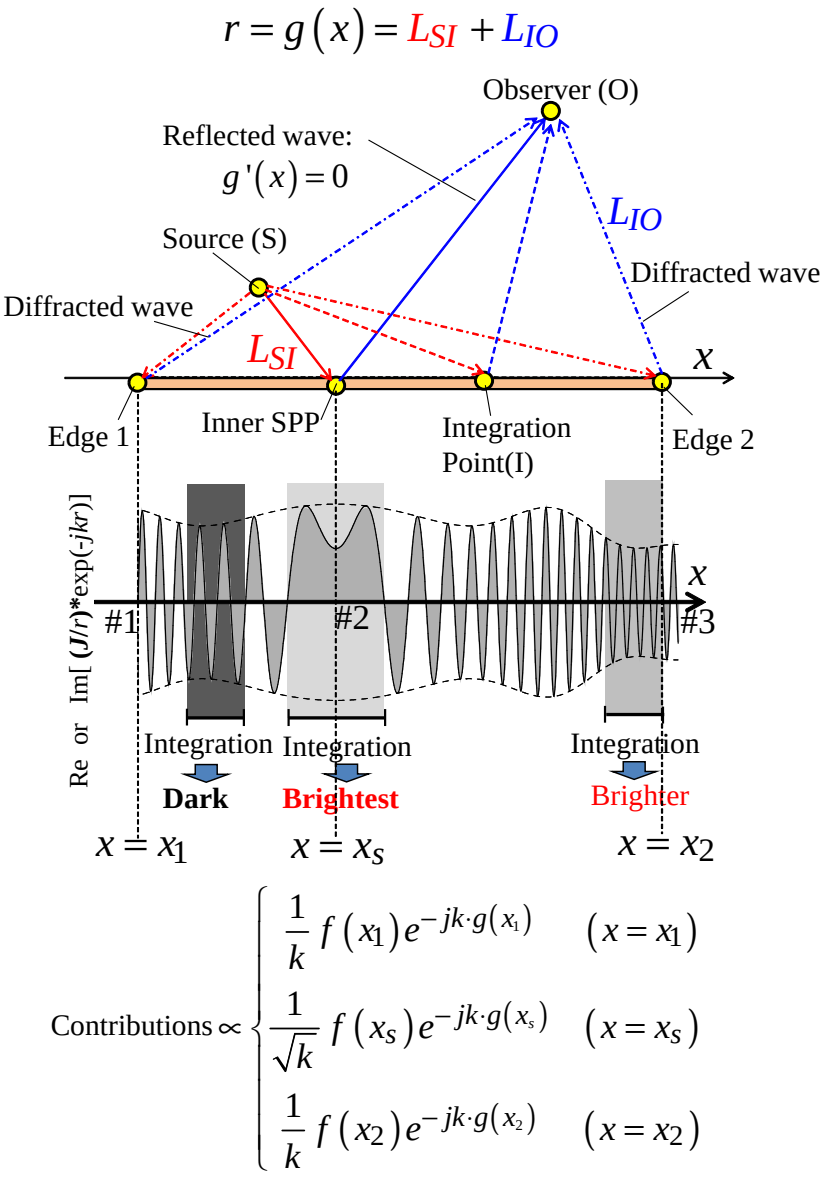

Figure 2.3: Physical meaning of the stationary phase method

2.3 Localization and Windowing Function based on Fresnel Zone Numbers

2.3.1 Physical interpretation of Fresnel zone number localization

Fig. 2.4 shows the concept of localization method. In the localization method, it is interpreted that dominant components of scattered fields come from not only the scattering

centers but also the neighboring areas. The importance monotonically decreases with distance from these centers. This property is well matched with the actual scattering phenomena of Fig. 2.2. Through the works of [2.8, 10], it was found that the areas where the considerable components exist should be specified by the difference of Fresnel zone numbers, in other words, the difference of optical path lengths. From the point of view of the SPM, the only points where the optical path length takes the extreme value are important. On the other hand, the localization method put importance on the area where the optical path length difference from the extreme value is less than a certain value (e.g. 1.5 λ in Fig. 2.4). The method to specify a local area for the inner SPP (reflection point) in terms of Fresnel zone number is depicted in Fig. 2.5. The area where the following conditions hold will be recognized as the areas with large contributions (here we name the area(s) as "local area(s)").

$$n_R = \frac{L_{SR} + L_{RO} - L_{SO}}{\lambda/2} \tag{2.4}$$

$$|n - n_R| = \Delta n \leq \Delta n_B \tag{2.5}$$

n_R is the Fresnel zone number at the reflection point. The parameter Δn_B is the number to determine the size of the local area. The larger Δn_B creates the larger local area. The shape of local area is elliptical. Note that the center or focus points of this ellipse does not coincide with the inner SPP (See Appendix A). This criterion means that the area where the optical path length difference is smaller than $\Delta n_B(\lambda/2)$ is defined as the local area. In addition to that, the difference of Fresnel zone numbers corresponds to the number of half oscillation or the phase change normalized by π in the integrand (See Fig. 2.4).

This criterion is able to determine the appropriate size, position and shape of local areas depending on the source position, observer position and frequency because Fresnel zone number is the function of these variables. For instance, if the frequency becomes higher, the oscillation of integrand gets more rapid and the size of local area specified by Δn_B becomes smaller as Fig. 2.4 (b). Furthermore, if the frequency is infinitely higher, the local area converges to the point as ray optics or a point contribution approximation by the SPM. In that sense, the localization based on Fresnel zone number is the method to connect the concept of wave optics and that of ray optics smoothly. This is a new insight into the interpretation of scattering phenomena, which never appears in the discussion on wave optics nor ray optics.

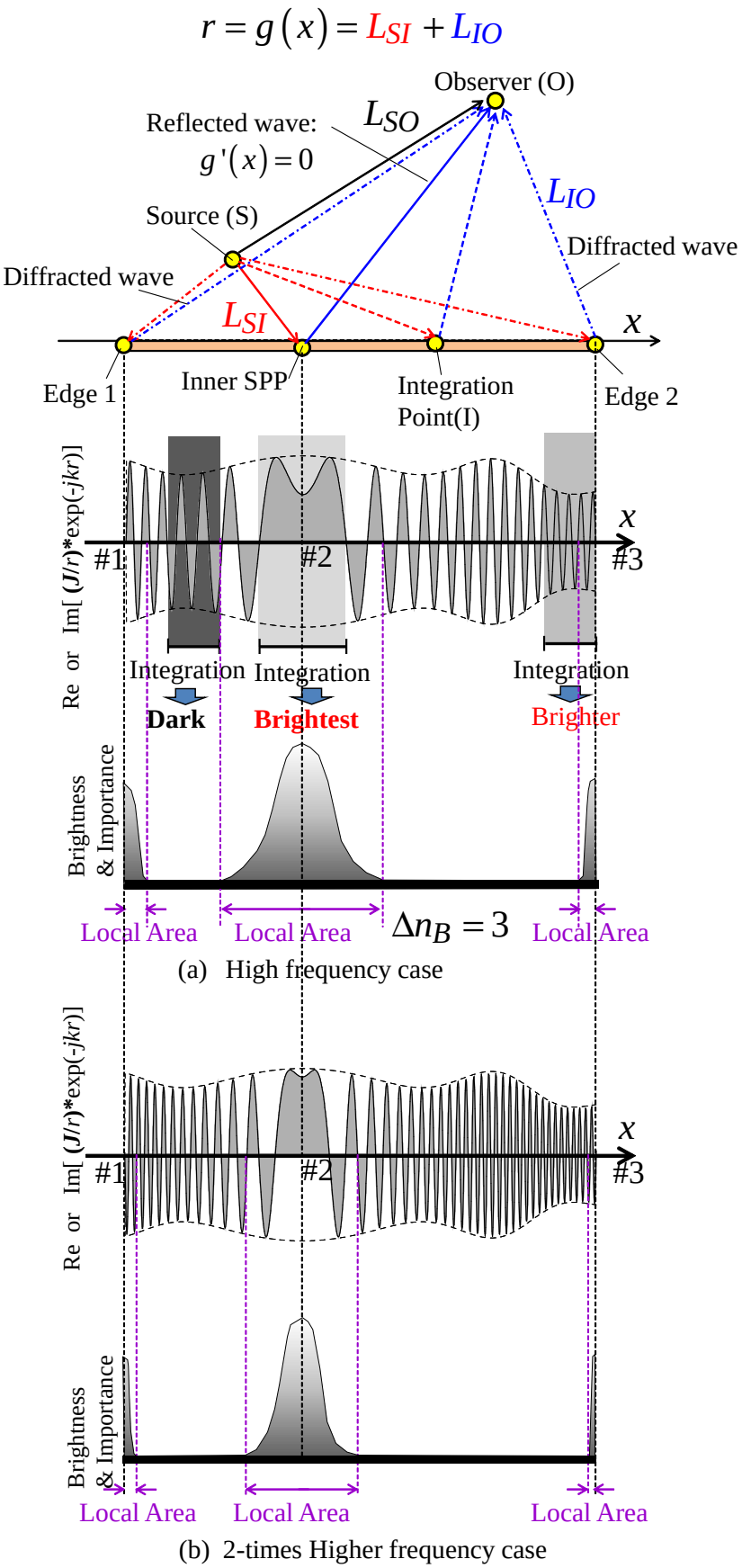

Figure 2.4: Physical meaning of the localization

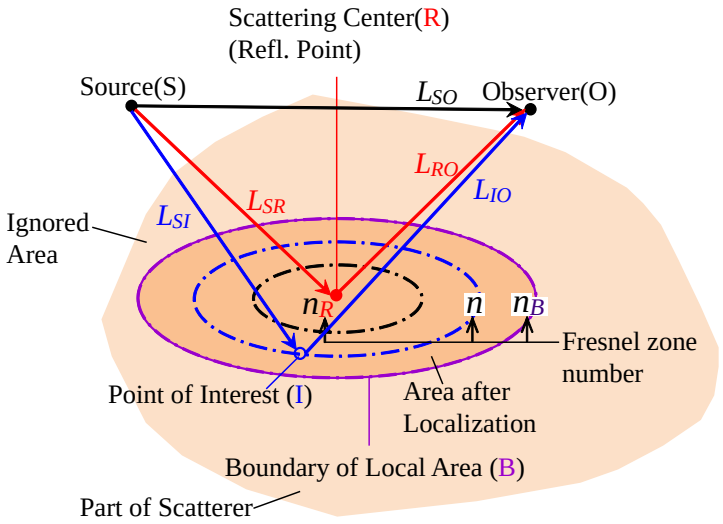

Figure 2.5: Localization for the inner SPP (reflection point)

2.3.2 Implementation of Fresnel zone localization and discussion on windowing function

The "implementation of locality (or localization technique) into scattering analysis" means that an analysis surface area is restricted to the local areas and the other areas are ignored. Let us consider that the localization is applied to the radiation integral for perfect electric conductor (PEC) infinite plate illuminated by the dipole source as shown in Fig. 2.6 as an example of localization. The dipole is located at $(x, y, z) = (0, 0, d)$ and the observer is at the angle θ and infinite distance from plate. Note that in this case the induced currents $\boldsymbol{J}$ is rigorously identical to PO's currents as $\boldsymbol{J}_{PO} = 2\hat{n} \times \boldsymbol{H}_i$ where $\hat{n}$ is the unit normal vector on the plate and $\boldsymbol{H}_i$ is an incident field from a dipole source. The imaginary part of integrand is shown in Fig. 2.7. After the localization (truncation), the discontinuities of the envelope of the integrand appear at the boundaries of local area (See Fig. 2.7 (b)). So these boundaries look fictitious edges which do not exist in the original problem and would produce undesired diffracted fields.

In order to suppress these, a windowing function is introduced. This function should take the values 1 at the scattering center so that the result of radiation integral remains unchanged due to localization, smoothly decreases towards the boundary of the local area and takes the value 0 at the boundary (See Fig. 2.7 (c)).

A raised cosine function is one of the candidates which satisfy these conditions. In [2.8, 10], the function in (2.6), named "EYE function," was adopted. r and r_B are the actual distance from the scattering center to the integration point and to the boundary of

the local area, respectively (See Fig. 2.6).

$$EYE\left(\frac{r}{r_B}\right) = \begin{cases} \cos^2\left(\frac{r}{r_B}\cdot\frac{\pi}{2}\right) & r \le r_B \\ 0 & r > r_B \end{cases} \tag{2.6}$$

After multiplying the EYE function with the truncated integrand, the fictitious edges disappear and the envelope of the integrand in Fig. 2.7 (d) resembles the figures of "brightness & importance" in Fig. 2.4. As mentioned later, the EYE function of (2.6) has the disadvantage of the trade-off relationship between the computation accuracy and the smallness of Δn_B. This is because (2.6) was originally designed for the visualization [2.8] and was not optimized for the localization using the general concept of the Fresnel zone number. Reflecting the knowledge of the localization using the Fresnel zone numbers, we here newly propose to adopt the Fresnel zone number instead of the actual distance as the argument in the EYE function as follows;

$$EYE\left(\frac{\Delta n}{\Delta n_B}\right) = \begin{cases} \cos^2\left(\frac{\Delta n}{\Delta n_B}\cdot\frac{\pi}{2}\right) & \Delta n \le \Delta n_B \\ 0 & \Delta n > \Delta n_B. \end{cases} \tag{2.7}$$

Here, we examine the superiority of the new EYE function (2.7) to the old one (2.6). The reflected far field from the infinite PEC plate as shown in Fig. 2.6 was calculated by the proposed localization technique and compared with that by the image theory. The minimum value of Δn_B which reproduces the original field is searched.

Fig. 2.8 presents the comparison for various values of Δn_B for various conditions of d and θ. The left vertical axis indicates relative amplitudes of field after localization normalized by that of image field. The right vertical axis indicates phase differences. For both of the windowing functions, (2.7) and (2.6), the amplitude and the phase converge to the exact ones when Δn_B becomes large enough. The phase difference by the old one ($EYE(r/r_B)$) however does not reach zero even in $\Delta n_B = 8$. That is, in the old one, there is the trade-off relationship between the computation accuracy and the smallness of Δn_B. On the other hand, the new one ($EYE(\Delta n/\Delta n_B)$ in Fig. 2.8) brings about much faster phase convergence than the old one. Furthermore, in the new one, both of the amplitude and phase are identical to the exact one when Δn_B is odd number and not smaller than 3; $\Delta n_B = 3$ seems the optimum number for the localization. The Fresnel zone number realizes the uniform criteria valid for all the combinations of parameters θ and d as shown in Fig. 2.8.

The resultant total fields in the same model are shown in Fig. 2.9. The distance d is fixed at 10λ and θ varies from 0° to 30°. In $EYE(r/r_B)$ case, the interference between the

scattered and incident field cannot be reproduced accurately. $EYE(r/r_B)$ for Δn_B adopted in [2.10] is also presented for comparison and the superiority of the new one is obvious in terms of both the accuracy and the smallness of the integration area. These results clarify the superior of the new EYE function and the fact that the area where $\Delta n_B = 3$ or the path difference is smaller than $(3/2)\lambda$ is enough to calculate the fields. Hereafter, we adopt $\Delta n_B = 3$ together with the new EYE function of (2.7).

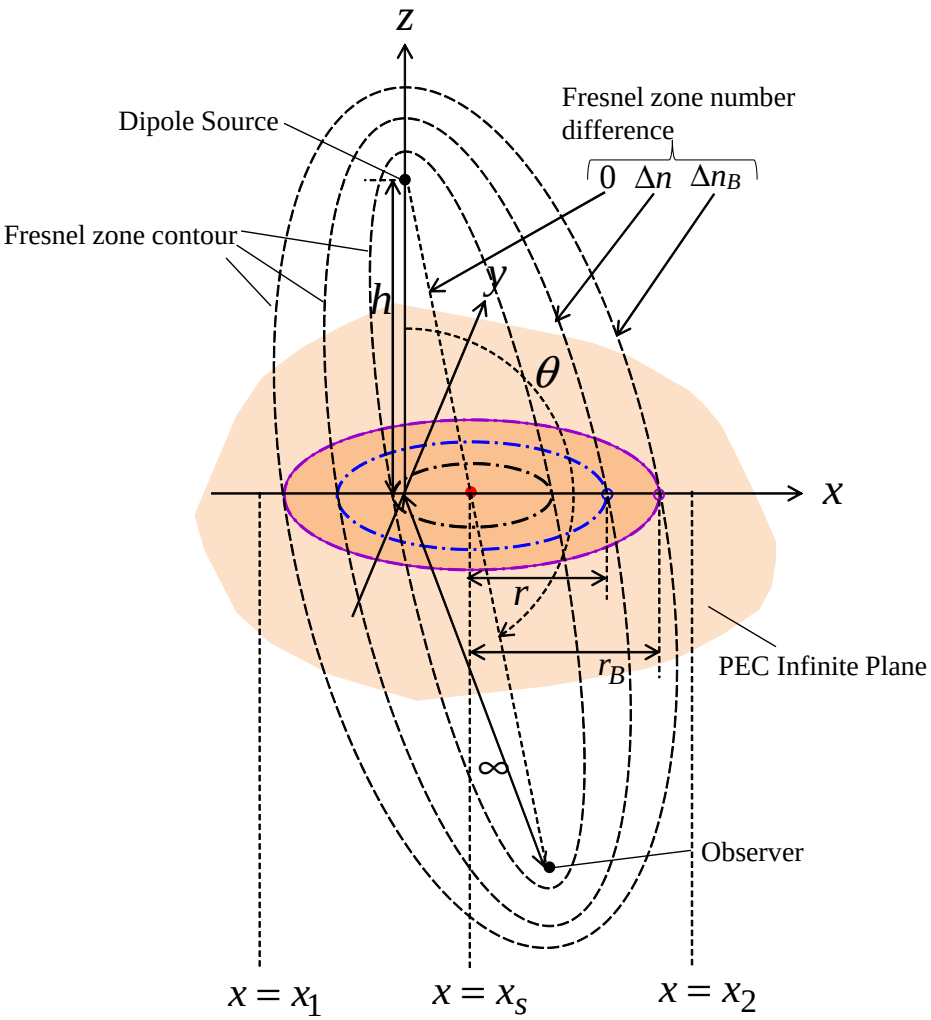

Figure 2.6: Localization of scattering phenomena from an infinite PEC plate with a dipole source

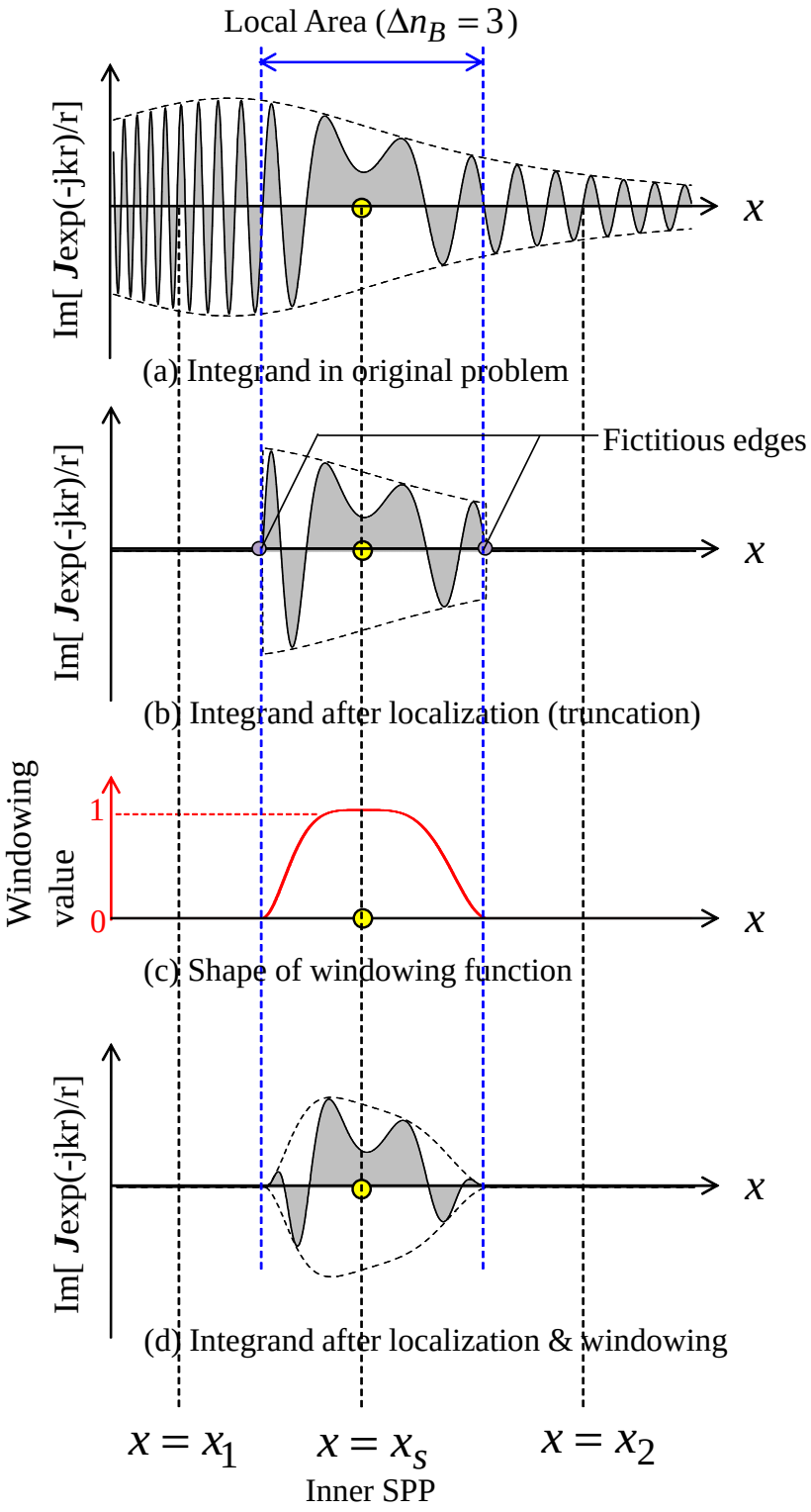

Figure 2.7: Integrand before/after the localization/windowing

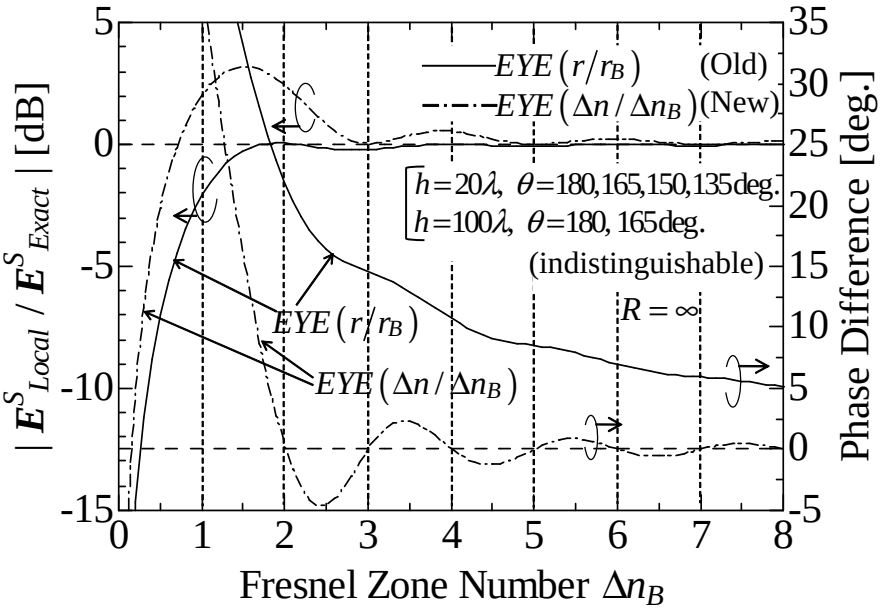

Figure 2.8: Convergence of the radiation integration result against Δn_B which is the parapeter to determine the size of local area

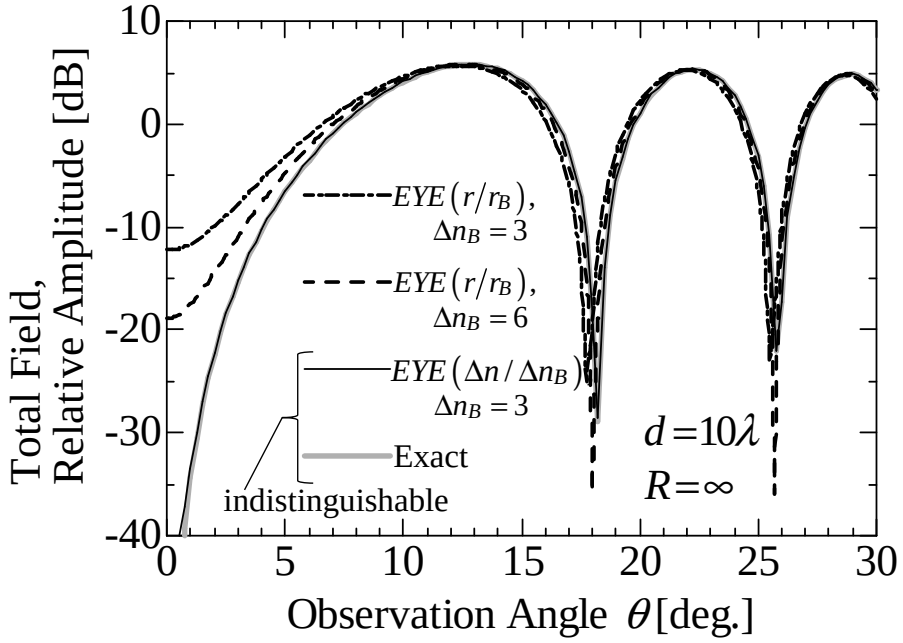

Figure 2.9: Comparison of total field patterns of the infinite plates and a dipole

2.4 Analytical Expression of Fresnel Zone Localization

2.4.1 Size of Local Areas in Terms of Wavelength

Here let us consider the frequency dependence of size of local area for the case of Fig. 2.6. The local area is basically an ellipse for any θ. The lengths of semi-major axis and semi-minor axis, a and b respectively, are expressed as

$$\frac{a}{\lambda} = \frac{\sqrt{\left(\frac{\lambda}{2}\Delta n_B\right)^2 + 2h\left(\frac{\lambda}{2}\Delta n_B\right)|\cos\theta|}}{\lambda\cos^2\theta} = \frac{\sqrt{\left(\frac{\Delta n_B}{2}\right)^2 + h\left(\frac{\Delta n_B}{\lambda}\right)|\cos\theta|}}{\cos^2\theta} \tag{2.8}$$

$$\frac{b}{\lambda} = \frac{\sqrt{\left(\frac{\lambda}{2}\Delta n_B\right)^2 + 2h\left(\frac{\lambda}{2}\Delta n_B\right)|\cos\theta|}}{\lambda\cos^4\theta} = \frac{\sqrt{\left(\frac{\Delta n_B}{2}\right)^2 + h\left(\frac{\Delta n_B}{\lambda}\right)|\cos\theta|}}{|\cos\theta|}. \tag{2.9}$$

When θ is 0° or 180°, the local area becomes a true circle. The radius R ($= a = b$) is expressed as

$$\frac{R}{\lambda} = \sqrt{\left(\frac{\Delta n_B}{2}\right)^2 + \frac{h\Delta n_B}{\lambda}}. \tag{2.10}$$

Derivation of these formula is summarized in Appendix A. Obviously, the normalized values of a and b (including R) by the wavelength have the frequency dependence as $O(\lambda^{-\frac{1}{2}}) = O(f^{\frac{1}{2}})$. In conclusion, the electrical area size (unit: λ^2) of surface area of ellipse increase in almost proportional to f. This characteristic is very important to consider the frequency dependence of computational costs when the localization method is applied.

Let us consider the size of local area ($\Delta n_B = 3$ and $\theta = 0^\circ$) defined on the planar plate with the finite physical length of 5 meters. As shown in Fig. 2.10, the physical size of local area, which produces strong contributions to the observer, becomes smaller in higher frequency as Fig. 2.4(b). The electrical area size of it however becomes larger as frequency gets higher. This discrepancy can be explained as follows; if the physical size of whole area (plate) remains unchanged, the electrical area size of whole area increases in proportional to f^2 while that of local area also increase as $O(f)$ tendency. This difference of frequency dependencies makes an impression that the local area shrinks for higher frequencies *in a visual sense*, although it enlarges in terms of the wavelengths.

This difference is the big advantage of localization method. In PO or MoM, the computational costs increase depending on $L = kR_s$ where R_s is the radius of the smallest sphere circumscribing the scatterer. If the whole area is regarded as analysis area, L has the $O(f)$ tendency. On the other hand, in the scattering analysis of local area, it has $O(f^{\frac{1}{2}})$ tendency. So we can suppress the computational costs by using the localization method while the costs of localization method themselves increase with higher frequency.

In order to realize the frequency-independent computational cost, we need to combine the localization method with another technique as discussed in Chapter 4.

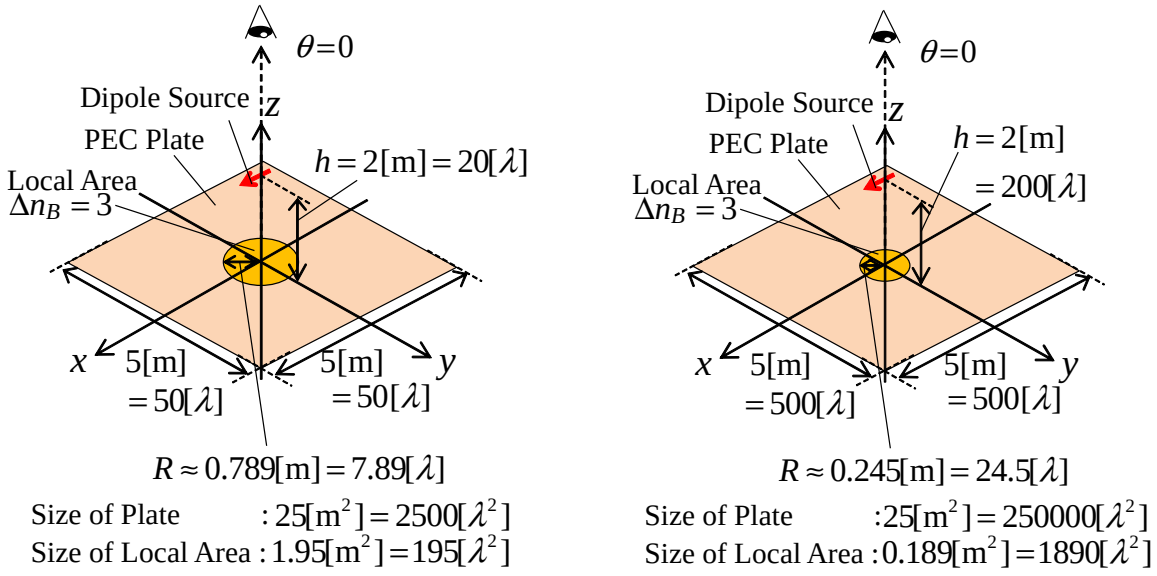

(a) $f = f_0 = 2.9979$GHz (b) $f = 10f_0$

Figure 2.10: Size of plate with finite physical length and local area

2.4.2 Error in Localization

In 2.3.2, we concluded that $\Delta n_B = 3$ is the optimum number for localization because the error of amplitude and phase of scattered field looks zero for any value of h and θ in Fig. 2.8. However, strictly speaking, these errors are not zero and they depend on h and θ. Fig. 2.11 shows the relative error of the results by the localization method with the $\Delta n_B = 3$ criterion. Here the relative error ε is defined as

$$\varepsilon = \frac{\left|\boldsymbol{E}^S_{Local} - \boldsymbol{E}^S_{Exact}\right|}{\left|\boldsymbol{E}^S_{Exact}\right|} \tag{2.11}$$

where $\boldsymbol{E}^S_{Local}$ is the calculated scattered field based on the localization method with $\Delta n_B = 3$ and $\boldsymbol{E}^S_{Exact}$ is the exact solution calculated by image theory. This graph shows the relative error ε is susceptible not to θ value but to h. The $\boldsymbol{E}^S_{Local}$ in Fig. 2.11 was calculated by numerical integration based on the rectangle method with the double precision and the segment size of 0.01λ. It is difficult to derive the analytical representation of this error for arbitrary cases. Here we show it for $\theta = 0°$ case. $\boldsymbol{p}$ is a dipole moment and $\hat{r}_o$ is a

unit vector from the origin to the observer at $\theta = 0°$, that is, $\hat{r}_o = \hat{z}$. ω and μ denote the angular frequency and the permeability, respectively. Derivation of these is summarized in Appendix B.

$$\boldsymbol{E}^S_{Exact} = \boldsymbol{E}_0 I_\infty \tag{2.12}$$

$$\boldsymbol{E}^S_{Local} = \boldsymbol{E}_0 I_L \tag{2.13}$$

$$\boldsymbol{E}_0 = \frac{\omega\mu kh}{4\pi} e^{-jkh} \left\{ \hat{r}_o \times (\hat{r}_o \times \boldsymbol{p}) \right\} \tag{2.14}$$

$$I_\infty = \frac{1}{jkh} \tag{2.15}$$

$$I_L = \frac{1}{2} I_0 + \frac{1}{4} I_+ + \frac{1}{4} I_- \tag{2.16}$$

$$I_0 = j \left\{ \frac{e^{-j\pi\Delta n_B}}{k\left(h + \frac{\lambda}{2}\Delta n_B\right)} - \frac{1}{kh} \right\} \tag{2.17}$$

$$\begin{aligned} I_\pm = & j \left(1 \pm \frac{1}{\Delta n_B} \right) e^{+jkh\left(1 \pm \frac{1}{\Delta n_B}\right)} \left[\frac{e^{-ju}}{u} \right]^{k\left(h + \frac{\lambda}{2}\Delta n_B\right)\left(1 \pm \frac{1}{\Delta n_B}\right)}_{u = kh\left(1 \pm \frac{1}{\Delta n_B}\right)} \\ & + \frac{1}{\Delta n_B} e^{+jkh\left(1 \pm \frac{1}{\Delta n_B}\right)} \left[\mathrm{E}\left(u\right) \right]^{k\left(h + \frac{\lambda}{2}\Delta n_B\right)\left(1 \pm \frac{1}{\Delta n_B}\right)}_{u = kh\left(1 \pm \frac{1}{\Delta n_B}\right)} \end{aligned} \tag{2.18}$$

$$I_- = \left[\ln u - \frac{u}{j\pi} \right]^{1 + \frac{2h}{\lambda}}_{u = \frac{2h}{\lambda}} \quad (\Delta n_B = 1) \tag{2.19}$$

$\mathrm{E}(x)$ is the function related with the sine integral $\mathrm{si}(x)$ and the cosine integral $\mathrm{ci}(x)$ as

$$\mathrm{E}(x) = -\int_x^\infty \frac{e^{-jt}}{t} dt = \mathrm{ci}\left(x\right) - j\,\mathrm{si}\left(x\right) \tag{2.20}$$

$$\mathrm{si}\left(x\right) = -\int_x^\infty \frac{\sin t}{t} dt \tag{2.21}$$

$$\mathrm{ci}\left(x\right) = -\int_x^\infty \frac{\cos t}{t} dt \tag{2.22}$$

$$\mathrm{E}(x) \sim \frac{je^{-jx}}{x} \quad (x \gg 1). \tag{2.23}$$

We also define $\kappa = I_L / I_\infty$ as the ratio of the localization's result to the exact solution. Note that the amplitude and phase of κ correspond to the left and right vertical axes of Fig. 2.8, respectively.

In addition to the rigorous formula of (2.16) to (2.19), we derive the asymptotic formula of (2.16). When $kh \gg 1$ and $\Delta n_B \geq 2$, $x \gg 1$ holds. By applying the approximation of

(2.23), I_L and κ are approximated as

$$I_L \sim \frac{1}{4jkh}\left\{2+\frac{2}{1-\left(\frac{1}{\Delta n_B}\right)^2}\right\} - \frac{e^{-j\pi\Delta n_B}}{4jkh\left(1+\frac{\pi\Delta n_B}{kh}\right)}\left\{2-\frac{2}{1-\left(\frac{1}{\Delta n_B}\right)^2}\right\} \tag{2.24}$$

$$\kappa \sim \frac{1}{4}\left\{2+\frac{2}{1-\left(\frac{1}{\Delta n_B}\right)^2}\right\} - \frac{e^{-j\pi\Delta n_B}}{4\left(1+\frac{\pi\Delta n_B}{kh}\right)}\left\{2-\frac{2}{1-\left(\frac{1}{\Delta n_B}\right)^2}\right\}. \tag{2.25}$$

Table 1 shows the comparison of relative errors ε calculated by three methods; the analytical and rigorous value (based on (2.16) to (2.19)), the numerical integration result (Fig. 2.11) and the approximated value (using (2.24) instead of (2.16)) for $\Delta n_B = 3$. The numerical integration results, which may include the numerical errors due to the rounding or rectangular integration method, are in very good agreement with the analytical ones. The approximated values also succeeded in predicting the errors well.

The value of κ is the intrinsic and inevitable error of localization method. Let us consider the characteristic of κ by using the asymptotic formula of (2.25). When Δn_B is integer, κ in (2.25) is a real number, that is, the phase of κ is zero. The amplitude (absolute value) of κ is always more than 1 and takes the local minimum value when Δn_B is an odd integer number. Note that (2.25) holds for $\Delta n_B \geq 2$. These are the same conclusion as that in 2.3.2.

If the errors due to the localization with the windowing must be avoided (e.g. required computational accuracy is very severe), we may add a correction term predicted by (2.16) or (2.24) to (2.7). At that moment, we should neglect the observation-angle dependence of errors and should use the correction value for $\theta = 0^\circ$ because its dependence is insignificant. Furthermore, the correction term itself is not necessary for most of the practical cases because the relative error becomes -29 dB at largest (See Fig. 2.12) and -29-dB relative error is acceptable in most of the scattering analyses. So we do not use the correction term throughout this dissertation.

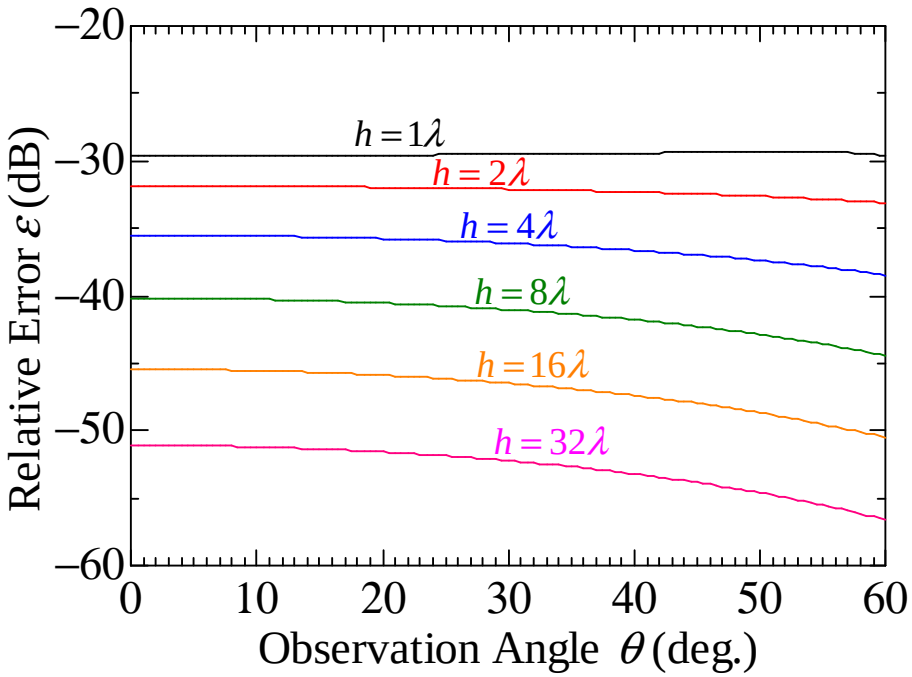

Figure 2.11: Relative error of localization with $\Delta n_B = 3$ in the model of Fig. 2.6. These errors correspond to the value at $\Delta n_B = 3$ of Fig. 2.8

Table 1: Relative Errors ε for $\theta = 0°$ and $\Delta n_B = 0$ in the case of Fig. 2.6.

h (λ)	Analytical value (dB) (based on (2.16) to (2.19))	Numerical integration (dB) (refer to Fig. 2.11)	Approximated value (dB) (based on (2.24))
1	-29.6156	-29.6156	-28.5194
2	-31.8537	-31.8537	-31.4419
4	-35.5015	-35.5015	-35.3678
8	-40.1540	-40.1540	-40.1150
16	-45.4319	-45.4319	-45.4213
32	-51.0642	-51.0642	-51.0615

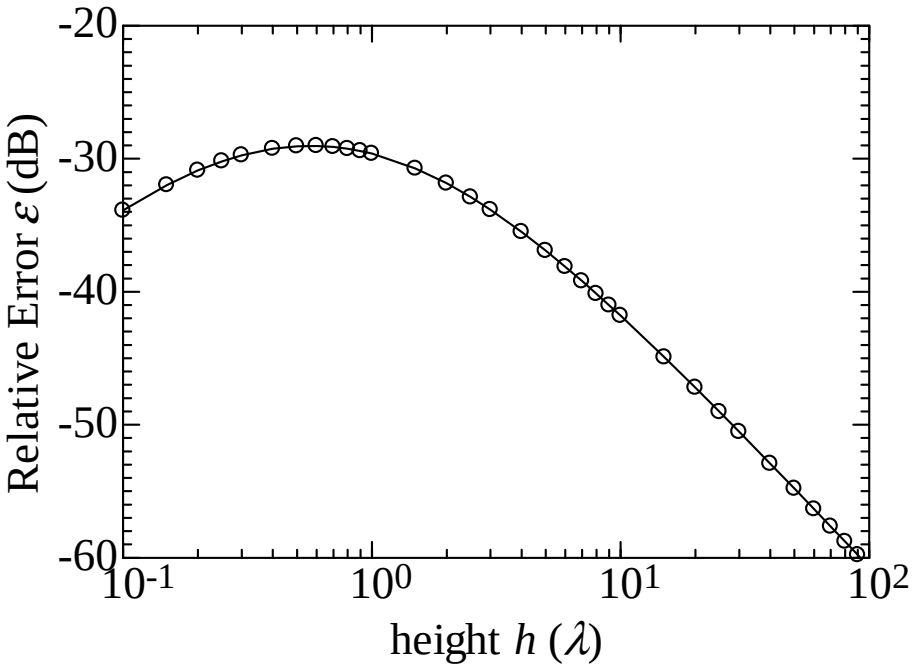

Figure 2.12: Analytical value of the relative errors against h, calculated by (2.16)

2.5 Concluding Remarks

In this chapter, the fundamental knowledge and interpretation of Fresnel zone number localization were provided. We compared the SPM and the localization method based on Fresnel zone number. The localization with Fresnel zone number enables the physical interpretation of scattered fields unlike the PO or MoM, and the results by localization never include the singularities unlike that of the SPM. In that sense, the localization method is situated between the wave optics (e.g. PO) and ray optics (e.g. GTD or UTD). Necessity of windowing function was explained and the EYE function was introduced as one of the candidates of windowing function. We proposed the new EYE function Fig. 2.7 whose argument is also the Fresnel zone number. The superiority of the new one to the old one was shown with the numerical data.

We analytically showed the fact that the electrical area size of local area has the frequency dependence as $O(f)$ while that of the whole surface with constant physical length has $O(f^2)$. This difference on frequency dependencies indicates the advantage of localization method in terms of computational cost reduction for higher frequencies. Finally, we showed the analytical and asymptotic formula of the error due to the localization method with EYE function. Since the maximum of the relative error is up to -29 dB, the correction term is not necessary for most of the practical scattering analyses. If the higher accuracy

is required, we may add the correction term.

Other functions are possible to be used as windowing function as long as they satisfy the condition mentioned in 2.3.2, that is, they take 1 at scattering centers and smoothly decrease toward the boundary of local area and take 0 at the boundary. We however use the EYE function of (2.7) as windowing throughout this dissertation since its characteristic has already been investigated very well.

References

[2.1] T. S. Rappaport, *Wireless Communication: Principal and Practice,* 1st Ed., Prentice Hall PTR, pp.89-99, 1996.

[2.2] J. B. Keller, "Geometrical theory of diffraction," *Journal of the Optical Society of America*, vol.52, pp116-130, 1962.

[2.3] R. G. Kouyoumjian and R. H. Pathak, "A uniform geometrical theory of diffraction for an edge in a perfectly conducting surface," *Proceedings of the IEEE*, vol.62, no.11, pp.1448-1461, Nov. 1974.

[2.4] V. A. Borovikov, *Uniform Stationary Phase Method*, IEE Electromagnetic waves series 40, 1994.

[2.5] R. F. Harrington, *Time-Harmonic Electromagnetic Fields*, pp.127-130, McGraw-Hill, New York. 1961.

[2.6] C. A. Balanis, *Advanced Engineering Electromagnetics*, pp.694-696, New York. Wiley, 1989.

[2.7] O. M. Conde, J. Perez, M. P. Catedra, "Stationary phase method application for the analysis of radiation of complex 3-D conducting structures," *IEEE Transaction of Antennas and Propagatation*, vol.49, no.5, pp.724-731, May 2001.

[2.8] T. Shijo, T. Itoh, M. Ando, "Visualization of high frequency diffraction based on physical optics," *IEICE Transaction on Electronics* vol.E87-C, no.9, pp.1607-1614, Sep. 2004.

[2.9] T. Shijo, T. Hirano, and M. Ando, "Large-Size Local- Domain Basis Functions with Phase Detour and Fresnel Zone Threshold for Sparse Reaction Matrix in the Method of Moments," *IEICE Transaction on Electronics.*, Vol.E88-C, No.12, pp.2208-2215, Dec. 2005.

[2.10] K. Ito, T. Shijo, M. Ando, "Fresnel zone criterion to implement locality in the method of moments and PO-MoM hybrid method for the reduction of unknowns," *IEICE Transaction on Electronics*, vol.E94-C, no.1, pp72-79, Jan. 2011.

[2.11] G. L. James, *Geometrical Theory of Diffraction for Electromagnetic Waves*, Stevenage, U. K.: Peregrinus, 1980.

[2.12] W. H. Ierley and H. Zucker, "A stationary phase method for the computation of the far field of open cassegrain antennas," *Bell System Technical Journal*, vol.49, no.3, pp.431-454, Mar. 1970.

[2.13] C. A. Siller, Jr., "Evaluation of the radiation integral in terms of end-point contributions," *IEEE Transaction on Antennas and Propagation*, vol.23, no.5, pp.743-745, Sep. 1975.

[2.14] H. Ikuno, "Calculation of far-scattered fields by the method of stationary phase," *IEEE Transaction on Antennas and Propagation*, vol.27, no.2, pp.199-202, Mar. 1979.

[2.15] H. Ikuno, M. Nishimoto, "Calculation of transfer functions of three-dimensional indented objects by the physical optics approximation combined with the method of stationary space," *IEEE Transaction on Antennas and Propagation*, vol.39, no.5, pp.585-590, May 1991.

[2.16] A. Michael, "Equivalent edge currents for arbitrary aspects," *IEEE Transaction on Antennas and Propagation*, Vol.AP-32, No.3, Mar. 1984.

[2.17] P. Y. Ufimtsev, "Elementary edge waves and the physical theory of diffraction," *Electromagnetics*, vol.11, iss.2, pp.125160, 1991.

[2.18] P. M. Johansen and O. Breinbjerg, "An exact line integral representation of the physical optics scattered field: The case of a perfectly conducting polyhedral structure illuminated by electric Herzian dipoles," *IEEE Transaction on Antennas and Propagation*, vol.AP-43, no.7, pp.689-696, Jul. 1995.

[2.19] K. Sakina and M. Ando, "Mathematical derivation of modified edge representation for reduction of surface radiation integral," *IEICE Transaction on Electronics*, vol.E-84-C,no.1,p.74-83, Jan. 2001.

[2.20] M. Albani and S. Maci "An Exact Line Integral Representation of the PO Radiation from a Flat Perfectly Conducting Surfaces Illuminated by Elementary Electric or Magnetic Dipoles," *Turk. J. Electr. Eng.*, vol.10, no.2, pp.291-305, 2002.

[2.21] M. Albani, "Boundary Diffracted Wave and Incremental Geometrical Optics: A Numerically Efficient and Physically Appealing Line-Integral Representation of Radiation Integrals. Aperture Scalar Case," *IEEE Transaction on Antennas and Propagation*, vol.59, no.2, pp.586-594, Feb. 2011.

[2.22] M. Ando, P. Lu and T. Kohama, "Discussion of physical optics surface integration for deep interpretation of GTD," *Proceeding of IEEE-APS Topical Conference on Antennas and Propagation in Wireless Communications (APWC)*, pp.1141-1144, Sep. 2012.

[2.23] J. C. Cooke, "Stationary phase in two dimensions," *IMA Journal of Applied Mathematics*, vol. 29, pp. 2537, 1982.

[2.24] J. P. McClure and R.Wong, "Two-dimensional stationary phase approximation: Stationary point at a corner," *SIAM Journal on Mathematical Analysis*, vol. 22, pp. 500523, Mar. 1991.

[2.25] D. S. Ahluwalia, R. M. Lewis, and J. Boersma, "Uniform asymptotic theory of diffraction by a plane screen," *SIAM Journal on Applied Mathematics*, vol. 16, pp. 783807, 1968.

[2.26] S.W. Lee and G. A. Deschamps, "A uniform asymptotic theory of electromagnetic diffraction by a curved wedge," *IEEE Transaction on Antennas and Propagation*, vol. 24, no. 1, pp. 2534, Jan. 1976.

Chapter 3

Fresnel Zone Localization of Radiation Integrals

3.1 Introductory Remarks

Most of the numerical calculation methods for electromagnetic fields, such as the Method of Moments (MoM) [3.1], Finite Element Method (FEM) [3.2, 3] and Finite-Difference Time-Domain (FDTD) [3.4, 5], are suitable only for the low frequencies due to increasing computational loads in the high frequency. On the other hand, the high frequency diffraction techniques such as Geometrical Theory of Diffraction (GTD) [3.6], Uniform Geometrical Theory of Diffraction (UTD) [3.7] and Physical Theory of Diffraction (PTD) [3.8, 9], give the enhanced accuracy in higher frequency, by taking the advantage of so-called "the locality of scattering phenomena" without increasing the computational loads.

The concept of "locality" was embodied by the authors of [3.10] and was visualized as mentioned in the chapter 2. The points with a strong contribution appear near the scattering center, that is, the reflection points and the edge diffraction points. GTD and UTD focus upon only the local corrections at the diffraction points. Physical Optics (PO) [3.11] approximates the induced currents focusing upon the local direction of the surface at the point of locality. PTD provides the local correction for PO in terms of fringe wave (FW) and leads to alternative and compatible results with UTD.

Regardless of these, the locality had been conceptual and too ambiguous for us to implement into calculation algorithm. There had been few examples which quantifies and utilize the locality, except PO-MoM hybrid method which explicitly uses the locality of the fringe wave [3.12, 13]. A hybrid method which complementarily uses PO and MoM suggested the use of locality but no general criteria has been discussed even in the recent papers [3.14]. Authors have tried to visualize [3.10], evaluate and implement the concept of locality. In their work of [3.15], the large-size local domain basis functions which make the reaction matrix in the MoM sparse were introduced and the Fresnel zone numbers were used as the truncation criteria based upon locality for the first time; the sizes of the matrix were successfully reduced and the computational load increase of MoM was remedied. The author further applied the Fresnel zone number for the direct reduction of the scattering objects into its partial or skeleton scatterers. The reduced scatterers

are compactly analyzed by MoM and the smooth weighting functions for suppressing the unwanted contribution emanating from truncation edges assured the highly accurate results [3.16]. The Fresnel zone number, proposed to use as the criteria for localization in [3.16], is the function of the positions of the source, observer and the point of interest on the scatterer as explained in the chapter 2. [3.16] also showed that Fresnel zone number is also useful for defining the seamless transition points between PO and MoM in PO-MoM hybrid method. Unfortunately, in [3.16],the Fresnel zone numbers for localization (truncation) depended upon types of scattering centers; $\Delta n_B = 4$ for the reflection points while $\Delta n_B = 6$ for the edge diffraction points for example were adopted. Furthermore, the discussions in [3.15, 16] were conducted only for two-dimensional problems.

In this chapter, how to apply the localization method to diffraction points is reviewed. Fresnel zone number localization is applied not directly to the actual surface but to the virtual one associated with the modified surface-normal vector satisfying the reflection law in [3.17]. The two revisions, incorporating the modified surface-normal vectors and adopting the Fresnel zone number in the windowing function (refer to the chapter 2), bring about the following two advantages; the uniform treatment of various types scattering centers and the applicability to 3-dimensional problems. Although these revisions also seem effective for 2-dimensional cases, in this chapter, they are conducted only for 3-dimensional cases.

3.2 Localization for Practical Scattering Problems

3.2.1 Localization for Edge and/or Corner Diffraction Points

Here, we newly introduce the localization method for the general point including the edge diffraction point, incorporating the modified surface-normal vector to the localization method. Fig. 3.1 shows the method to determine the local areas for both of the reflection and diffraction points. As for the reflection point, as already mentioned in the chapter 2, the area which satisfies the following conditions will be recognized as the local area;

$$n_R = \frac{L_{SR} + L_{RO} - L_{SO}}{\lambda/2} \tag{3.1}$$

$$n = \frac{L_{SI} + L_{IO} - L_{SO}}{\lambda/2} \tag{3.2}$$

$$|n - n_R| = \Delta n \leq \Delta n_B \tag{3.3}$$

where n and n_R is the Fresnel zone number at a point of interest and at the reflection point, respectively.

On the other hand, these conditions of (3.1) to (3.3) cannot be directly applied to edge or corner diffraction points because the reflection law is not satisfied at these points. Therefore, the scatterer surface should be replaced with the plane which satisfies the reflection law. The plane is specified by the modified surface-normal vector $\hat{n}_{mod}$ [3.17]. One out of two types of the modified surface-normal vectors are selectively used; $\hat{n}_r$ and $\hat{n}_i$ satisfy the reflection law for the observation point, source and image source, respectively, as

$$\hat{n}_r = \frac{\hat{k}_d - \hat{k}_i}{\hat{k}_d - \hat{k}_i} \tag{3.4}$$

$$\hat{n}_i = -\frac{\hat{k}_d - \hat{k}_{im}}{\hat{k}_d - \hat{k}_{im}} \tag{3.5}$$

where $\hat{k}_i$ and $\hat{k}_{im}$ are the propagation vectors indicating the incident direction from the source and its image, respectively, and $\hat{k}_d$ is the normal vector along with the direction to observation (see Fig. 3.2). Here, the selection of $\hat{n}_r$ or $\hat{n}_i$ depends upon the observer's position; for the observer on the front side or on the back side, $\hat{n}_r$ or $\hat{n}_i$ is selectively adopted, according to the following equation,

$$\hat{n}_{mod} = \begin{cases} \hat{n}_r & \text{FrontSide} : |\hat{n} \cdot \hat{n}_r| \geq |\hat{n} \cdot \hat{n}_i| \\ \hat{n}_i & \text{BackSide} : |\hat{n} \cdot \hat{n}_r| < |\hat{n} \cdot \hat{n}_i| \end{cases} \tag{3.6}$$

where $\hat{n}$ is the actual surface-normal vector at the diffraction points. The localization area will be specified not on the actual scatterer surface but on the fictitious surface defined by $\hat{n}_{mod}$ as shown in the right side of Fig. 3.1. At that moment, the conditions of (3.1) to (3.3) will be replaced with the following ones;

$$n_E = \frac{|L_{SE} + L_{EO} - L_{SO}|}{\lambda/2} \tag{3.7}$$

$$n = \frac{|L_{SI'} + L_{I'O} - L_{SO}|}{\lambda/2} \tag{3.8}$$

$$|n - n_E| = \Delta n \leq \Delta n_B \tag{3.9}$$

where the point (I') indicates a point of interest on the imaginary infinite plane tangential to $\hat{n}_{mod}$. Note that the right side of Fig. 3.1 displays the example for $\hat{n}_{mod} = \hat{n}_r$ case. In the case of $\hat{n}_{mod} = \hat{n}_i$, the local area should be determined with respect to not the source position (S) but the image source position (S').

Next, we determine a windowing value by using the EYE function as

$$EYE\left(\frac{\Delta n}{\Delta n_B}\right) = \begin{cases} \cos^2\left(\dfrac{\Delta n}{\Delta n_B} \cdot \dfrac{\pi}{2}\right) & \Delta n \leq \Delta n_B \\ 0 & \Delta n > \Delta n_B. \end{cases} \tag{3.10}$$

on the imaginary infinite plane. Finally, the localized (truncated) area and windowing value defined on the imaginary plate is projected onto the actual scatterer surface. In conclusion, the local integration areas on the actual scatterer are identified.

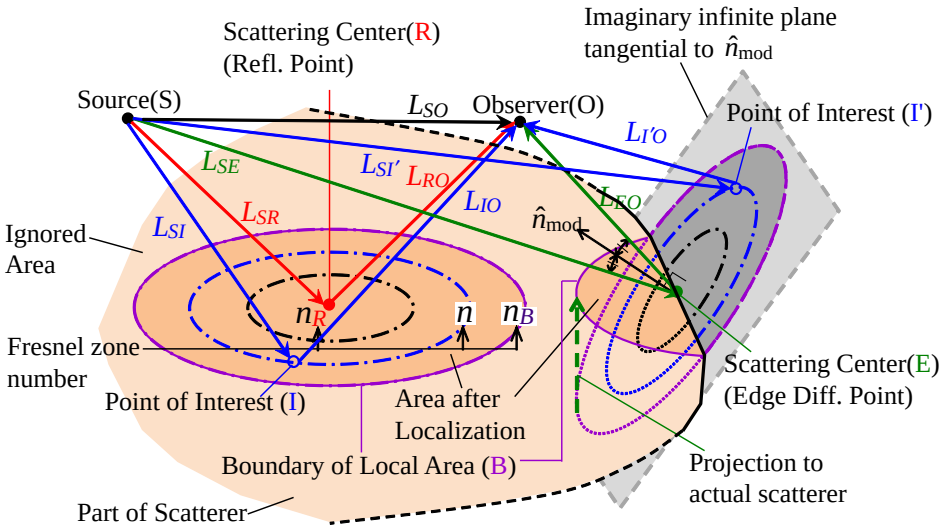

Figure 3.1: Localization for both of the reflection and diffraction points.

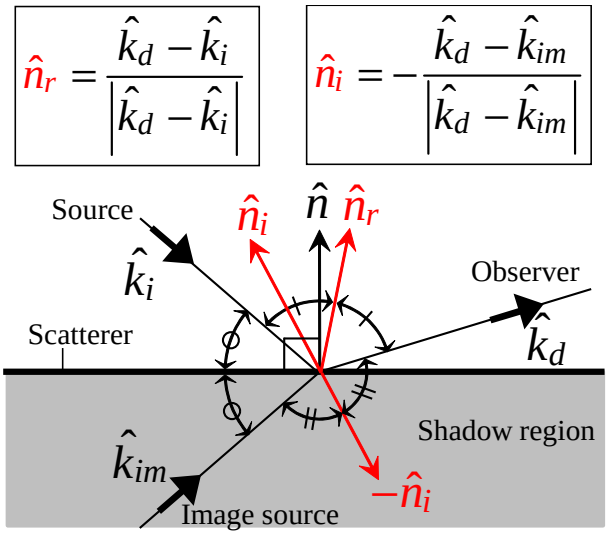

Figure 3.2: Definition of modified surface-normal vector.

3.2.2 Treatment of Overlapped Local Areas

When the inner SPP (reflection point) and diffraction points or the different diffraction points get close together, the local areas for each point are overlapped and the windowing values are multiply defined. Fig. 3.3(a) shows the case when the reflection point and diffraction point are close together and the windowing value are multiply defined around $x = x_c$. In that case, the shape of final local areas is determined by merging the different local areas. There are however several ways to determine the final windowing value. In the literature of [3.18], a maximum-value rule was adopted. Let EYE_i be a windowing value based on (3.10) with respect to an i-th scattering center (in Fig. 3.3, $i = 1$ indicates the reflection point at $x = x_s$, and $i = 2$ indicates the diffraction point at $x = x_1$). The final windowing value W following the maximum-value rule is expressed as

$$W = EYE_{i_{\max}} = \max_i EYE_i \tag{3.11}$$

$$i_{\max} = \arg\max_i EYE_i. \tag{3.12}$$

The maximum-value rule however has a problem; distribution of final windowing value has a discontinuity of the first derivative value at some points on a scatterer (See the distribution at $x = x_c$ in Fig. 3.3(a) or Fig. 3.3(e)) and these points would produce the undesired contributions. In order to cope with it, a smoothing rule was proposed in [3.19]. The correction term ΔEYE is added (3.11) as follows.

$$W = EYE_{i_{\max}} + \Delta EYE \tag{3.13}$$

$$\Delta EYE = \frac{1}{2}\sum_i |\hat{\sigma}_{i_{\max}} - \hat{\sigma}_i| \cdot (1 - EYE_{i_{\max}}) \cdot EYE_i \tag{3.14}$$

$$\hat{\sigma}_i = -\frac{\nabla_s (EYE_i)}{|\nabla_s (EYE_i)|} = \frac{\nabla_s (\Delta n)}{|\nabla_s (\Delta n)|} \tag{3.15}$$

∇_s in (3.15) is a vector differential operator regarding two unit vectors which construct a coordinate system on a scatterer's surface, that is, $\nabla_s = \nabla - \hat{n}\,(\hat{n} \cdot \nabla)$. The unit vector $\hat{\sigma}_i$ was also introduced in the context of the modified edge representation (MER) [3.20]. Fig. 3.3(e) shows the distribution of windowing value considering ΔEYE. The discontinuities around $x = x_c$ disappear due to the correction term ΔEYE. Note that ΔEYE of (3.14) naturally has a feature which correct windowing values on a medium area between nearby scattering centers and hardly works on the other area.

Comparison of the maximum-value rule and the smoothing rule will be numerically done in the next subsection.

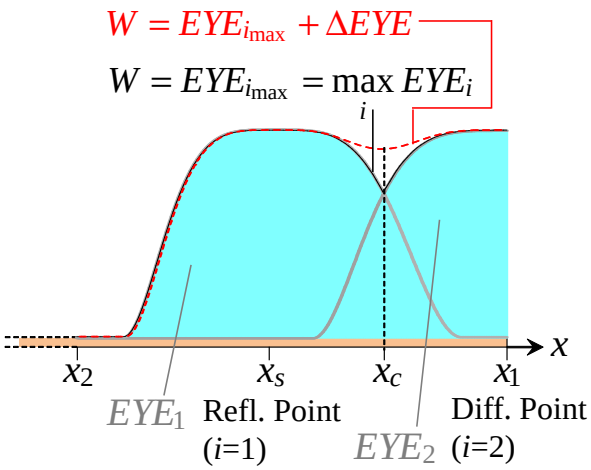

(a) Windowing on x-axis.

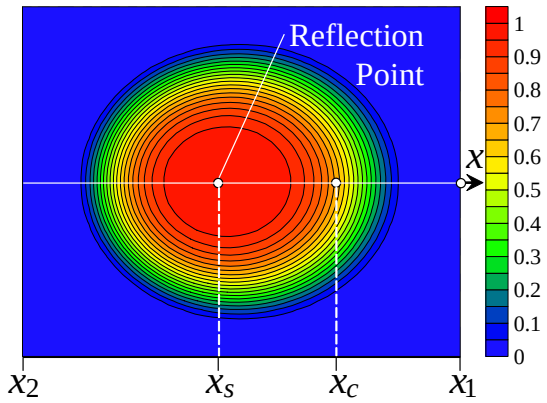

(b) Reflection point only.

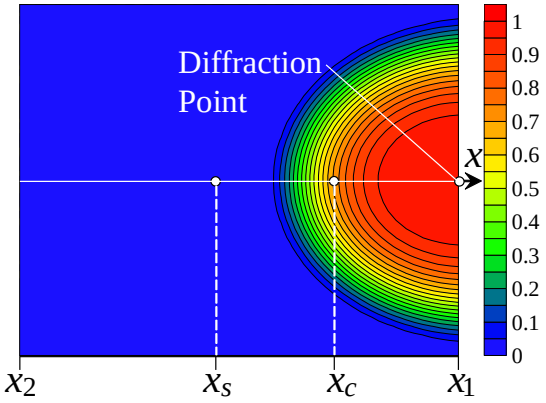

(c) Diffraction point only.

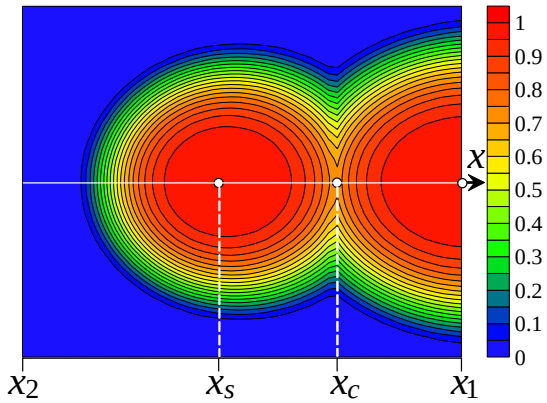

(d) Final windowing value based on the maximum-value rule.

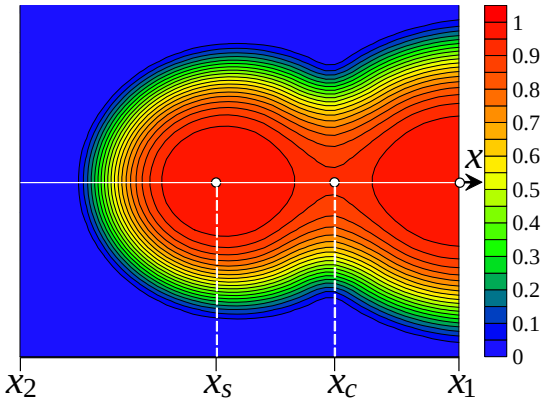

(e) Final windowing value based on the smoothing rule.

Figure 3.3: Windowing for nearby scattering centers. (a) Geometry of problem and windowing values on x-axis (b)˜(e) Distributions of windowing values for various situations.

3.3 Numerical Results

3.3.1 Radiation Integrals for Calculation of Scattered and Total Field Patterns

A. A Flat Scatterer: Scattered Fields and Windowing Value Distribution

All results from here, except Fig. 3.6, were calculated under the condition of $\Delta n_B = 3$. Fig. 3.4 shows the computational model. A perfect electric conductor (PEC) square plate with $50\lambda \times 50\lambda$ size is illuminated by an x-directed dipole on the z-axis at a distance of 50λ. Fig. 3.5 shows scattered field patterns in two planes of observation $\phi = 0°$ and $45°$. The geometrical reflection and incident shadow boundary (RSB and ISB, respectively) are also drawn in the graphs. Here we used the smoothing rule for determining windowing value, although the the effect by selection of rules is not significant in the scattered field pattern so the results by both the rules are indistinguishably matched. The radiation integral is conducted over the reduced area and weighted with the EYE function in (3.10) using $\Delta n_B = 3$. This is much smaller than the previous results $\Delta n_B = 6$ and 4 for the inner SPP and the edge in [3.16] The results by the whole area integration are also presented as the references. The localization does not deteriorate scattering field at all. The dashed line indicates an occupation ratio of the local areas against the whole ones (refer to the right vertical axis). The ratio varies with the observation angle and is always below 43%. It is noted that the result for $\phi = 45°$, especially, for the angle θ between RSB and $90°$ where only corner diffraction points survive and the other scattering centers vanish, assures that the localization algorithm works well for a typical 3-dimensional problem, while the result of $\phi = 0°$ has a similarity with a 2-dimensional problem in the sense that the reflection point and edge diffraction points are located on one axis. Fig. 3.6 presents the scattered field for various values of Δn_B from $50°$ to $90°$ at $\phi = 0°$ plane, where the reflection point vanishes and only diffraction waves exist in terms of ray optics. Errors were observed in $\Delta n_B = 2$ case while that of $\Delta n_B \geq 3$ is almost perfect. This result shows that the criterion of $\Delta n_B = 3$ is also valid and large enough for edge and corner diffraction points.

Fig. 3.7 and Fig. 3.8 show the distributions of windowing values for various observation angles. They were calculated based on the smoothing rule. In both of the $\phi = 0°$ and $\phi = 45°$ plane, the shape and windowing value smoothly vary depending on θ. Although the local area for the reflection point vanishes when the observer transverses the RSB, the distribution of windowing values continuously changes. This property ensures a continuity of a scattered field unlike geometrical optics (GO) or GTD's field.

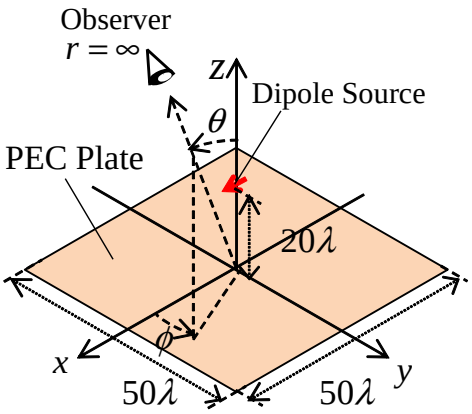

Figure 3.4: Computational model. A PEC rectangular plate illuminated by dipole.

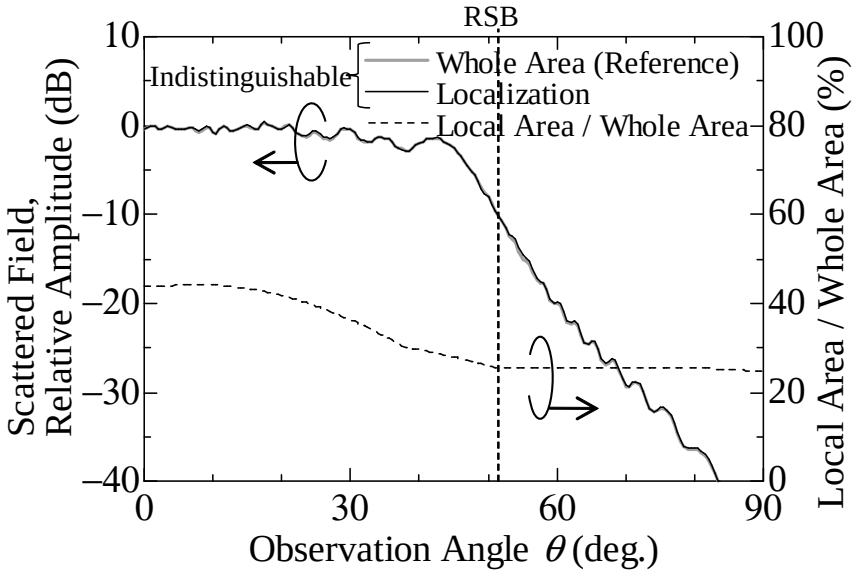

(a) $\phi = 0°$

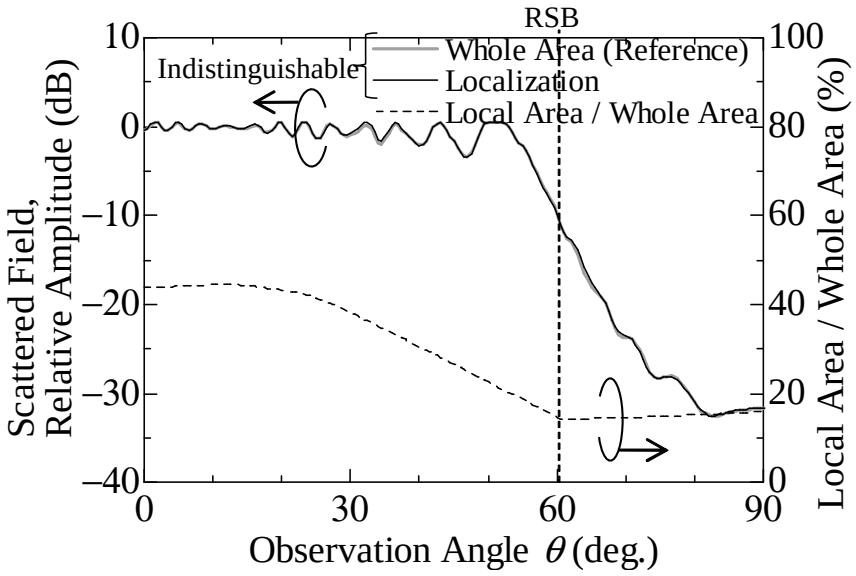

(b) $\phi = 45°$

Figure 3.5: Scattered field from a rectangular plate ($\Delta n_B = 3$).

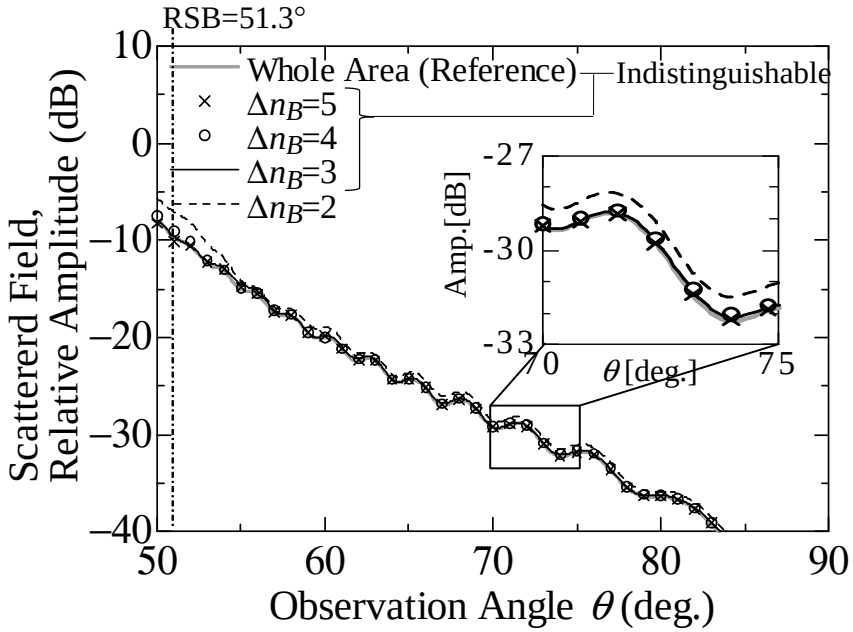

Figure 3.6: Scattered field for various values of Δn_B when there is no reflection point.

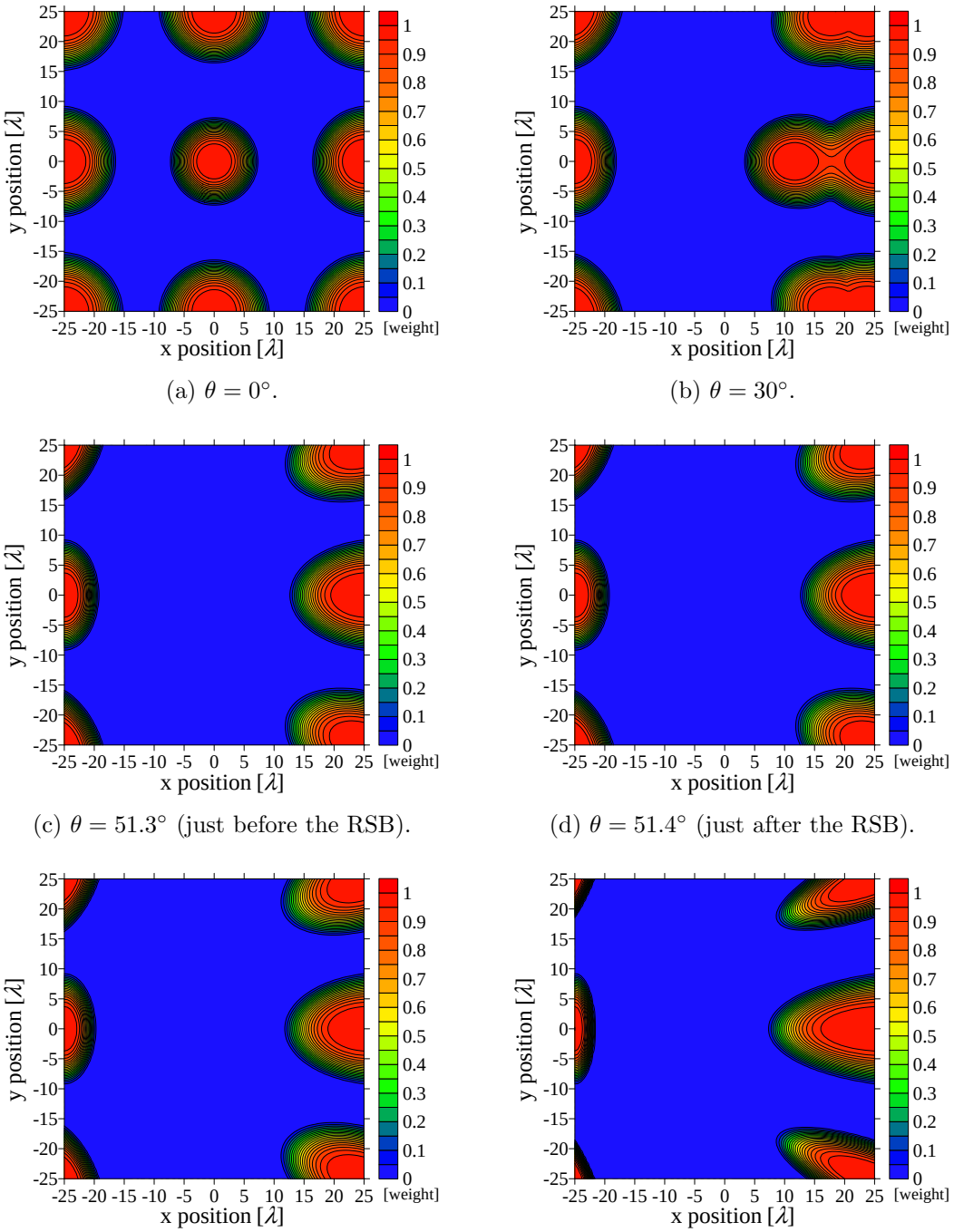

(a) $\theta = 0°$.

(b) $\theta = 30°$.

(c) $\theta = 51.3°$ (just before the RSB).

(d) $\theta = 51.4°$ (just after the RSB).

(e) $\theta = 60°$.

(f) $\theta = 90°$.

Figure 3.7: Distribution of windowing value for various θ value at $\phi = 0°$.

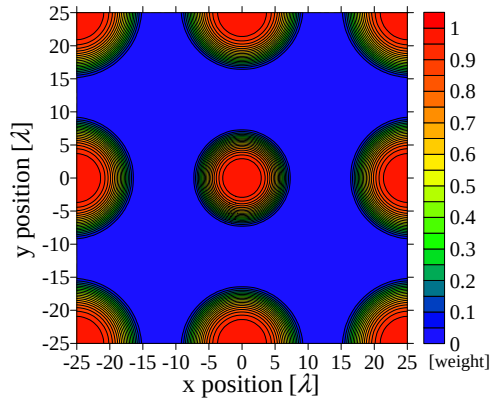

(a) $\theta = 0°$.

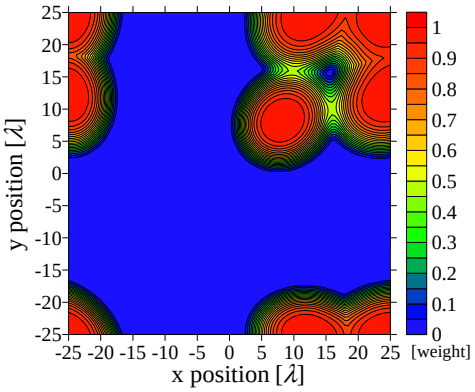

(b) $\theta = 30°$.

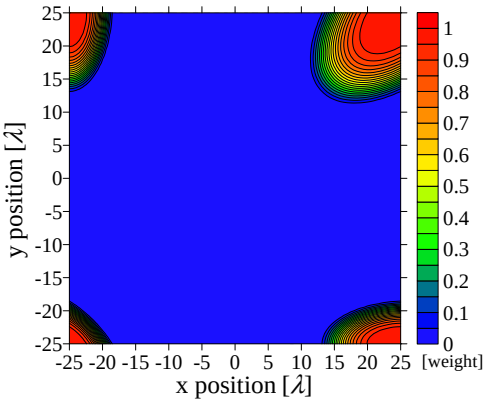

(c) $\theta = 60.5°$ (just before the RSB).

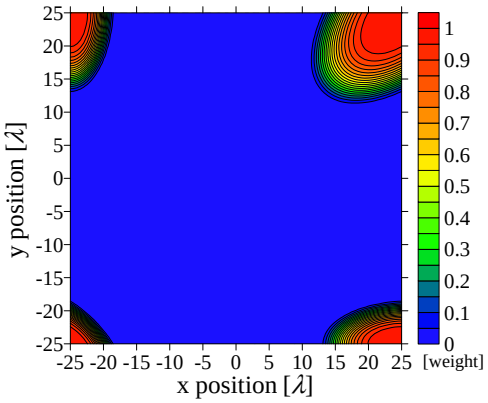

(d) $\theta = 60.6°$ (just after the RSB).

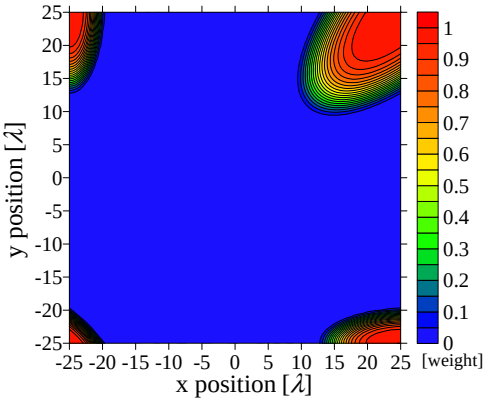

(e) $\theta = 60°$.

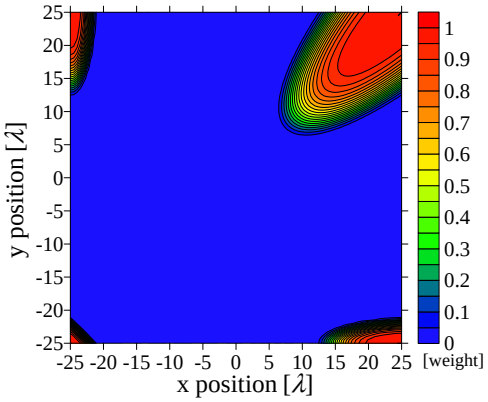

(f) $\theta = 90°$.

Figure 3.8: Distribution of windowing value for various θ value at $\phi = 45°$.

B. A Flat Scatterer Case: Total Field Patterns and Comparison of Windowing Rules

A total field pattern is more sensitive to errors than a scattered field since the total field is the sum of the scattered field and the incident wave and a phase error of scattered field becomes notable. Fig. 3.9 compares the total field patterns calculated by the maximum-value rule and the smoothing rule as well as the whole area integration. The patterns of both of the rules are in good agreement with the whole integration. However, as for the maximum-value rule, some errors are notable in the angles of $130^\circ \leq \theta \leq 160^\circ$ at $\phi = 0^\circ$ plane and $130^\circ \leq \theta \leq 150^\circ$ at $\phi = 45^\circ$ plane. These error comes from the discontinuities of windowing value distribution. Not that the scattered field by the maximum-value rule has also the same error on the front side because the windowing value distribution at θ is same as that at the angle of $180^\circ - \theta$. The errors however are not notable because the incident waves, exactly calculated, are dominant on the front side. This graph explicitly shows the superiority of the smoothing rule. The smoothing rule will be always used from the next chapter.

The generality of localization method is high. Fig. 3.10 is also a total field when the dipole source turns to z-direction and the other conditions are unchanged. Also in this case, the field can be produced accurately.

The localization of radiation integrals is also valid for numerically-exact currents by the MoM. Total field patterns by the whole integration and localization with the smoothing rule are compared in Fig. 3.11. The computation model is similar to the one of Fig. 3.4 but the size is slightly smaller due to the memory limitation in MoM-based simulator Wipl-D as the reference; 40λ on a side illuminated by a half wavelength dipole at 16λ high. It is confirmed that the proposed approximation is still effective for the realistic currents analyzed by the MoM.

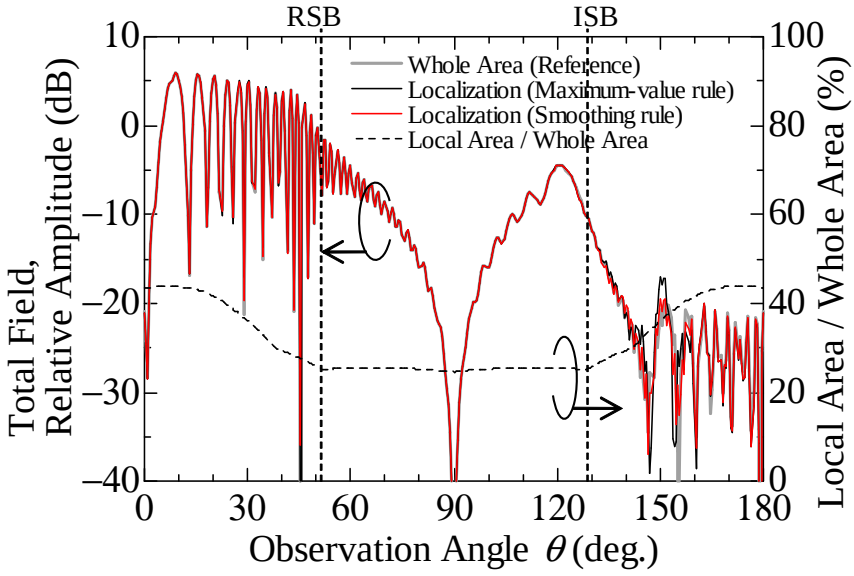

(a) $\phi = 0°$ plane.

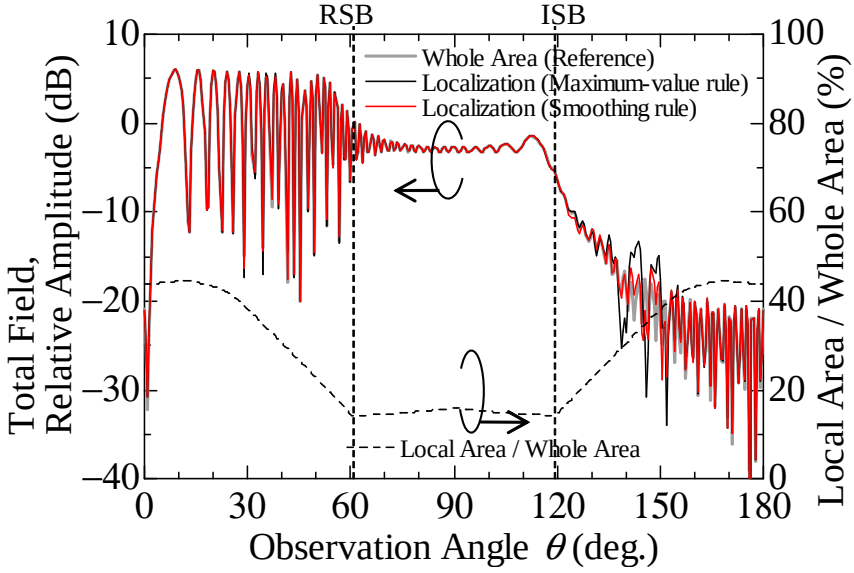

(b) $\phi = 45°$ plane.

Figure 3.9: Total field from a rectangular plate and an x-directed dipole source.

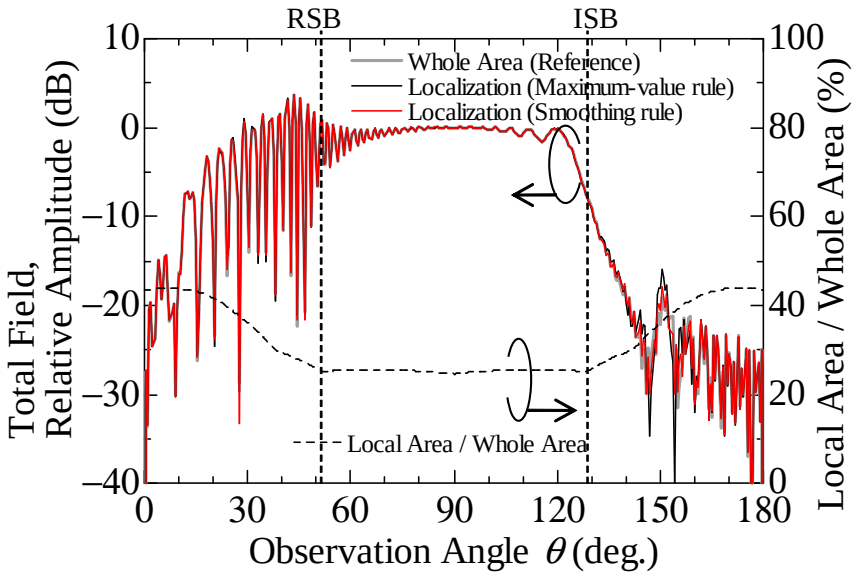

Figure 3.10: Total field from a rectangular plate and an z-directed dipole source.

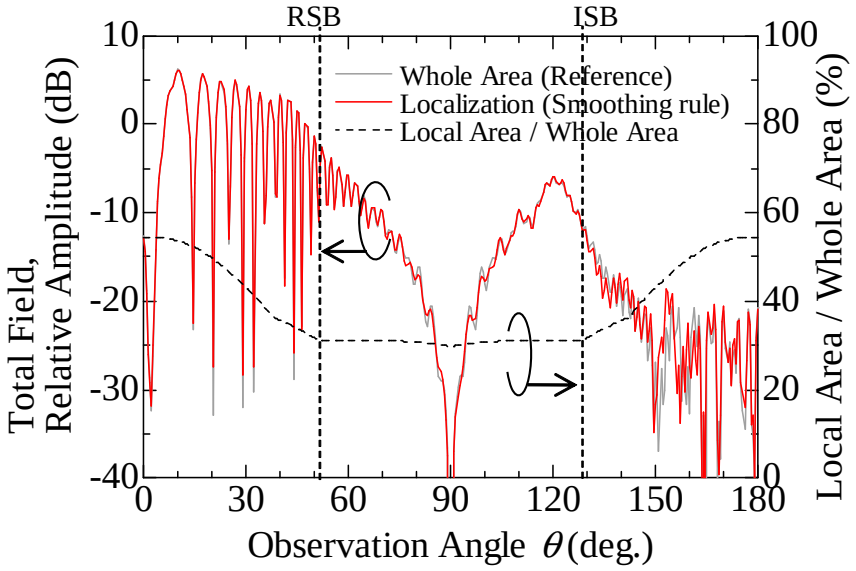

Figure 3.11: Total field calculated by radiation integral of MoM currents. The dimensions of a rectangular plate change to $40\lambda \times 40\lambda$ and the x-directed dipole source is at 16λ high.

C. A Curved Scatterer Case

The localization of radiation integral is also valid for a curved scatterer as Fig. 3.12. When the angle θ is neither 0° or 180°, there are two diffraction points on the periphery (see

Fig. 3.12) while $\theta = 0°$ and 180° are the caustics and every point on the periphery becomes a diffraction point. Therefore results at $\theta = 0.01°$ and 179.99° are used as that at $\theta = 0°$ and 180°, respectively. The two patterns are matched well so the validity of the localization was confirmed.

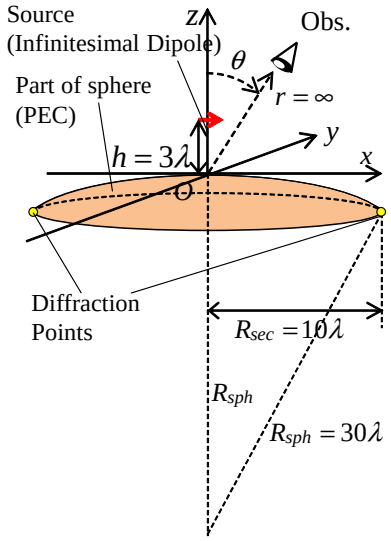

Figure 3.12: Computational model. A part of PEC sphere illuminated by dipole.

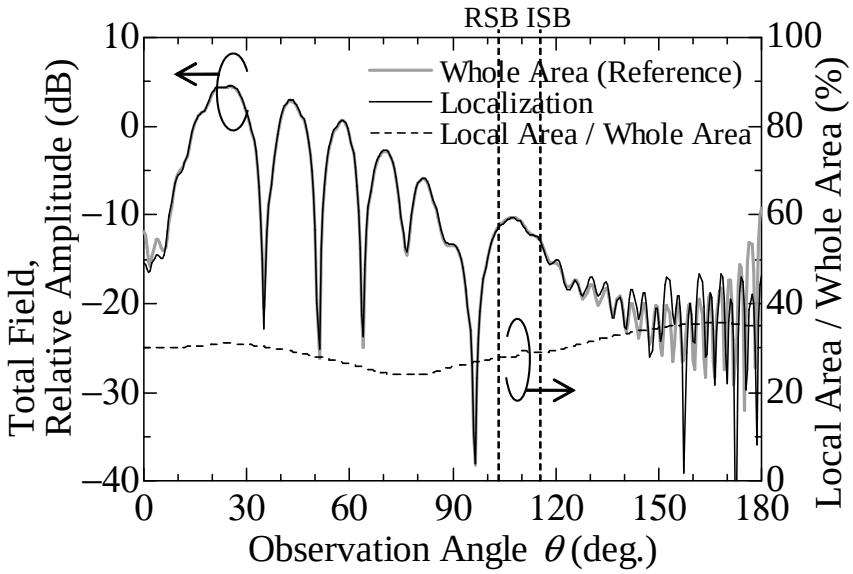

Figure 3.13: Total field form a part of PEC sphere and a dipole source.

3.3.2 Frequency Dependence of Occupation Ratio

Fig. 3.14 summarizes the frequency dependence of the occupation ratio of local area to whole one for several observation angles θ. At higher frequencies, the ratio is inversely proportional to the frequency. This means that the computational load reduction would be enhanced in higher frequency. This is also depicted at the bottom of Fig. 3.14 by comparing the local areas at $\theta = 30°$ in original and 10-times frequency. Obviously, the local areas shrink as frequency gets higher. Note that the electrical surface size (λ^2) of local areas itself increase for higher frequencies as discussed in the chapter 2. However, since the electrical size of whole area against frequency increase at a higher rate than that of local areas, the occupation ratio itself decrease for higher frequency. This characteristic of the ratio means that frequency dependence of computational complexity regarding radiation integrals is suppressed from $O(f^2)$ to $O(f)$ level.

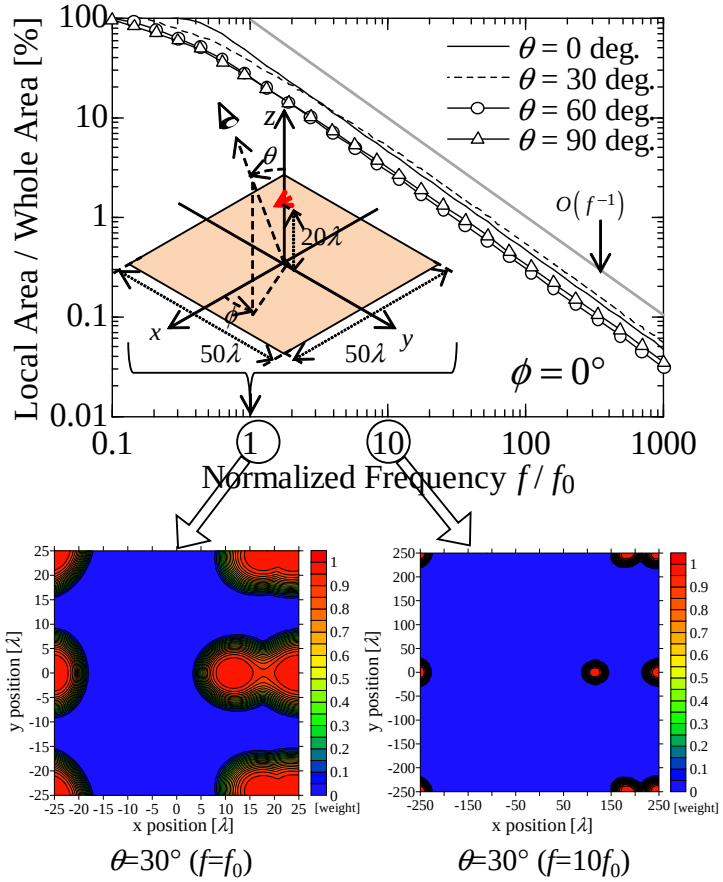

Figure 3.14: Frequency dependence of the occupation ratio of local area to whole area and visuals of local areas.

3.4 Concluding Remarks

The localization of radiation integrals was introduced in this chapter. The techniques to apply the localization method to an arbitrary point including diffraction points were also introduced. Various scattering centers, such as the reflection point and the diffraction points, can be localized uniformly with the same criteria of $\Delta n_B = 3$ by utilizing the modified-surface normal vector. We compared two rules to determine a final windowing value, the maximum-value rule and the smoothing rule. We concluded that the smoothing rule is better because the correction term ΔEYE, which considers $\hat{\sigma}_i$ vectors, eliminates a discontinuity of the first derivative value of windowing value and it leads to enhanced accuracy of total field pattern. The algorithm was successfully applied to the scattering analyses for a flat square plate and a part of sphere. The localization is valid for numerically exact currents by the MoM as well as approximated currents by PO.

References

[3.1] R.F. Harrington, *Field Computation by Moment Methods*, IEEE Press, New York, 1993.

[3.2] J. Jin, *The Finite Element Method in Electromagnetics*, John Wiley and Sons, 1993.

[3.3] J. L. Volakis, A. Chatterjee, and L. C. Kempel, *Finite Element Method for Electromagnetics* IEEE Press, 1998.

[3.4] A. Taflove and S. C. Hagness, *Computational Electrodynamics: The Finite-Difference Time-Domain Method*, Artech House, 3rd editon, 2005.

[3.5] K. Kunz and R. Luebbers, *The Finite Difference Time Domain Method for Electromagnetics*, CRC Press, 1993.

[3.6] J. B. Keller, "Geometrical theory of diffraction," *Journal of the Optical Society of America*, vol.52, pp116-130, 1962.

[3.7] R. G. Kouyoumjian and R. H. Pathak, "A uniform geometrical theory of diffraction for an edge in a perfectly conducting surface," *Proceedings of the IEEE*, vol.62, no.11, pp.1448-1461, Nov. 1974.

[3.8] P. Y. Ufimtsev, "Elementary edge waves and the physical theory of diffraction," *Electromagnetics*, vol.11, iss.2, pp.125160, 1991.

[3.9] M. Ando, "Radiation pattern analysis of reflector antennas," *IEICE Transaction on Communication (Japanese Edition)*, J67-B, no.8, pp.853-860, Aug. 1984.

[3.10] T. Shijo, T. Itoh, M. Ando, "Visualization of high frequency diffraction based on physical optics," *IEICE Transaction on Electronics* vol.E87-C, no.9, pp.1607-1614, Sep. 2004.

[3.11] R. F. Harrington, *Time-Harmonic Electromagnetic Fields*, pp.127-130, McGraw-Hill, New York. 1961.

[3.12] C. S. Kim, Y. Rahmat-Samii, "Low profile antenna study using the physical optics hybrid method (POHM)", *in the Digest of IEEE International Symposium on Antennas and Propagation (AP-S)*, vol. 29, pp.1350-1353, June 1991.

[3.13] U. Jakobus and F.M. Landstorfer, "Improvement of the PO-MoM hybrid method by accounting for effects of perfectly conducting wedges," *IEEE Transaction on Antennas and Propagation*, vol.43, no.10, pp.11231129, Oct. 1995.

[3.14] Z.-L. Liu, X. Wang and C.-F. Wang, "Installed Performance Modeling of Complex Antenna Array Mounted on Extremely Large-Scale Platform Using Fast MoM-PO Hybrid Framework," *IEEE Transaction on Antennas and Propagation*, vol.62, no.7, pp.3852-3858, July 2014.

[3.15] T. Shijo, T. Hirano, and M. Ando, "Large-Size Local- Domain Basis Functions with Phase Detour and Fresnel Zone Threshold for Sparse Reaction Matrix in the Method of Moments," *IEICE Transaction on Electronics.*, Vol.E88-C, No.12, pp.2208-2215, Dec. 2005.

[3.16] K. Ito, T. Shijo, M. Ando, "Fresnel zone criterion to implement locality in the method of moments and PO-MoM hybrid method for the reduction of unknowns," *IEICE Transaction on Electronics*, vol.E94-C, no.1, pp72-79, Jan. 2011.

[3.17] T. Shijo, L. Rodriguez, and M. Ando "The Modified Surface-Normal Vectors in the Physical Optics," *IEEE Transaction on Antennas and Propagation*, Vol.56, No.12, pp.3714-3722, Dec. 2008.

[3.18] T. Kohama and M. Ando, "Localization of Radiation Integrals Using the Fresnel Zone Numbers," *IEICE Transaction on Electronics* vol.E95-C, no.5, pp.928-935, May. 2012.

[3.19] T. Kohama and M. Ando, "Novel Techniques for Abbreviated Analysis of High Frequency Scattering Using the Fresnel Zone Numbers," *IEEE International Symposium on Antennas and Propagation (AP-S)*, Session: 533.4, Orlando, FL, USA, July 7-13, 2013.

[3.20] K. Sakina, M. Ando, "Mathematical derivation of modified edge representation for reduction of surface radiation integral," *IEICE Transaction on Electronics*, vol.E-84-C,no.1,p.74-83, Jan. 2001.

Chapter 4

Physical Optics Radiation Integrals with Frequency -Independent Number of Division utilizing Fresnel Zone Number Localization and Adaptive Sampling Method

4.1 Introductory Remarks

The efficient and accurate computation of the scattering fields from electrically large scatterers is one of the important problems in the antenna and propagation areas such as the gain estimation of the reflector antenna or the radar analysis. The physical optics (PO) approximation [4.1, 2] is one of the techniques to calculate them with a reasonable accuracy in the high frequency region. The PO has been widely used to analyze scattering fields from the electrically large conducting scatterers such as the reflector antennas [4.3]. This is also being applied to a radio propagation or wireless communication environmental analysis in high frequency such as the UHF band [4.4].

The PO assumes induced currents only on the lit surface and a zero current on the unlit surface as follows;

$$\boldsymbol{J}_{PO} = \begin{cases} 2\hat{n} \times \boldsymbol{H}_i & \text{lit region} \\ 0 & \text{unlit region} \end{cases} \tag{4.1}$$

where the $\hat{n}$ is the surface-normal vector and $\boldsymbol{H}_i$ is the incident magnetic field on the surface. The field radiated from PO currents can be computed by the radiation integrals over the whole surface. In order to evaluate the radiation integral numerically, the integration area must be divided into small segments and a certain constant and short value compared to the wavelength is chosen as this size. The required CPU time of the PO is usually proportional to the scatterer's electrical size which basically increases in proportion to the first power of the frequency (2-D case) or the second power of the frequency (3-D case); the PO calculation therefore becomes extremely heavy at higher frequencies.

In order to alleviate this load, a variety of techniques have been proposed. The evaluation of the PO integrals by the asymptotic method such as stationary phase method (SP) [4.5] is a classical technique but has been often used because of its usefulness. The SP is the mathematical asymptotic techniques that replace the integration of the rapidly-

oscillating function with the contributions from the stationary phase points at which it takes the extreme value. In other words, the SP is said to be the method to lower the dimension of the domain of the integration. In the 3-dimensional scattering problem, the radiation integral is the double (surface) integral. If the SP is applied once, the surface integral is transformed to the single (line) integration along the contour of the scatterer. The equivalent edge currents (EECs) are the line currents to be integrated along the periphery of the scatterers, which are regarded as the results of the SP applied to the surface integration once: variety types of definition of EECs have been proposed in history which have the identical asymptotic behaviors [4.6–11]. Furthermore, the line integration can be transformed into the contribution from some specific points if the SP is applied once more [4.12]. These points are so-called "scattering centers" such as the reflection point or the edge diffraction points which are leading terms in high frequency techniques such as the Geometrical Theory of Diffraction [4.13]. The SP technique is the asymptotic method thus calculation results become singular in some observation points, for instance, when an observer is at the reflection shadow boundary, the caustics and so on.

Another mathematical approach is also developed where the amplitude and phase of the integrand is approximated and expanded in terms of the low-order polynomial functions which are integrable in the closed-form[4.14–17].

The adaptive sampling method (ASM) proposed by Burkholder [4.20] is the technique to reduce the sampling point in the PO numerical integration. He pointed out that the usual sampling criterion, which is based on the wavelength and is so-called "Nyquist sampling", often causes over-sampling. In order to cope with this, he proposed another criterion based on the phase changes of the integrand which is so-called "adaptive sampling".

We proposed a quite different approach named "Localization of the radiation integrals." [4.21, 22] This technique has some of the common points in the SP technique however the dimension of the domain of integration doesn't become lower and only the size reduction or localization takes place. This localization method suggests that only the small portions of the integration with a slow phase change contribute to the scattering field. This idea comes from the local property of scattering phenomena as mentioned in the chapter 2. In order to extract the locality and truncate the areas with strong contribution appropriately, we have proposed the use of Fresnel zone number as the generalized criterion and the argument in the weighting function.

In this chapter, we newly introduce the ASM in the localization method. In principle, the proposed method provides the frequency-independent number of division in the radiation integrals and the computational time and accuracy. Furthermore, this method introduces no singularity unlike the SP and EEC techniques.

The proposed method is applied to the radar cross section (RCS) analysis by PO for

2-dimensional structure. Time dependence of $\exp(j\omega t)$ is assumed and suppressed, where ω is the angular frequency. λ and k are the wavelength and wavenumber, where $k = 2\pi/\lambda$, respectively. By the way, the practical computation of scattering covers the numbers of the sampling points of observation angles and also one of frequencies. These also increase depending on the frequency [4.18, 19]. Consequently, the multiplication of the three terms gives the load on computation, that is, a scatterer's electrical size, number of sampling points of observation points and one of frequencies determine the computational load. The techniques we have reviewed so far are aimed for a computational load reduction regarding the first one, that is, the electrical size. Of course, some of the methods aimed for the other two terms have also been proposed and developed; the Fast Physical Optics (FPO) [4.18] and Multilevel Physical Optics [4.19] are the representative method of these. Therefore, the method developed in this paper, classified into the techniques to reduce computational cost about the first term, may be combined with the FPO and MLPO for reducing the number of sampling points and frequencies, and leads to a more efficient computation in practical applications.

4.2 Adaptive Sampling Method in the Fresnel Zone Number Localization

In this subsection, we compare the usual sampling method, so-called "Nyquist sampling," and the adaptive sampling method which was introduced in [4.20].

Usually, the sampling rate is determined by the criterion of the Nyquist sampling rate. According to this criterion, the integration area is divided into the equal- and small-size segments. A small value compared to the wavelength is usually chosen as that size of Δx; for instance $\lambda/20$ or $\lambda/10$ (See Fig. 4.1(a)) depending upon the accuracy required. If the frequency f becomes higher for the given physical size of the systems, the total number of divisions increases proportional to the electrical size of total integration areas, viz. $O(f)$ in the 3-D case, or $O(f^2)$ in the 2-D case. This brings about the heavy computational load in the high frequency region. Another difficulty of the over-sampling was pointed out in [4.20]. "Adaptive sampling" is a criterion to cope with this problem. The integrand in the radiation integral can be generally expressed as (4.2). $G(x)$ is the envelope of the integrand and $f(x)$ is the path length from the source to the observer via the integration point.

$$I = \iint_S G(x)\, e^{-jkf(x)} dx \tag{4.2}$$

This ASM is the method to adaptively divide the integration area so that the phase

change of the integrand, that is, the variation of $kf(x)$ in one segment should be a certain constant value of $\Delta\alpha$; for instance, $\pi/10$ or $\pi/20$ (See Fig. 4.1(b)). Since one hump of the waves (or, half oscillation) corresponds to the π phase changes, this criterion can be interpreted as the method to divide the hump of the wave into 10 or 20 segments.

Here, let us consider the frequency dependence of total number of divisions when we introduce the ASM in the localization method. Based on the localization method, (4.2) will be converted into the following form in terms of the Fresnel zone number.

$$I \approx \iint_S EYE\left(\frac{\Delta n}{\Delta n_B}\right) G(x)\, e^{-j\pi(\Delta n + n_R)} dx. \tag{4.3}$$

To facilitate numerical evaluation, (4.3) can be transformed into a summation of discrete terms. If we adopt the ASM and we put $\delta = \Delta\alpha/k$, which corresponds a step value of the Fresnel zone number in the radiation integral, the discretized version shall be expressed as follows;

$$I \approx e^{-jkn_R} \sum_{i=0}^{N_{FZN}} EYE\left(\frac{i\delta}{\Delta n_B}\right) G(x(i\delta))\, e^{-jk(i\delta)} \Delta x_i \tag{4.4}$$

where Δx_i is a size of an i-th surface segment and $N_{FNZ} = \Delta n_B/\delta$ is the total number of divisions in the numerical radiation integral. This N_{FNZ} is independent of the frequency because both of Δn_B and $\Delta\alpha$ are the criterion value remaining unchanged for frequency. In other words, (4.4) is a frequency-independent form, so the constant CPU time can be achieved.

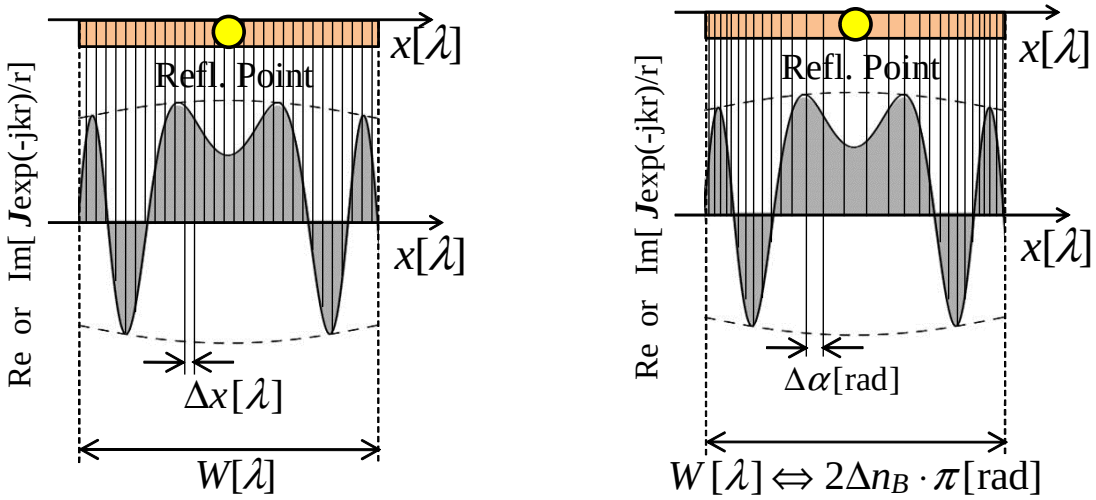

(a) Nyquist Sampling (b) Adaptive Sampling

Figure 4.1: Sampling criteria

4.3 Numerical Results for 2-Dimensional Results

In this subsection, we demonstrate that the adaptive sampling method is better in the sense of the number of sampling points and the computational accuracy when the localization method is adopted. In order to facilitate the discussion, problems which can be analytically evaluated as closed forms will be treated in this section. First, we show the relationship between the number of sampling points and the relative errors for each criterion when the localization method is adopted. The TM plane wave express by (4.5) to (4.7) is incident on the 2-dimensional conducting strip of the width w from the angle of θ as shown in Fig. 4.2(a). The monostatic radar cross section (RCS) from the strip was calculated by PO radiation integrals combined with the localization method.

$$\boldsymbol{k}_i = -\hat{x}\sin\theta - \hat{z}\cos\theta \tag{4.5}$$

$$\boldsymbol{E}_i = (\hat{y} \times \boldsymbol{k}_i)\, E_0 \exp\left(-j\boldsymbol{k}_i \cdot \boldsymbol{r}\right) \tag{4.6}$$

$$\boldsymbol{H}_i = \hat{y}\frac{E_0}{\eta_0} \exp\left(-j\boldsymbol{k}_i \cdot \boldsymbol{r}\right) \tag{4.7}$$

The specific procedure is as follows. First of all, the PO currents are given by (4.1). We evaluated the RCS value of (4.9). Please note that $\sigma_{2\mathrm{D}}$ has the dimension of the length (meter) but $\sigma_{2\mathrm{D}}/\lambda$ is the dimensionless value. At that time we calculated the scattering

electric fields according to (4.11) instead of (4.10). In this model, the scattering centers must be two edge points; the left one (E1) and right one (E2) (see Fig. 4.2(a)). Local areas were determined by the Fresnel zone criterion and the windowing function, EYE function, was applied upon these areas. After that, the numerical integration was conducted following the two types of the division criteria (sampling method); the Nyquist sampling method and the ASM. We calculated the RCS value for each criterion and discussed the convergence tendency of it. The reference value was computed by the usual procedure (the full integration without any weighting function) of PO computation with $\lambda/10000$ interval by using (4.10).

$$\boldsymbol{k}_s = -\boldsymbol{k}_i \tag{4.8}$$

$$\frac{\sigma_{2\mathrm{D}}}{\lambda} = \frac{1}{\lambda} \lim_{r\to\infty} \left\{ 2\pi r \frac{|\boldsymbol{E}_S|^2}{|\boldsymbol{E}_i|^2} \right\} \tag{4.9}$$

$$\boldsymbol{E}_S = -\frac{\omega\mu}{4} \cdot \sqrt{\frac{2j}{\pi k}} \int_{\text{strip}} \boldsymbol{J}_{PO} \exp\left(-j\boldsymbol{k}_s \cdot \boldsymbol{r}\right) dS \tag{4.10}$$

$$\boldsymbol{E}_S = -\frac{\omega\mu}{4} \cdot \sqrt{\frac{2j}{\pi k}} \int_{\Delta n \le \Delta n_B} EYE\left(\frac{\Delta n}{\Delta n_B}\right) \boldsymbol{J}_{PO} \exp\left(-j\boldsymbol{k}_s \cdot \boldsymbol{r}\right) dS \tag{4.11}$$

At first, we show the convergence tendency of the radiation integral results against the division number in the case of the Nyquist sampling. The tendencies for $\theta = 20°, 50°$ and $80°$ in the case of $w = 10\lambda$ are shown in the Fig. 4.3(a). The convergence speeds for each angle are different and tends to be slower for wider angles. In other words, the number of divisions required for a certain constant accuracy becomes larger in the wider angles. The tendencies with a 5 times higher frequency are overlaid on the Fig. 4.3(a). The speeds against the number of divisions per 1 wavelength are unchanged. Therefore, the total number of divisions becomes 5 times larger than the one of the $w = 10\lambda$ case in the proportion to the frequency.

In comparison, the results from the ASM show us the frequency- and observation-angle-independent convergence tendencies. Fig. 4.3(b) shows the tendencies when the ASM is adopted for the strip of $w = 10\lambda$ and $w = 50\lambda$. Three dotted lines for each w value are matched indispensably. This result tells that these tendencies are almost perfectly independent of the observation angles. The speeds of convergence against the number of divisions per one Fresnel zone number are identical for each width of the strip in the same manner as the case of the Nyquist sampling method. In addition to that, the speed against the total number of division does not change at all unlike the previous case. And these

convergence speeds against the total number of division is much faster than ones of the Nyquist sampling method. In addition to that, these 6 lines are matched as if the same conditions were used. This result tells us that the tendency is almost perfectly independent of the observation angles. The advantage of the ASM criterion over the Nyquist one has been shown.

The RCS pattern from the strip conductor with the width of 10λ is shown in Fig. 4.4. PO (Number/Wavelength) in this and following figures means the results by the full integration without any weighting function with $\lambda/10000$ interval. PO (Number/Fresnel zone) is the results by the localization method with the criterion of the adaptive sampling method with $\Delta\alpha = \pi/12$ interval. Note that the value of $\pi/12$ was experimentally found so as to realize less than 0.1 dB difference in the peak values of two patterns in the situation of Fig. 4.2, and that this value might give almost the same accuracy for any other cases. The accurate results are observed not only for the specific angles of $\theta = 20°, 50°$ and $80°$, but also for every angle from $-90°$ to $90°$. The pattern for the case of the rectangular cylinder in Fig. 4.2(b) is shown in Fig. 4.5. The two patterns are well-matched.

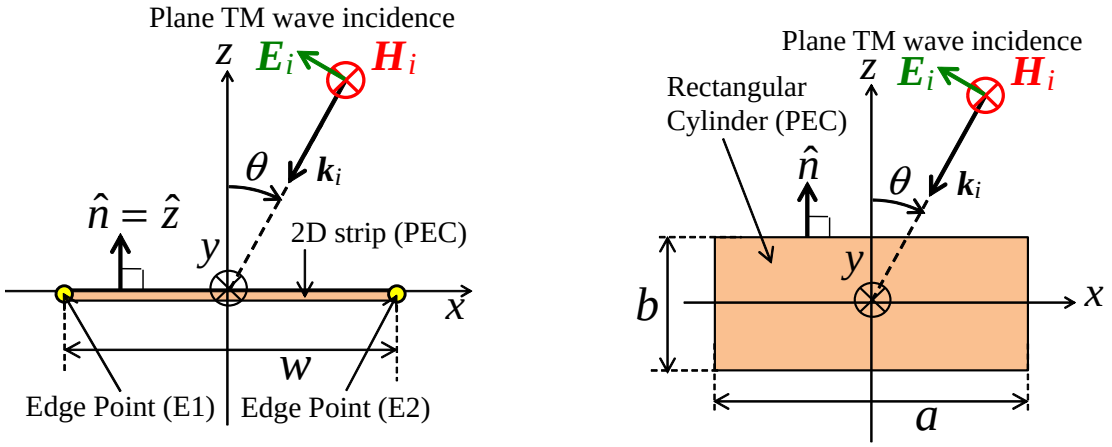

(a) Strip (b) Rectangular cylinder

Figure 4.2: Two-dimensional PEC scatterers with Plane TM wave incidence

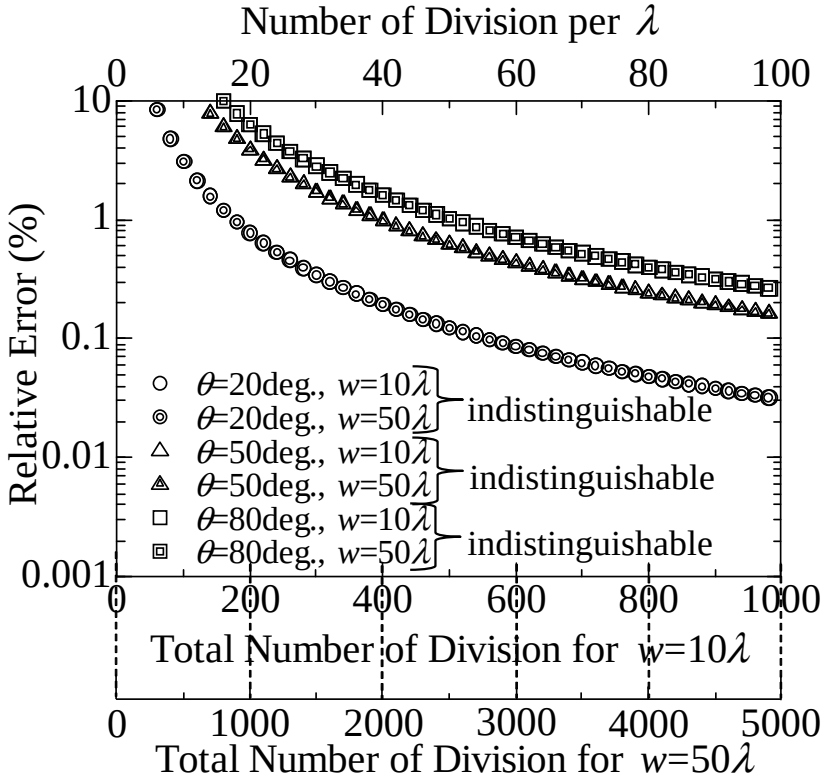

(a) Nyquist sampling method

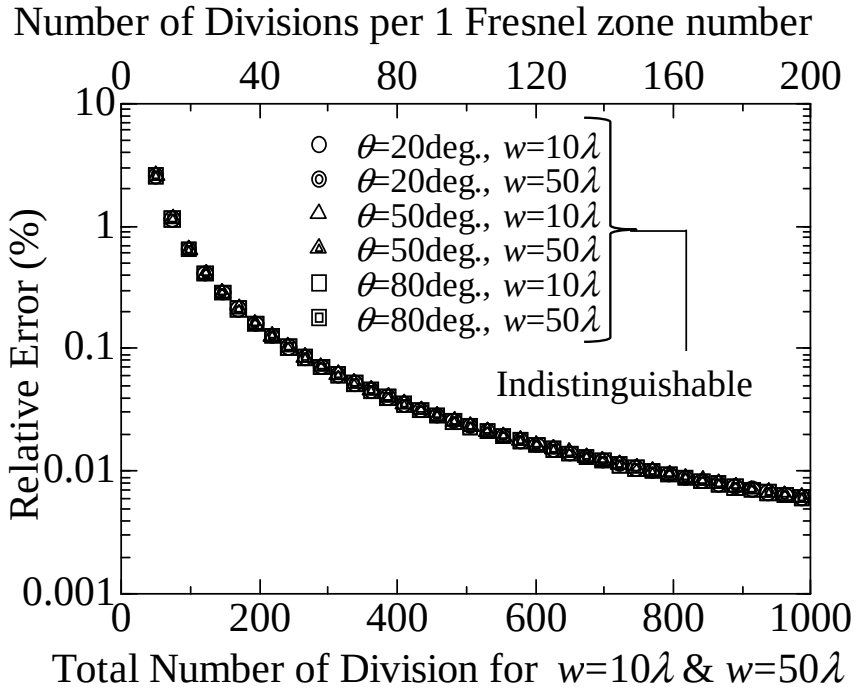

(b) Adaptive sampling method

Figure 4.3: Convergence of the relative error according to the number of divisions

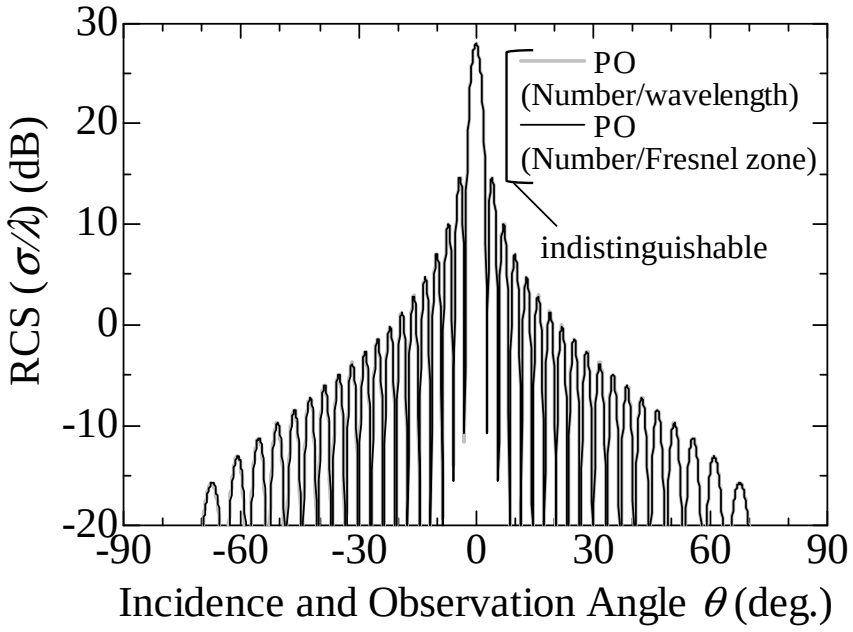

Figure 4.4: RCS pattern for PEC strip ($w = 10\lambda$)

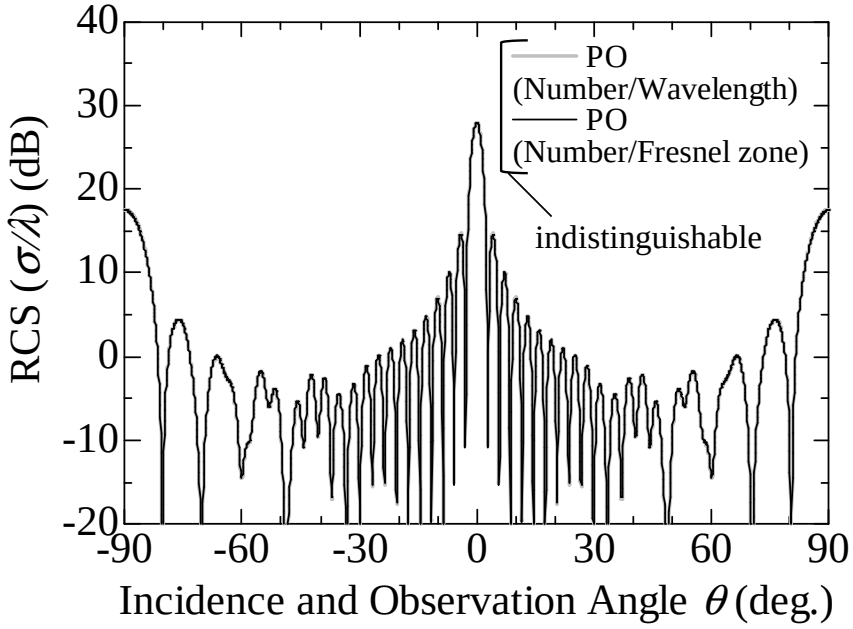

Figure 4.5: RCS pattern for PEC rectangular cylinder ($a = 10\lambda, b = 3\lambda$)

4.4 Frequency Dependence of the Computational Accuracy and Time

In this subsection, we discuss the frequency dependence of the computational accuracy and time for the proposed method. Generally speaking, the accuracy in the numerical integration is enhanced with an increase in the sampling density; however the computational time gets longer in proportion to the density as well. In other words, there is a trade-off relationship between the accuracy and the time in the full integration of PO currents. We therefore have to check the balance of the computational time and the accuracy.

Fig. 4.6 shows the frequency dependence of the CPU time for calculating the monostatic RCS of the conducting strip in Fig. 4.2(a) against the width w. Note that m-times larger width w corresponds to the situation with m-times higher frequency. The CPU time by the usual PO is proportional to the frequency while one by the proposed PO is almost constant and independent of the frequency.

The normalized root-mean-square (RMS) error defined by (4.12), which is the same one as that of [4.18], is also indicated in Fig. 4.6.

$$\Delta_{rms} = \left\{ \frac{\displaystyle\sum_{i=1}^{N_\theta} \left| \boldsymbol{E}_S^{\mathrm{int}}(\theta_i) - \boldsymbol{E}_S^{\mathrm{ref}}(\theta_i) \right|^2}{\displaystyle\sum_{i=1}^{N_\theta} \left| \boldsymbol{E}_S^{\mathrm{ref}}(\theta_i) \right|^2} \right\}^{\frac{1}{2}} \times 100\ [\%] \tag{4.12}$$

$\boldsymbol{E}_S^{\mathrm{ref}}(\theta_i)$ is the reference value computed by usual PO (Number/wavelength) with $\lambda/10000$ interval, $\boldsymbol{E}_S^{\mathrm{int}}(\theta_i)$ is the result to be compared and N_θ is the number of observation sampling points and here we use $N_\theta = 1$. The results of Fig. 4.6 show that the proposed method realizes the constant computational time and accuracy for any frequencies while the RMS error of the results by the usual one is decreasing with higher frequencies. This reason can be explained as follows.

If the frequency becomes m-times higher, the width of the scatterer on one side normalized by the wavelength becomes m-times larger; on the other hand, the width of one oscillation near the scattering center becomes $\sqrt{m}$-times larger. This property has been mentioned in the chapter 2. For this, the Nyquist sampling criterion makes the sampling rate per one oscillation $\sqrt{m}$-times dense.

We confirmed the correctness of the above discussion. Table 1 summarizes the sampling density based on the usual PO, which realizes the almost constant RMS error of $0.45\% \leq \Delta_{rms} \leq 0.50\%$. The third column indicates the predicted sampling density which are derived from $80/\sqrt{m}$, where 80 is the sampling density to realize the RMS error of $0.45\% \leq$

$\Delta_{rms} \leq 0.50\%$ in the case of $w = 10\lambda$ and used as the initial value. The equation of $80/\sqrt{m}$ succeeded in predicting the sampling rate to realize the RMS error of $0.45\% \leq \Delta_{rms} \leq 0.50\%$. From another point of view, it is said that the Nyquist sampling method brings about the over-sampling in the higher frequency region. Note that the paper of [4.20] didn't discuss the frequency dependence of the adaptive sampling rate however it implied that the sampling rate should change adaptively not only for the observation position but for the frequency.

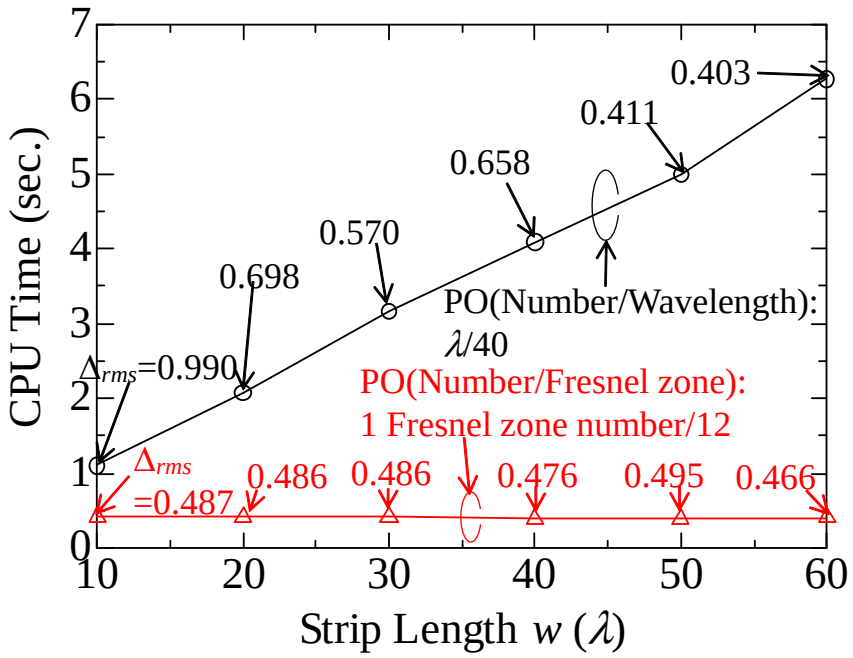

Figure 4.6: CPU time and RMS error against strip length w

Table 1: Sampling density to realize the constant value of Δ_{rms}

m	w [λ]	sampling deinsity (predicted) [/λ]	sampling deinsity (chosen) [/λ]	Δ_{rms} for 4th column
1	10	(initial value) 80.0	80	0.493
2	20	56.6	56	0.498
3	30	46.2	46	0.495
4	40	40.0	40	0.493
5	50	35.8	36	0.490
6	60	32.7	34	0.474

4.5 Extension for 3-D Problems

In this section, we discuss the applicability of the proposed method in the 3-dimensional case which cannot be analytically evaluated as closed forms. Here, integration for local area around the reflection point on an infinite PEC plane and a part of sphere is discussed as the basic study.

In 3-D case, it is difficult to uniquely apply the ASM to the radiation integral because there is ambiguity in determining the segment shape on the scatterer surface while every segment is simply determined by the shape of the periphery of the scatterer in 2-D case.

One possible segmentation method which harmonizes with the Fresnel Zone localization and is applicable for 3-D general surfaces is described in Fig. 4.7. The local integration areas are characterized by two directions; Δn which is the maximum variation direction in Δn and τ which is the non-variation direction in Δn. N_σ and N_τ are the number of sampling points along the σ direction per one Fresnel zone number and τ direction per 1/4 rotation, respectively. The precise definitions of σ and τ are mentioned in the scheme of the modified edge representation (MER) technique [4.9]. Note that the boundary of local area is defined by the condition of $\Delta n_B = 3$ and the shape of it is an ellipse when the scatterer is planar, and that the boundary is along the τ direction.

Reflected fields from the plane were calculated for various distances d by two methods; the first one is the image theory, which gives the exact solution in this case, and the second one is the surface integration based on the localization and proposed segmentation as shown in Fig. 4.8. Reflected field patterns from $\theta = 0^\circ$ to 45° for $d = 1\lambda$ and $d = 100\lambda$ are plotted in Fig. 4.9(a) and Fig. 4.9(b) respectively. Both of the graphs are drawn under the condition of $N_\sigma = 20$ and $N_\tau = 10$. Although there is a little difference between the exact solution and proposed one in the case of $d = 1\lambda$, two pattern are almost matched.

The RMS errors for the reflection pattern from $\theta = 0^\circ$ to 45° under the condition of $N_\sigma = 20$ and $N_\tau = 10$ against the distance d are plotted in Fig. 4.10. Since the division of θ is 0.1°, N_θ equals 451. The sizes of local areas for $\theta = 0^\circ$ to 45° are also depicted and correspond to the right vertical axis. Note that the total number of segments is always constant for any values of d and this fact caused the almost-constant CPU time because N_σ and N_τ are unchanged. While the local integration areas themselves increase in proportion to d but the total number of divisions is unchanged, the RMS error does not get worse.

The proposed method is applicable to a curved scatterer case as well. We calculated a reflected wave from a part of sphere shown in Fig. 4.11(a). The same segmentation as Fig. 4.7 can be straightforwardly applied to the local area on the surface of sphere. The RMS errors of the reflected pattern from $\theta = 0^\circ$ to 45° with 0.1° step and the size of local area are also plotted in Fig. 4.11(b) under the condition of $N_\sigma = 20$ and $N_\tau = 10$. The

similar tendencies as Fig. 4.10 are observed. The discussion of number of division for the remaining parts of scattering centers such as the edge- and corner-diffraction for general 3-D scatterers is left for future works.

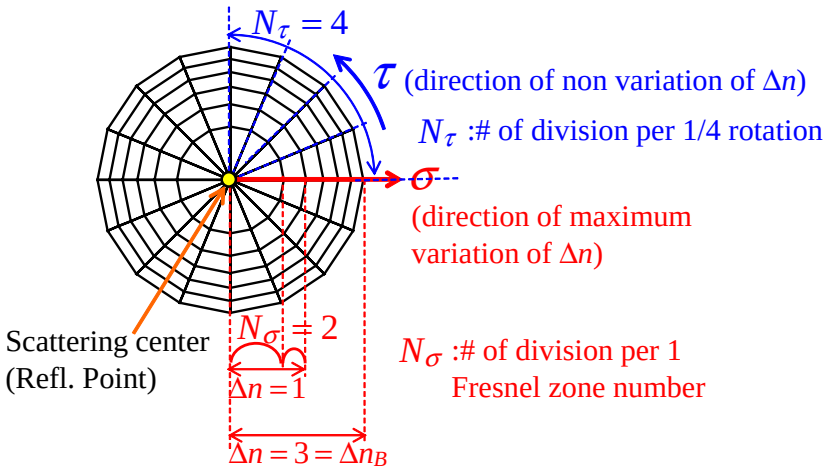

Figure 4.7: Segmentation method for local area around the reflection point on 3-dimensional scatterer surface

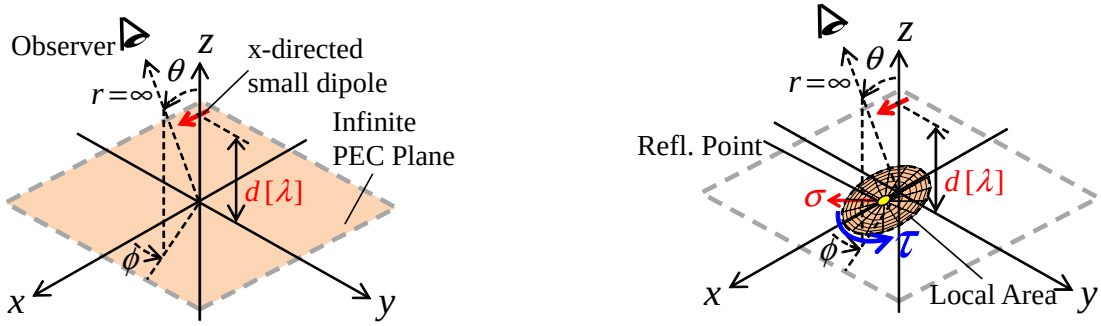

(a) Original Problem (Infinite plane and dipole)

(b) After localization and σ&τ segmentation

Figure 4.8: Calculation model for basic study of 3-D case

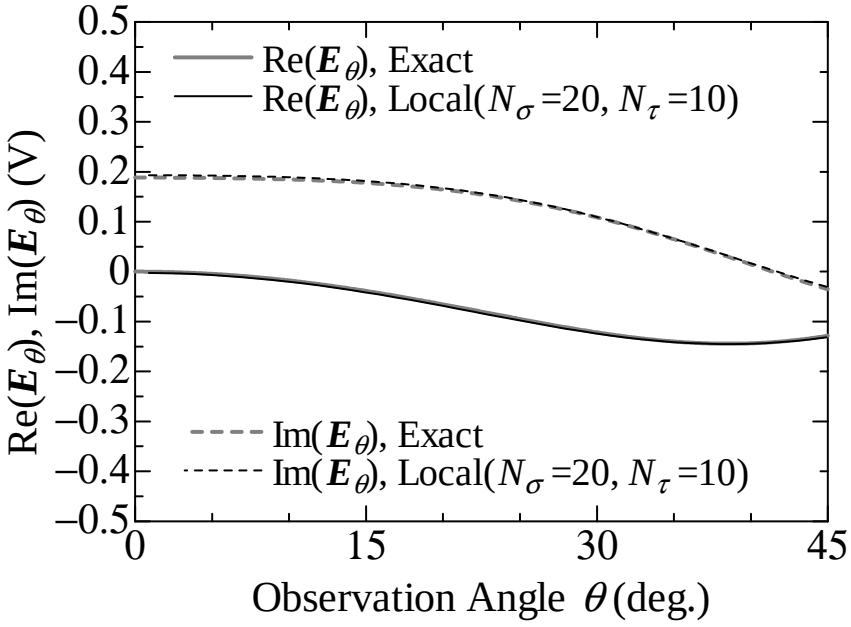

(a) $d = 1\lambda$

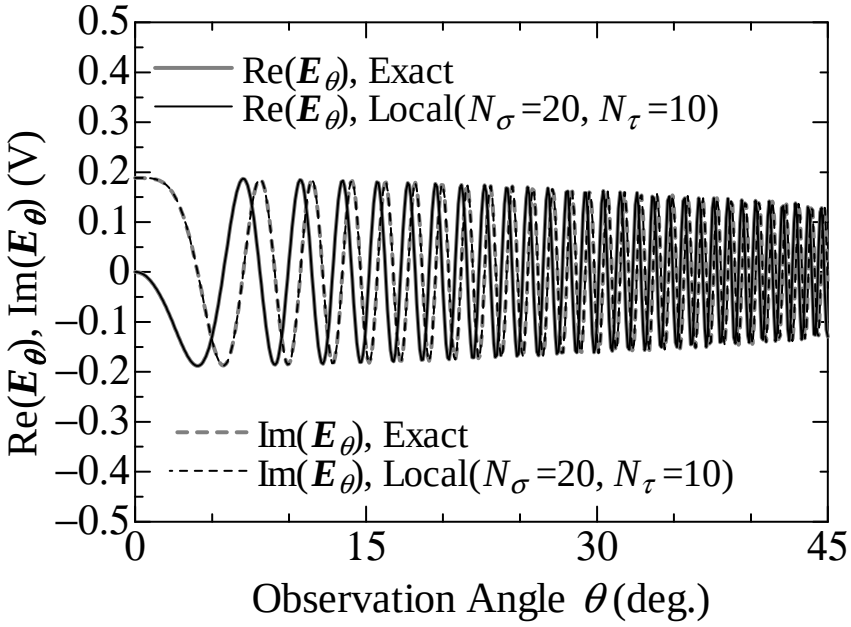

(b) $d = 100\lambda$

Figure 4.9: Reflected fields by the image and the PO segmentation in Fig. 4.8 for Localized area

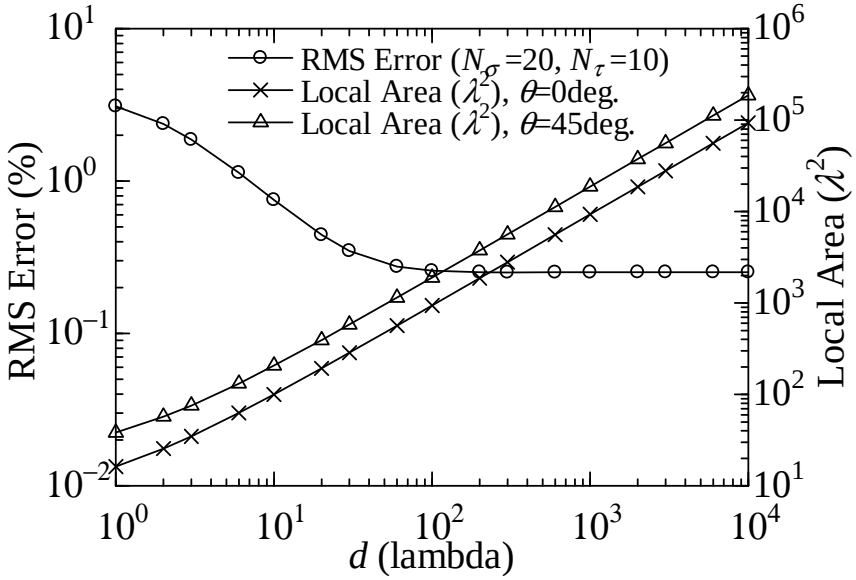

Figure 4.10: RMS error and Local Area against the distance d between dipole and infinite plane

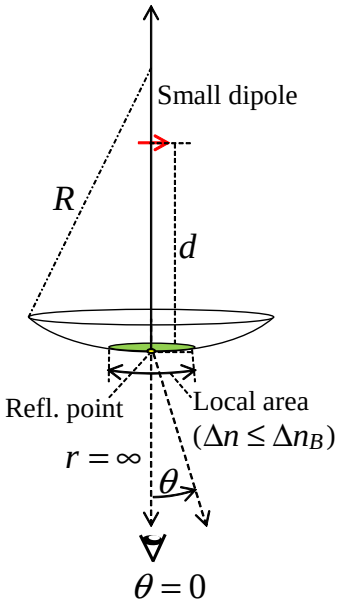

(a) Geometry

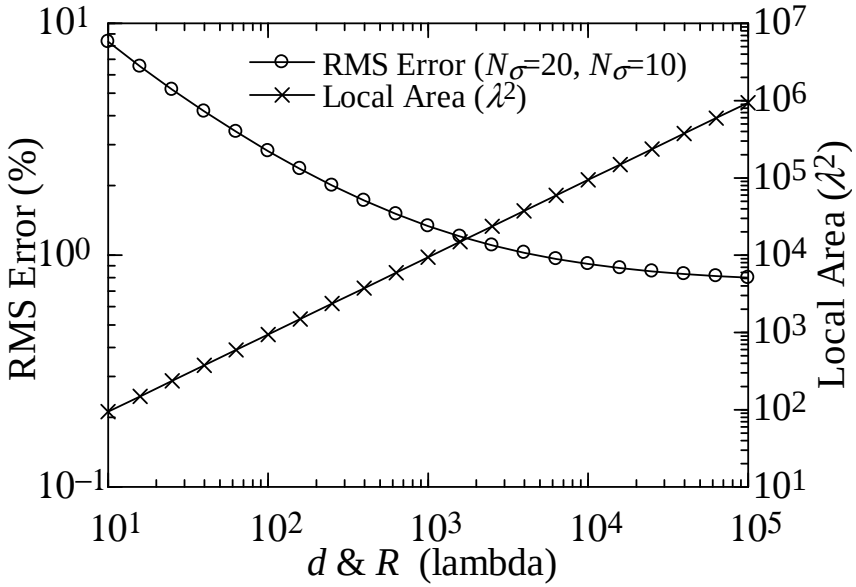

(b) RMS error and Local Area against $d\&R$

Figure 4.11: Curved scatterer case: a small dipole and a part of sphere

4.6 Concluding Remarks

The new technique to introduce the ASM in the localization method was presented. We trim the integration area in such a way that the area contains constant number of the oscillation of the integrand in PO radiation integral and the ASM provides the constant sampling points per one oscillation. We applied the propose method to 2-D RCS calculation for PEC strip and cylinder. We confirmed that our proposed method provides frequency independent number of divisions and realizes a certain constant accuracy for any frequency and observation angles. As the starting point for extension to 3-D case, this method was applied for reflection from an infinite PEC plane and a part of sphere by introducing a possible segmentation in terms of σ and τ direction.

The discussion of number of division for general 3-D scatterers with diffraction and application of proposed integration techniques into another radiation integral such as those in the Method of Moments are left for future works. The hybrid use of this method and the FPO algorithm can further accelerate the PO computation and is also an important future task.

References

[4.1] R. F. Harrington, Time-Harmonic Electromagnetic Fields, pp.127-130, *McGraw-Hill*, New York. 1961

[4.2] P. H. Pathak, "Techniques for high frequency problems," in *Antenna Handbook Theory, Application and Design*, Y. T. Lo and S. W. Lee, Eds. New York: Van Nostrand Reinhold, 1988

[4.3] J. A. Shifflett, "CADDRAD: a physical optics radar/radome analysis code for arbitrary 3D geometries," *IEEE Antennas Propagation Magazine*, vol.39, no.6, pp.73-79, Dec. 1997

[4.4] E. G. Papkelis, I. Psarros, I. C. Ouranos, C. G. Moschovitis, K. T. Karakatselos, E. Vagenas, H. T. Anastassiu and P. V. Frangos, "A radio-coverage prediction model in wireless communication systems based on physical optics and the physical theory of diffraction [Wireless Corner]," *IEEE Antennas and Propagation Magazine*, vol.49, no.2, pp.156-165, April 2007

[4.5] V. A. Borovikov, *Uniform Stationary Phase Method*, IEE Electromagnetic waves series 40, 1994

[4.6] A. Michael, "Equivalent edge currents for arbitrary aspects," *IEEE Transaction on Antennas and Propagation*, Vol.AP-32, No.3, Mar. 1984

[4.7] P. Y. Ufimtsev, "Elementary edge waves and the physical theory of diffraction," *Electromagnetics*, vol.11, iss.2, pp.125160, 1991

[4.8] P. M. Johansen and O. Breinbjerg, "An exact line integral representation of the physical optics scattered field: The case of a perfectly conducting polyhedral structure illuminated by electric Herzian dipoles," *IEEE Transaction on Antennas and Propagation*, vol.AP-43, no.7, pp.689-696, Jul. 1995

[4.9] K. Sakina, M. Ando, "Mathematical derivation of modified edge representation for reduction of surface radiation integral," *IEICE Transaction on Electronics*, vol.E-84-C,no.1,p.74-83, Jan. 2001

[4.10] M. Albani and S. Maci "An Exact Line Integral Representation of the PO Radiation from a Flat Perfectly Conducting Surfaces Illuminated by Elementary Electric or Magnetic Dipoles," *Turk. J. Electr. Eng.*, vol.10, no.2, pp.291-305, 2002

[4.11] M. Albani, "Boundary Diffracted Wave and Incremental Geometrical Optics: A Numerically Efficient and Physically Appealing Line-Integral Representation of Radiation Integrals. Aperture Scalar Case," *IEEE Transaction on Antennas and Propagation*, vol.59, no.2, pp.586-594, Feb. 2011

[4.12] O. M. Conde, J. Perez, M. P. Catedra, "Stationary phase method application for the analysis of radiation of complex 3-D conducting structures," *IEEE Transaction of Antennas and Propagatation*, vol.49, no.5, pp.724-731, May 2001

[4.13] J. B. Keller, "Geometrical theory of diffraction," *Journal of the Optical Society of America*, vol.52, pp116-130, 1962

[4.14] A. Ludwig, "Computation of radiation patterns involving numerical double integration," *IEEE Transaction on Antennas and Propagation*, vol.16, no.6, pp.767-769, Nov. 1968

[4.15] W. B. Gordon, "Far-field approximations to the Kirchoff-Helmholtz representations of scattered fields," *IEEE Transaction on Antennas and Propagation*, vol.23, no.4, pp.590-592, Jul. 1975

[4.16] C. Delgado, J. M. Gomez, M. F. Catedra, "Analytical Field Calculation Involving Current Modes and Quadratic Phase Expressions," *IEEE Transaction on Antennas and Propagation*, vol.55, no.1, pp.233,240, Jan. 2007

[4.17] F. Vico-Bondia, M. Ferrando-Bataller, A. Valero-Nogueira, "A New Fast Physical Optics for Smooth Surfaces by Means of a Numerical Theory of Diffraction," *IEEE Transaction on Antennas and Propagation*, vol.58, no.3, pp.773-789, Mar. 2010

[4.18] A. Boag, "A fast physical optics (FPO) algorithm for high frequency scattering," *IEEE Transaction on Antennas and Propagation*, vol.52, no.1, pp. 197- 204, Jan. 2004.

[4.19] A. Boag, C. Letrou, "Multilevel fast physical optics algorithm for radiation from non-planar apertures," *IEEE Transaction on Antennas and Propagation*, vol.53, no.6, pp. 2064- 2072, June 2005

[4.20] R. J. Burkholder, Teh-Hong Lee, "Adaptive sampling for fast physical optics numerical integration," *IEEE Transaction on Antennas and Propagation*, vol.53, no.5, pp. 1843- 1845, May 2005.

[4.21] K. Ito, T. Shijo, M. Ando, "Fresnel zone criterion to implement locality in the method of moments and PO-MoM hybrid method for the reduction of unknowns," *IEICE Transaction on Electronics*, vol.E94-C, no.1, pp72-79, Jan. 2011

[4.22] T. Kohama, M. Ando, "Localization of radiation integrals using the Fresnel zone numbers,"*IEICE Transaction on Electronics*, vol.E95-C, no.5, pp928-935, May 2012

[4.23] T. Shijo, T. Itoh, M. Ando, "Visualization of high frequency diffraction based on physical optics," *IEICE Transaction on Electronics* vol.E87-C, no.9, pp.1607-1614, Sep. 2004

Chapter 5

Implementation of High Frequency Locality in the Method of Moments for 3-Dimensional Scattering Problems

5.1 Introductory Remarks

Redaction of the computational complexity and memory consumption in the method of moments (MoM) [5.1] computation has been an important problem in electromagnetic scattering analyses for several decades. If the direct method is adopted as matrix inversion, computational complexities for the matrix filling and matrix inversion are roughly proportional to N^2 and N^3, respectively, where N is the number of unknowns. The type of unknowns to be solved depends on the type of analyzed materials and adapted integral equations (e.g. electric field integral equation (EFIE), magnetic field integral equation (MFIE) or combined field integral equation (CFIE)). A required capacity of computer memory is proportional to N^2 as well. Since N becomes larger in proportion to the electrical size of scatterer which is proportional to f^2 (f is frequency) when the physical size of scatter is unchanged, frequency dependency of memory capacity amount to $O(f^4)$. This means that the MoM analysis becomes explosively inefficient in higher frequency. Some of the techniques to suppress the computational cost of the MoM have been proposed. The fast multipole method (FMM) [5.2] and multilevel fast multipole method (MLFMM) [5.3] are the representative methods among them. The two methods suppress the memory consumption to $O(N^{1.5})$ and $O(N \log N)$, respectively. The characteristic basis function method (CBFM) [5.4] is also well-known technique to reduce the memory consumption. Note that these methods don't directly reduce N itself but reduce N's dependence of the complexity in the MoM computation. Therefore the frequency dependence of N is also unchanged as $O(f^2)$.

PO-MoM is another way to reduce N directly [5.5, 6]. A scatterer is divided into a physical optics (PO) [5.7, 8] region and an MoM region and then unknowns are assumed only on the MoM region. Although PO-MoM has been treated even in the recent papers such as [5.9], to the best knowledge of the authors, there is no explicit criterion to determine the boundary between PO and MoM regions.

In this chapter, we focus on the Local-MoM [5.10] which was originally proposed for

2-dimensional problems and directly reduces the frequency dependence of N. The Local-MoM is one of the MoM fully considering the "locality of scattering phenomena." The locality itself is a key feature in the high frequency asymptotic (HFA) methods such as localized evaluation of PO integrals [5.11], the geometrical theory of diffraction (GTD) [5.12] and the uniform theory of diffraction (UTD) [5.13]. As mentioned in the chapter 2, scattering phenomena by PO currents also show the locality. Even if a dipole source illuminates the whole surface of scatterer, the strong contributions appear in only the area around the scattering centers (reflection and edge diffraction points in terms of ray optics) and the contribution from the other area is almost zero [5.14]. Some of the methods which embed the locality into the MoM have been introduced [5.10, 14–16] and Local-MoM is one of them. The basic idea of Local-MoM is as follows; the induced currents only on the truncated local scatterers are at first analyzed by MoM and then the scattered field is obtained by radiation integral with smooth windowing function to suppress the error due to the truncation of scatterer. In [5.10], the Local-MoM was firstly applied to radar cross section (RCS) analyses of 2-dimensional scatterers. In [5.16], the localization of radiation integral was discussed as the beginning of expansion of Local-MoM into 3-dimensional problem. Throughout these papers, the authors succeeded in giving the explicit criterion to determine truncated local areas in terms of Fresnel zone numbers, unlike PO-MoM. Moreover it was confirmed that a computational accuracy does not degrade so much and the frequency dependence of N is suppressed than that for the normal MoM.

The objective of this chapter is to expand the Local-MoM into 3-D problem together with some modifications including the technique proposed in [5.16]. Scatterings from some simple structures such as a perfect electric conductor (PEC) rectangular plate and a part of sphere illuminated by an infinitesimal dipole will be treated as the beginning of the application of Local-MoM to 3-D problems. Since the special procedures in the Local-MoM computation are only the truncation of analysis model and the applying of the windowing function based on Fresnel zone criterion, they could be easily implemented in existing MoM-based commercial simulators. This is the big difference from hybrid methods between HFA methods and MoM (e.g. PO-MoM, MoM-GTD [5.17] or MoM-UTD [5.18]). These hybrid methods need to take fields calculated by HFA methods into account. Therefore an implementation of hybrid methods by existing simulators having a MoM solution only is impossible without developing a new option to give an HFA solution. Here the Local-MoM is implemented in a commercial electromagnetic simulator WIPL-D. We will discuss how to apply the windowing function since we found that the windowing proposed in the chapter 2 provided inaccurate results. The computational accuracy and the frequency dependence of computational load will also be discussed.

As already explained, the big difference between the Local-MoM and the fast methods

of FMM, MLFMM and CBFM is the frequency dependence of N. These fast methods don't change it as $O(f^2)$ while the Local-MoM technique directly reduces it from $O(f^2)$ to $O(f)$ due to the truncation of scatterer. Moreover there is a possibility which the computation complexity can be further reduced by jointly using the Local-MoM and these fast methods. That is, we may apply the fast methods to small scatterers truncated by following the Local-MoM procedure. From this point of view, the Local-MoM is totally independent of these fast methods. In this paper we however don't use them in order to simply evaluate the effectivity of Local-MoM.

5.2 Analysis Method

5.2.1 MoM for Localized Scatterer

Fig. 5.1 compares the calculation procedures of normal MoM and Local-MoM. In the normal MoM, an integral equation is at first constructed for unknown currents $\boldsymbol{J} = \sum_n I_n \boldsymbol{B}_n$ assumed over the whole surface of a PEC scatterer as the following matrix and inner product form.

$$[Z_{mn}]\,[I_n] = [V_m] \tag{5.1}$$

$$Z_{mn} = \langle \boldsymbol{T}_m, L\,(\boldsymbol{B}_n) \rangle \tag{5.2}$$

$$V_m = \left\langle \boldsymbol{T}_m, \left[\left\{ EYE\left(\frac{\Delta n}{\Delta n_B} \right) \right\}^{\alpha} \cdot \boldsymbol{I}^i \right] \right\rangle \tag{5.3}$$

$$EYE\left(\frac{\Delta n}{\Delta n_B} \right) = \begin{cases} \cos^2\left(\dfrac{\Delta n}{\Delta n_B} \dfrac{\pi}{2} \right) & \Delta n \le \Delta n_B \\ 0 & \Delta n > \Delta n_B \end{cases} \tag{5.4}$$

$\boldsymbol{B}_n$ and $\boldsymbol{T}_m$ are basis and testing functions, respectively. In is the coefficient for basis functions, $\boldsymbol{I}^i$ is an incident field from external sources and $L(\cdot)$ is a linear operator. The type of $\boldsymbol{I}^i$ (electric or magnetic field) and formulation of $L(\cdot)$ are specified by analysis conditions including the type of integral equation. For more details, please refer to the chapter 5 of [5.1]. (5.4) with $x = 1$ is a raised cosine function which takes the value 1 at (R) and smoothly decreases towards the boundary of the local area (B) and takes the value 0 at (B). This function was previously utilized to suppress some errors due to localization in [5.16]. For the later discussion for the Local-MoM, the EYE function to the power of the parameter α is multiplied with $\boldsymbol{I}^i$ in (5.3), although it is not used in the normal MoM, that is, $\alpha = 0$ is normally applied. Note that when the exponent value α is zero, the

windowing value is defined as follows;

$$\left\{ EYE\left(\frac{\Delta n}{\Delta n_B}\right)\right\}^0 = \begin{cases} 1 & \Delta n \leq \Delta n_B \\ 0 & \Delta n > \Delta n_B. \end{cases} \tag{5.5}$$

After the construction of the matrix (5.2), it is solved by matrix inversion. When a source is fixed (e.g. bistatic RCS or antenna radiation analysis), this matrix operation step is conducted only once.

After that, a radiation integral for the observed currents is conducted. For the same reason as the expression of (5.3), the form of radiation integral including the EYE function is expressed as (5.6) Here k is a wave number, r is a distance between an integration point and an observer and β is the exponent for the EYE function. In the normal MoM, the windowing is not needed, that is, we use $\beta = 0$ as defined in (5.5).

$$\boldsymbol{E}_S \propto \int_S \left\{ EYE\left(\frac{\Delta n}{\Delta n_B}\right)\right\}^\beta \boldsymbol{J}\frac{\exp\left(-jkr\right)}{4\pi r}dS \tag{5.6}$$

The radiation integral must be done repeatedly for the number of observation angles. As we mentioned in 5.1, computational times for matrix filling and matrix inversion and a required capacity of computer memory are proportional to N^2, N^3 and N^2, respectively.

In Local-MoM, we at first give an i-th observation angle (θ_i, ϕ_i) and then localize and truncate the analysis model so that only the local areas which satisfies the Fresnel zone number criterion survive and the other areas are removed. Unknown currents are placed only on truncated local areas and a matrix is constructed only for these local currents. After solving the matrix, radiation integral for these local currents is conducted to obtain the scattered field at the i-th angle (θ_i, ϕ_i). In the construction of matrix (integral equation) and radiation integral, the windowing is applied to the incident field radiated from the source and the integrand, respectively. In Local-MoM computation, we apply the EYE function with some values of α and β. A good combination of α and β for scattering analysis will be discussed later.

Furthermore, if the analysis model are separated into N_i^{sca} isolated scatterers at the i-th angle due to the localization as shown in Fig. 4 and electromagnetic couplings between two separated scatterers is negligible (e. g. planar scatterer case), it is enough to construct the matrix only for currents on a j-th separated scatterer. The currents and the scattered field for the j-th scatterer are obtained in the same way as explained above. The scattered field for the i-th angle, $\boldsymbol{E}_S(\theta_i, \phi_i)$, is calculated by

$$\boldsymbol{E}_S\left(\theta_i, \phi_i\right) = \sum_{j=1}^{N_i^{sca}} \boldsymbol{E}_S^{\#j}\left(\theta_i, \phi_i\right) \tag{5.7}$$

where $\boldsymbol{E}_S^{\#j}(\theta_i, \phi_i)$ is the scattered field from the j-th separated scatterer at the i-th angle. This technique can further reduce the computational cost of Local-MoM because the number of unknown currents to be solved in one-time MoM execution (procedure of the MoM analysis) becomes smaller.

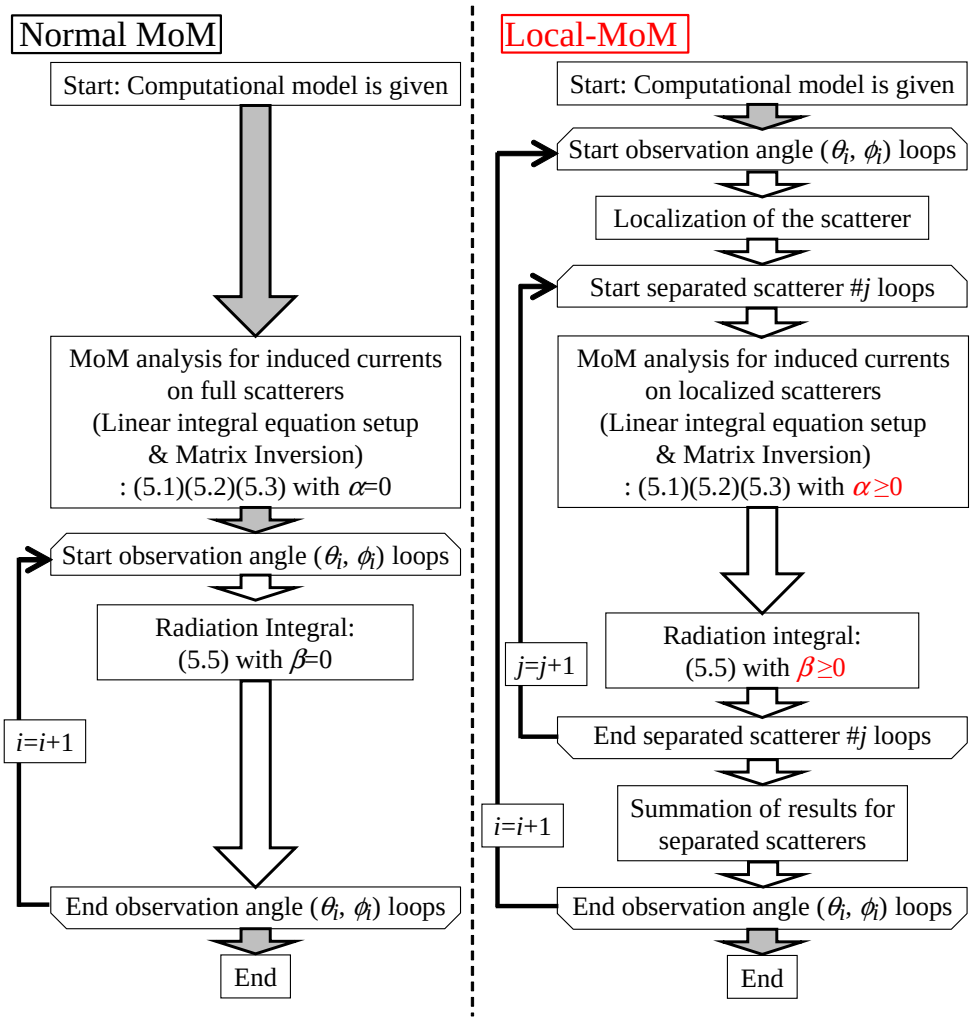

Figure 5.1: Comparison of Calculation Procedures in Normal MoM and Local-MoM.

5.2.2 Rough Discussion on Computational Cost

Let n_{ij} be the number of unknown currents on the j-th separated scatterer for the i-th angle (θ_i, ϕ_i). Since n_{ij} for any i and j is much smaller than N of the normal MoM, the required capacity of memory can be surely saved by the Local-MoM technique. On the other hand, since the integral linear equation (matrix) must be solved repeatedly for

the number of observation angle unlike the normal MoM, the computation time becomes longer than that for the normal MoM for some situations, especially lower frequency cases. The frequency dependence of n_{ij} is however $O(f)$-level as the electrical size of a truncated scatterer. The localization therefore becomes more effective in higher frequency and the difference of frequency dependence between n_{ij} and N provides the saving of computational times as well as the memory capacity. Numerical discussion on these computational costs will be done in 5.3.3.

5.3 Numerical Results

5.3.1 Discussion on Windowing

In the discussion on 2-D structure [5.10] and the localization technique about physical optics radiation integral [5.16], the windowing was applied only to the integrand in radiation integral, that is, $\alpha = 0$ and $\beta = 0$ are applied to (5.3) and (5.6), respectively. We however found that the windowing only to the integrand gave us results with a poor accuracy. To overcome this, we searched for the better windowing method to reproduce the scattering field from the original rectangular plate with smaller errors. We examined several combinations of the exponent α and β of the EYE function. The former one of $\{EYE(\Delta n/\Delta n_B)\}^{\alpha}$ corresponds to the extra boundary condition which the incident field becomes weaker near the periphery of local areas in addition to the original boundary condition required in an adapted integral equation (e.g. EFIE, MFIE or CFIE). From another point of view, $\{EYE(\Delta n/\Delta n_B)\}^{\alpha}$ can be interpreted to embed the locality in the current distribution analysis. The latter one of $\{EYE(\Delta n/\Delta n_B)\}^{\beta}$ is just for eliminating a discontinuity of currents near the periphery. The discontinuity would produce diffracted fields which don't exist in original problem. Windowing both of them is more natural idea than that in previous papers, because both of the modification of current distribution analysis and the elimination of undesired diffraction match the feature of locality well. Since the paper of [5.16] showed that the EYE function to the first power gives us very accurate results, we especially focused on the cases of $\alpha + \beta = 1$ although we examined other cases (e.g. $\alpha + \beta = 2$).

The second row of Table 1 compares the root mean square error values of Δ_{rms} for the scattered field from the rectangular plate in Fig. 5.2 under the condition of $a = b = 8d =$

16λ. The error Δ_{rms} is defined by (5.8) [5.19];

$$\Delta_{rms} = \left\{ \frac{\sum_{i=1}^{N_{obs}} \left| \boldsymbol{E}_S^{\text{int}}(\theta_i) - \boldsymbol{E}_S^{\text{ref}}(\theta_i) \right|^2}{\sum_{i=1}^{N_{obs}} \left| \boldsymbol{E}_S^{\text{ref}}(\theta_i) \right|^2} \right\}^{\frac{1}{2}} \times 100\ [\%]. \tag{5.8}$$

where $\boldsymbol{E}_S^{\text{ref}}(\theta_i, \phi_i)$ is the reference scattered field calculated by the normal MoM, $\boldsymbol{E}_S^{\text{int}}(\theta_i, \phi_i)$ is the one calculated by the Local-MoM and N_{obs} is the number of observation angle. Here N_{obs} is 361 at $\phi = 0°$ plane. In the cases of $\alpha+\beta = 0$ and $\alpha+\beta = 0$, the errors are relatively large. These errors decrease as a frequency becomes higher. The third row of Table 1 shows some of the results for the case when frequency is 6-times higher ($a = b = 8d = 96\lambda$). In both cases, the condition of $\alpha = \beta = 0.5$ tends to provide reasonable results. Although this conclusion might slightly change depending upon the specific profile of problem, we therefore adopt $\alpha = \beta = 0.5$ hereafter.

Table 1: Comparison of root mean square errors Δ_{rms} for various combination of α and β

α, β	0, 0	0, 1	0.25, 0.75	0.5, 0.5	0.75, 0.25	1, 0	0, 2	1, 1	2, 0
Δ_{rms} for $a = b = 8d = 16\lambda$ (%)	80.9	20.3	7.63	5.04	5.07	6.49	29.1	20.3	21.2
Δ_{rms} for $a = b = 8d = 96\lambda$ (%)		4.53		1.17		1.50			

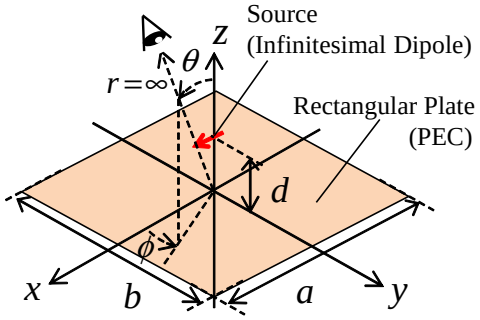

Figure 5.2: Analysis model (a Rectangular Plate and a Dipole).

5.3.2 Total Field Pattern

Fig. 5.3(a) compares the total field patterns calculated by the normal MoM and Local-MoM under the condition of $a = b = 8d = 16\lambda$. Some errors exist around the refection and

incident shadow boundary (RSB and ISB) but reasonable accuracy of $\Delta_{rms} \approx 5.04\%$ was obtained. The shapes of localized model for the angle $\theta = 0°$, $30°$ and $90°$ are shown in Fig. 5.3(b) to Fig. 5.3(d). The local areas for diffraction points are connected at $\theta = 0°$ and $30°$ since the scatterer is not large enough (in other words, frequency is not high enough) from the Local-MoM's point of view. In that sense, the effectivity of Local-MoM is not high for this model. The reasonable accuracy was achieved not only in $\phi = 0°$ plane but also but also in $\phi = 45°$ plane as shown in Fig. 5.4. Δ_{rms} for $\phi = 45°$ plane is about 4.10%. Fig. 5.5(a) shows the results with 6-times higher frequency($a = b = 8d = 96\lambda$). The localized scatterers for this frequency are also visualized in Fig. 5.5(b) to Fig. 5.5(d). The agreement between two patterns is obviously improved, and the error Δ_{rms} is reduced to 1.17%. This is because the Local-MoM is based on the HPA methods and therefore it has the similar tendency with the HPA which accuracy will be improved in higher frequency. However accuracy of Local-MoM is unfortunately poorer than the PO's results since the geometry of the model is too simple.

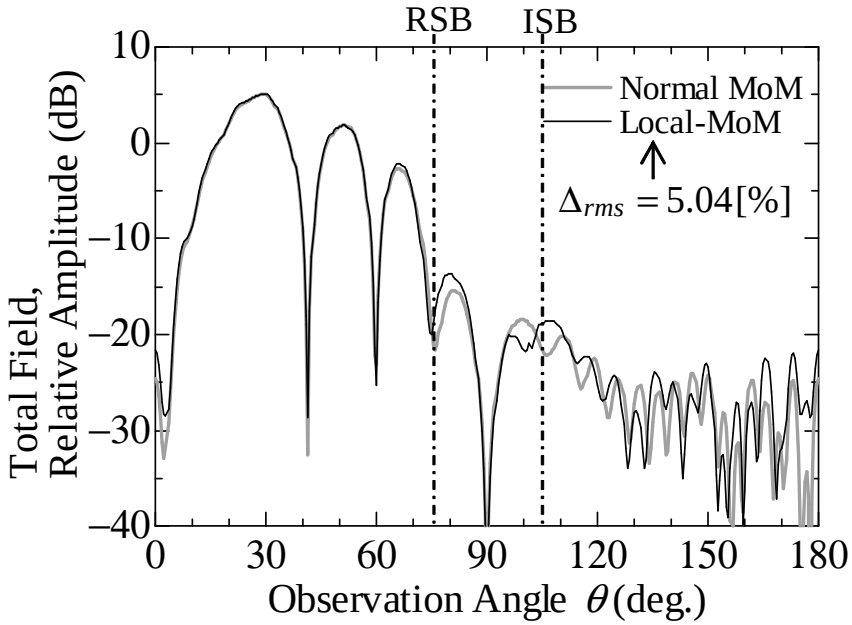

(a) Total field pattern

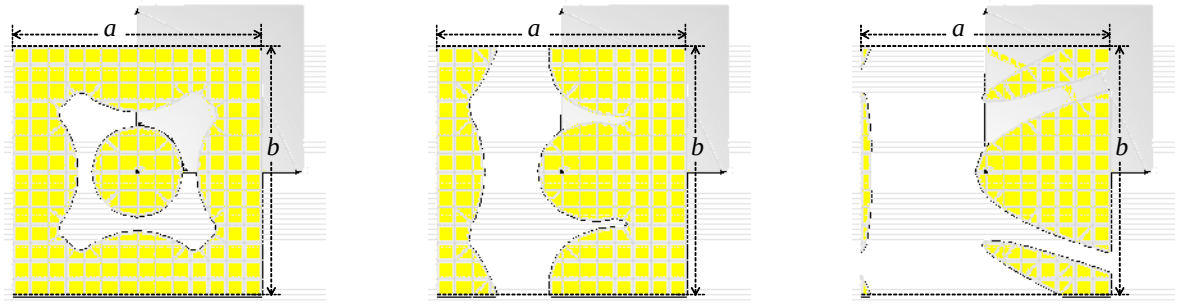

(b) $\theta = 0°$ (c) $\theta = 30°$ (d) $\theta = 90°$

Figure 5.3: Local-MoM's result ($a = b = 8d = 16\lambda$, $\phi = 0°$ plane) (a) Total Field Pattern (b) (c) (d) Localized model for various angles.

Another example which is difficult to be treated by HFA methods is demonstrated. A part of sphere with the radius $R_{sph} = 30\lambda$ is partly lit by a dipole source and the shadow boundary is formed on the scatterer as shown in Fig. 5.6. In ray optics, several kinds of diffraction waves should be taken into account depending on the observer position: the surface diffracted ray, whispering gallery modes, the incident creeping wave and edge diffracted ray and so on [5.20, 21]. PO cannot take into account the effect of unlit region because the PO's induced currents are not assumed. On the other hand, the local areas may be defined not only on the lit region but also on the unlit region by following the

rules mentioned in the chapter 3.2 if the diffraction points are assumed to be located on the shadow boundary (see Fig. 5.6(a)). Fig. 5.6(b) shows the total field pattern. The error of the Local-MoM is smaller than that of PO because the Local-MoM treats the induced currents on the unlit region. It means that the Local-MoM technique is valid even for the problem where HFA methods cannot work.

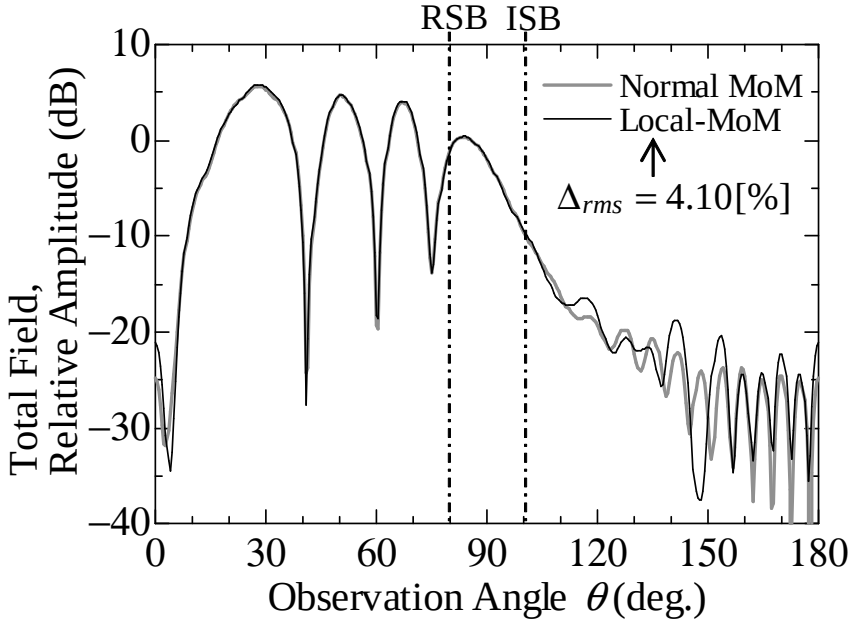

Figure 5.4: Total field pattern for $a = b = 8d = 16\lambda$ and $\phi = 45°$ plane.

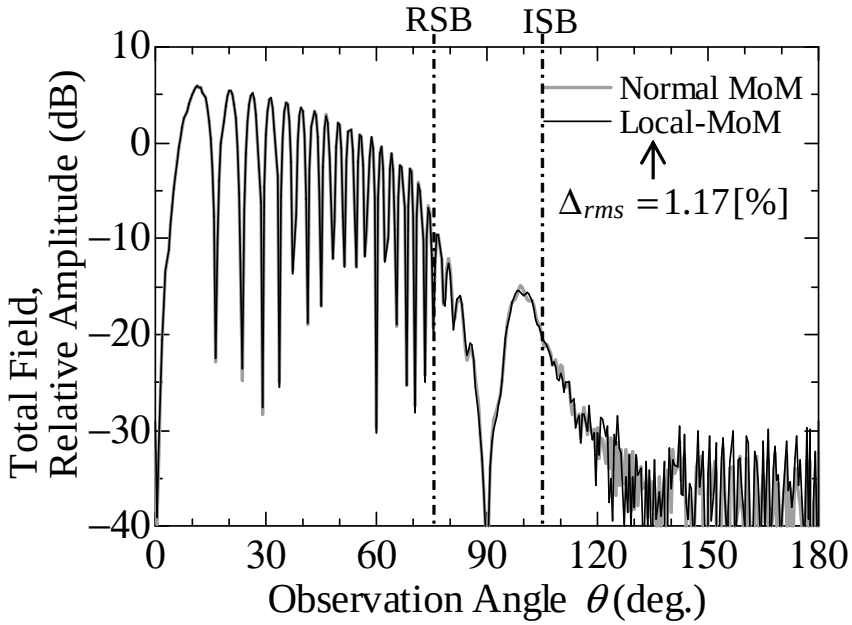

(a) Total field pattern

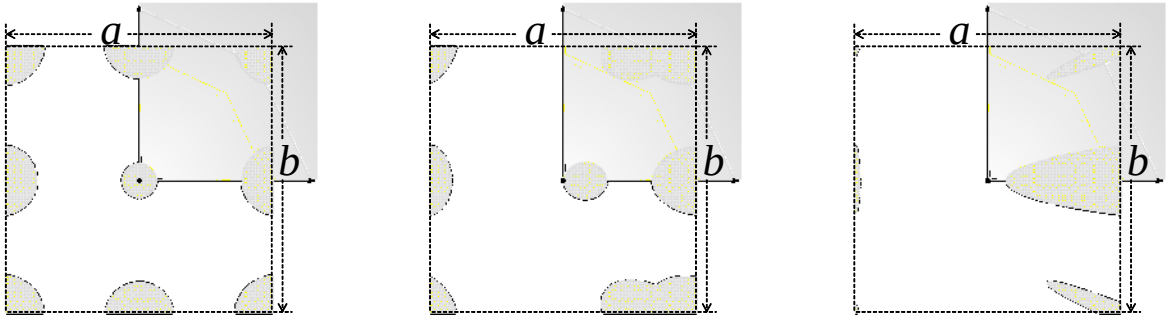

(b) $\theta = 0°$ (c) $\theta = 30°$ (d) $\theta = 90°$

Figure 5.5: Local-MoM's result ($a = b = 8d = 96\lambda$, $\phi = 0°$ plane) (a) Total Field Pattern (b) (c) (d) Localized model for various angles.

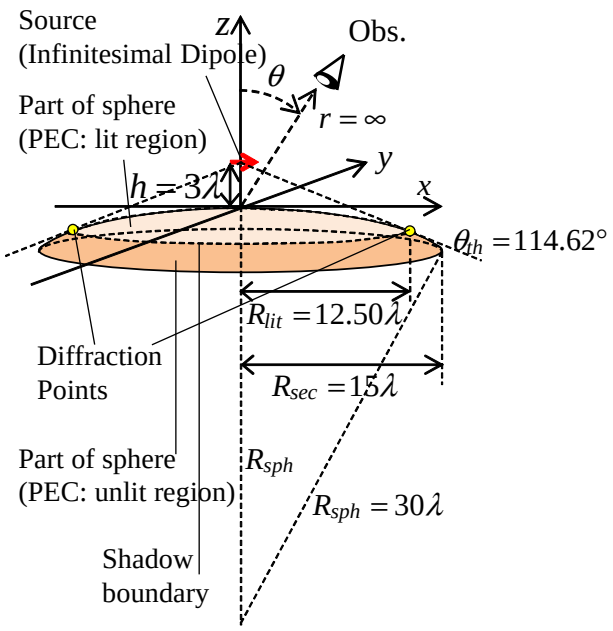

(a) Computational model (a part of PEC sphere partly illuminated by dipole).

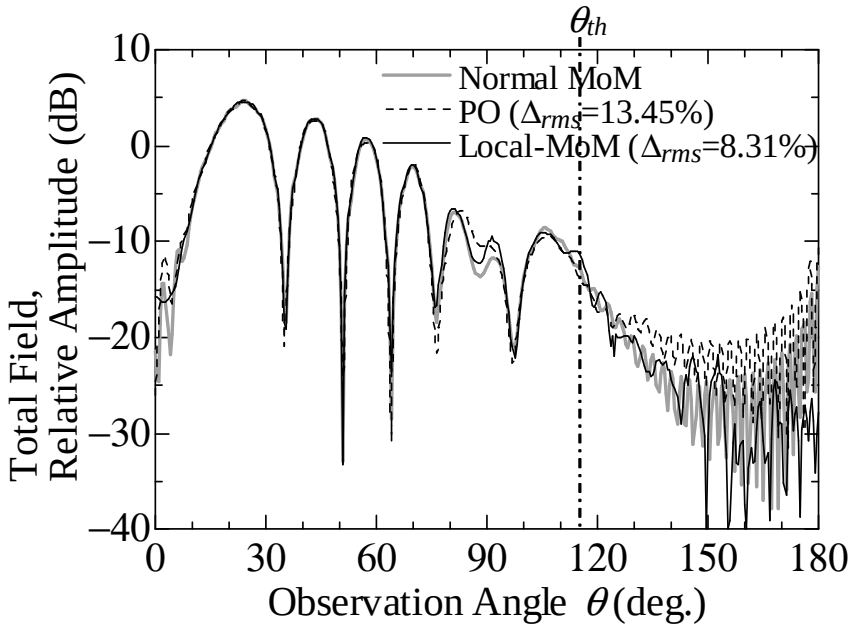

(b) Total field pattern.

Figure 5.6: Local-MoM for a part of sphere with a unlit region.

5.3.3 Discussion on Computational Cost

Fig. 5.7 shows the change of n_{ij} against the observation angle. The number of local areas N_i^{sca} is not constant because the local areas connect or separate each other as seen in comparison between Fig. 5.3(b) and Fig. 5.3(c) and the presence of scattering centers switches depending on the angle. The minimum N_i^{sca} for $a = b = 8d = 16\lambda$ case is 1 while that for $a = b = 8d = 96\lambda$ is 6.

Fig. 5.8 compares M of the memory capacity required for radiation pattern analyses with single precision at $\phi = 0°$ plane or $\phi = 45°$ plane by two methods. M was simply estimated by the equation of $M = 8N^2$ byte. As for the Local-MoM, N is replaced with $n_{\max}$ defined by

$$n_{\max} = \max_{i,j} n_{ij}. \tag{5.9}$$

As we estimated in 5.2.3, M for the normal MoM is increasing according to $O(f^4)$. It doesn't change for any ϕ plane because currents on the whole surface are necessary to calculate a scattered filed for any observation angles. In the Local-MoM, M varies depending on ϕ value. M for $\phi = 0°$ plane is the almost minimum while M for $\phi = 45°$ plane is the almost maximum. In either cases, the frequency dependence of M for the Local-MoM is more than $O(f^2)$ against our estimation in 5.2.3. This is because the estimation is done for the case when an observation angle is fixed while the angle to give $n_{\max}$ varies according to f (compare Fig. 5.7(a) and Fig. 5.7(b)). Nevertheless, M for Local-MoM is much smaller than that for the normal MoM. In higher frequency, the difference between two lines increases furthermore due to the difference of frequency dependence between $n_{\max}$ and N. Local-MoM technique expands the upper limitation of model size which is solvable by a certain given memory capacity. For example, the Local-MoM is available up to $a = b = 8d = 112\lambda$ by a computer with 32GB memory while the normal MoM is limited below approximately 40λ.

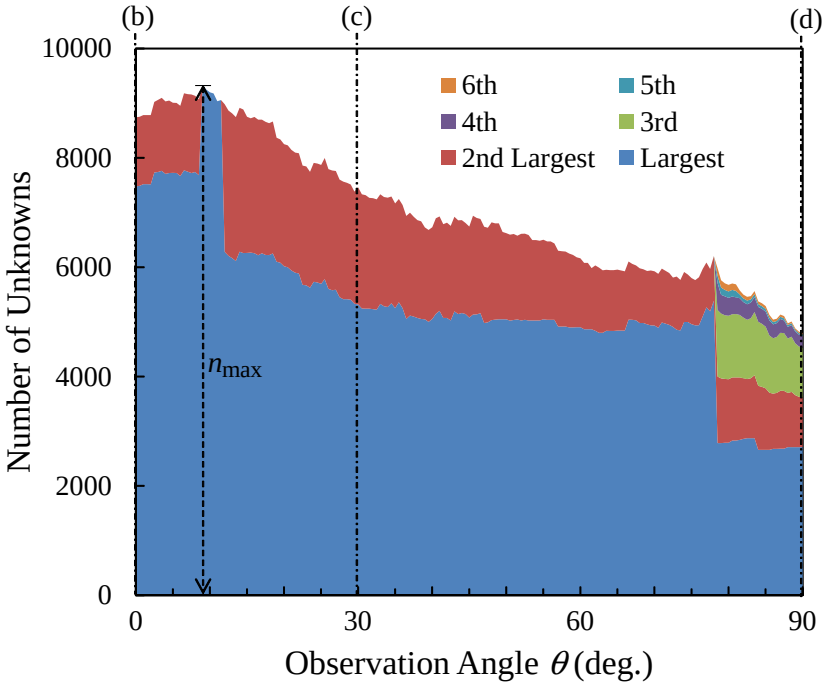

(a) $a = b = 8d = 16\lambda$.

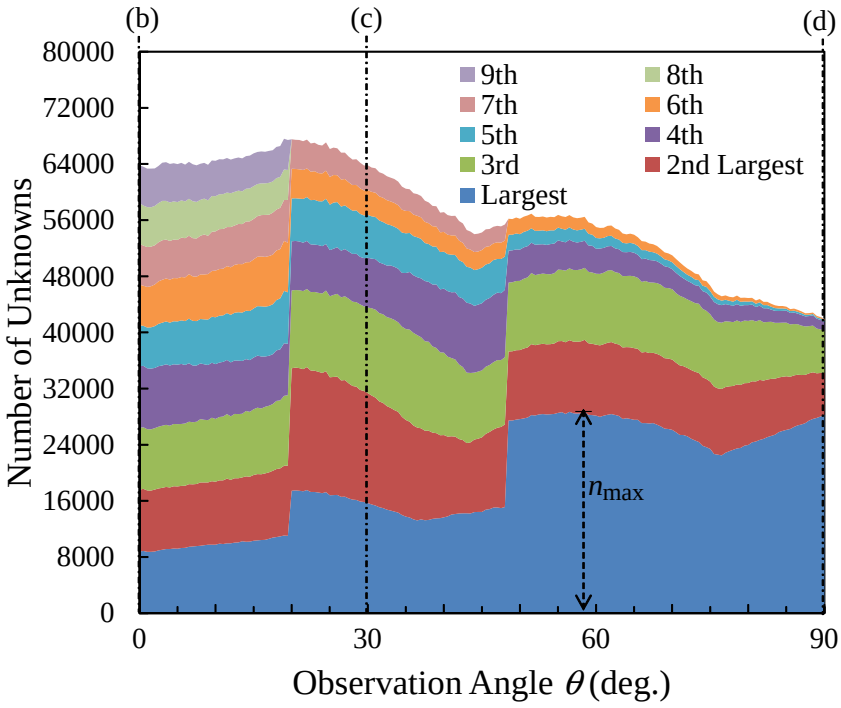

(b) $a = b = 8d = 96\lambda$.

Figure 5.7: Number of Unknowns of Local Areas in $\phi = 0°$ plane. ((b)-(d) in the graph correspond to the angles at which the Localized models are drawn in Fig. 5.3 and Fig. 5.5.

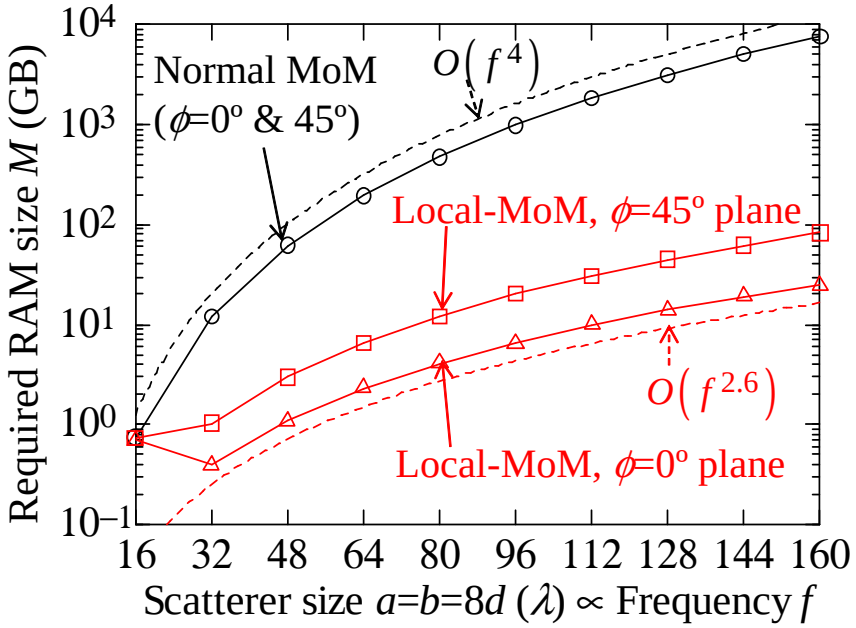

Figure 5.8: Frequency Dependence of memory capacity required for pattern calculation in $\phi = 0°$ or $\phi = 45°$ plane.

Let us here discuss the effectiveness of the Local-MoM in terms of the computational time. The total computational time in the procedure of Fig. 5.1 is mainly dominated by the MoM analysis step. As mentioned in 5.1, the normal MoM's computational times for the matrix filling and matrix inversion are expressed as AN^2 and BN^3, respectively, where A and B are the coefficients which depend on the specification of computer, numerical algorithms adopted in simulator (e.g. the type of numerical integration), and so on. On the other hand, in the Local-MoM computation, the MoM analysis step must repeated for $N_i^{sca} \times N^{obs}$ times. So the times of Local-MoM for each part are expressed as

$$T_A \approx A \sum_{i=1}^{N^{obs}} \sum_{j=1}^{N_i^{sca}} {n_{ij}}^2 \tag{5.10}$$

$$T_B \approx B \sum_{i=1}^{N^{obs}} \sum_{j=1}^{N_i^{sca}} {n_{ij}}^3 \tag{5.11}$$

Here we define and discuss the efficiencies about the matrix filling step e_1 and matrix inversion step e_2, which are the Local-MoM's time normalized by the normal MoM's one

as shown in .

$$e_1 = \frac{\sum_{i=1}^{N^{obs}} \left(\sum_{j=1}^{N_i^{sca}} {n_{ij}}^2 \right)}{N^2} \tag{5.12}$$

$$e_2 = \frac{\sum_{i=1}^{N^{obs}} \left(\sum_{j=1}^{N_i^{sca}} {n_{ij}}^3 \right)}{N^3} \tag{5.13}$$

Note that e_1 and e_2 include neither A nor B, that is, the discussion of e_1 and e_2 is independent of computer's specification, and so on. When e_1 or e_2 becomes smaller than 1, it means the Local-MoM becomes more effective than the normal MoM as for the corresponding step.

The lines with unfilled circles and triangles in Fig. 5.9 show the e_1 and e_2 against the frequency under the condition of $\theta = 0^\circ$ to 180° with 0.5° step, $N^{obs} = 361$ in $\phi = 0^\circ$ plane. In higher frequency, the both of efficiencies are improved so the Local-MoM becomes much more useful as e_2 lowers 1 after $a = b = 8d = 48\lambda$, although e_1 does not lower than 1 until $a = b = 8d = 160\lambda$. Note that the situation of $e_1 > 1$ and $e_2 < 1$ doesn't mean the Local-MoM is inefficient. As the frequency becomes higher and N becomes very large (e.g. $N \approx 100,000$), the time of matrix inversion step is more dominant than that of matrix filling step. For instance, N for $a = b = 8d = 64\lambda$ is approximately 156,000. In that case, a reduction effect in time for matrix inversion would exceed an inefficiency of e_1. As a result, the total computational time in the Local-MoM would lower than that in the normal MoM. Also note that the value of e_1 and e_2 are susceptible to the range of observation angle and N^{obs}. For instance, if only N^{obs} is halved for the fixed ϕ plane, e_1 and e_2 simply become halved as shown by the lines with solid-filled circles or triangles in Fig. 5.9. If ϕ is changed or pattern analysis is conducted for several ϕ planes, the e1 and e2 lines will increase as well. Even for these cases, the improvement of the efficiencies for higher frequency can be expected.

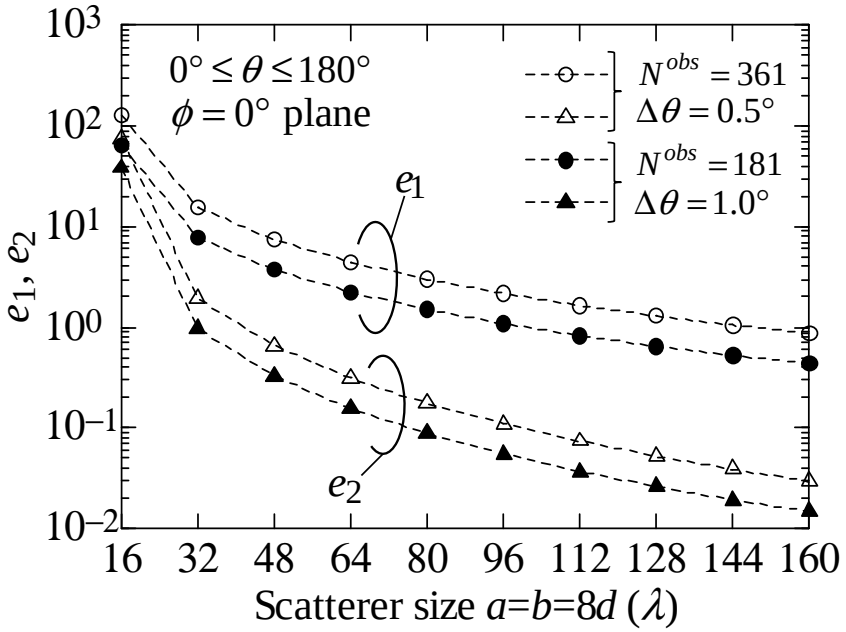

Figure 5.9: Frequency dependence of the efficiencies e_1 and e_2.

5.4 Concluding Remarks

The Local-MoM which embeds the locality of scattering phenomena into the MoM was extended for 3-dimensional problems and was implemented in the commercial electromagnetic simulator WIPL-D. The windowing method was investigated to achieve reasonably-accurate results. Numerical results were demonstrated for the scattering from a rectangular plate and a part of sphere illuminated by an infinitesimal dipole. It was confirmed that the Local-MoM can treat the currents not only on the lit region but also on the unlit (shadow) region. The required capacity of computer memory is surely saved owing to localization of scatterer even in lower frequency cases. The usefulness of the Local-MoM in terms of the total computational time varies depending on situations. Further extensions of Local-MoM, for example, investigation for more complicated-shaped scatterer and joint use of the Local-MoM and fast methods such as FMM or CBFM should be examined as future works. The combination of FMM and Local-MoM is in particular attractive because both of the frequency dependence of N will be suppressed.

References

[5.1] R.F. Harrington, *Field Computation by Moment Methods*, IEEE Press, New York, 1993.

[5.2] R. Coifman, V. Rokhlin and S. Wandzura, "The fast multipole method for the wave equation: a pedestrian prescription," *IEEE Antennas and Propagation Magazine*, vol.35, no.3, pp.7-12, June 1993

[5.3] J. M. Song, and W. C. Chew, "Multilevel fast-multipole algorithm for solving combined field integral equations of electromagnetic scattering," *Microwave and Optical Technology Letters*, Vol.10, No.1, pp.14-19, Sep. 1995.

[5.4] V. V. S. Prakash and Raj Mittra, "Characteristic basis function method: A New Technique for Efficient Solution of Method of Moments Matrix Equations," *Microwave and Optical Technology Letters*, Vol.36, No.2, Jan. 2003.

[5.5] C. S. Kim, Y. Rahmat-Samii, "Low profile antenna study using the physical optics hybrid method (POHM)", *in the Digest of IEEE International Symposium on Antennas and Propagation (AP-S)*, vol. 29, pp.1350-1353, June 1991.

[5.6] U. Jakobus and F.M. Landstorfer, "Improvement of the PO-MoM hybrid method by accounting for effects of perfectly conducting wedges," *IEEE Transaction on Antennas and Propagation*, vol.43, no.10, pp.11231129, Oct. 1995.

[5.7] R. F. Harrington, *Time-Harmonic Electromagnetic Fields*, pp.127-130, McGraw-Hill, New York. 1961

[5.8] C. A. Balanis, *Advanced Engineering Electromagnetics*, pp.694-696, New York. Wiley, 1989.

[5.9] Z.-L. Liu, X. Wang and C.-F. Wang, "Installed Performance Modeling of Complex Antenna Array Mounted on Extremely Large-Scale Platform Using Fast MoM-PO Hybrid Framework," *IEEE Transaction on Antennas and Propagation*, vol.62, no.7, pp.3852-3858, July 2014.

[5.10] K. Ito, T. Shijo, M. Ando, "Fresnel zone criterion to implement locality in the method of moments and PO-MoM hybrid method for the reduction of unknowns," *IEICE Transaction on Electronics*, vol.E94-C, no.1, pp72-79, Jan. 2011.

[5.11] O. M. Conde, J. Perez, M. P. Catedra, "Stationary phase method application for the analysis of radiation of complex 3-D conducting structures," *IEEE Transaction of Antennas and Propagatation*, vol.49, no.5, pp.724-731, May 2001.

[5.12] J. B. Keller, "Geometrical theory of diffraction," *Journal of the Optical Society of America*, vol.52, pp116-130, 1962.

[5.13] R. G. Kouyoumjian and R. H. Pathak, "A uniform geometrical theory of diffraction for an edge in a perfectly conducting surface," *Proceedings of the IEEE*, vol.62, no.11, pp.1448-1461, Nov. 1974.

[5.14] T. Shijo, T. Itoh, M. Ando, "Visualization of high frequency diffraction based on physical optics," *IEICE Transaction on Electronics* vol.E87-C, no.9, pp.1607-1614, Sep. 2004.

[5.15] T. Shijo, T. Hirano, and M. Ando, "Large-Size Local- Domain Basis Functions with Phase Detour and Fresnel Zone Threshold for Sparse Reaction Matrix in the Method of Moments," *IEICE Transaction on Electronics.*, Vol.E88-C, No.12, pp.2208-2215, Dec. 2005.

[5.16] T. Kohama and M. Ando, "Localization of Radiation Integrals Using the Fresnel Zone Numbers," *IEICE Transaction on Electronics* vol.E95-C, no.5, pp.928-935, May. 2012.

[5.17] W. D. Burnside, C. L. Yu and R. J. Marhefka, "A technique to combine the geometrical theory of diffraction and the moment method," *IEEE Transaction of Antennas and Propagatation*, vol.23, no.4, pp.551-558, July 1975.

[5.18] U. Jakobus and F. M. Landstorfer, "A combination of current-and ray-based techniques for the efficient analysis of electrically large scattering problems," *Proceedings of 13th Annual Review of Progress in Applied Computational Electromagnetics*, Monterey, CA, pp. 748-755, Mar. 1997.

[5.19] A. Boag, "A fast physical optics (FPO) algorithm for high frequency scattering," *IEEE Transaction on Antennas and Propagation*, vol.52, no.1, pp. 197- 204, Jan. 2004.

[5.20] F.A. Molinet, "Edge-excited rays on convex and concave structures: a review," *IEEE Antennas and Propagation Magazine*, vol.47, no.5, pp.34-46, Oct. 2005

[5.21] K. Goto, T. Kawano and T. Ishihara, "High-Frequency Analyses for Scattered Fields by a Cylindrically Curved Conducting Surface," *IEICE Transaction on Electronics*, vol.E92-C, no.1, pp25-32, Jan. 2009.

Chapter 6 Conclusions

6.1 Summary of the Preceding Chapters

The objectives of this thesis are to establish the localization methods which are based upon the Fresnel zone number criteria and are applicable to three-dimensional problems.

In Chapter 1, the representative methods for scattering analysis were at first reviewed. Through the introduction of high frequency approximations (HFA), numerically-accurate methods, and hybrid methods, the background and objective of this study were presented.

In Chapter 2, the physical meaning of localization method and Fresnel zone number criteria was explained. The localization method is analogous with the stationary phase method (SPM) in the sense that a surface integration can be replaced with contributions from scattering centers. However, the localization method doesn't lower the order of dimensions of integral unlike the SPM. A way to determine a boundary of local area around an inner stationary phase point (SPP) on an actual surface was here presented. The necessity of windowing function was also explained. It was confirmed that the raised cosine function named "EYE function" is the good candidate of windowing function. In this chapter, it was proposed that Fresnel zone number should be used as the argument of EYE function which was previously an actual distance from a scattering center. Difference of the arguments was numerically evaluated in the localization errors. The superiority of Fresnel zone number to an actual distance was confirmed and the criterion of $\Delta n_B = 3$ was obtained. The localization error was analytically derived only for the case when the observation angle θ is 0° or 180°. It was revealed that the errors depends on distance between a scatterer and a source, and that a relative error is suppressed to less than -29 dB. The frequency dependence of electrical size of local area was also analytically discussed and was concluded that its dependence is surely reduced from $O(f^2)$ to $O(f)$ level due to the localization.

In Chapter 3, localization of radiation integrals for three-dimensional problem was presented. A uniform treatment to define local areas around any scattering centers such as edge or corner diffraction points was established by introducing the modified surface-normal vectors. A way to determine a windowing value for multiply overlapped local areas was also established by introducing the vector $\hat{\sigma}$. These cares enable the application of localization of radiation integrals to scattering problem for a rectangular plate and a part of sphere with reasonable accuracy. It was confirmed that distribution of windowing values continuously varies depending on an observer position. As expected in Chapter 2, frequency dependence of electrical size of local areas is $O(f)$.

In Chapter 4, one method was shown, which realizes radiation integrals with the frequency-independent number of divisions by jointly using the Fresnel zone localization and adaptive sampling method. Due to the Fresnel zone localization, the area including the constant number of half oscillation of an integrand is truncated for any observation angle or frequency. Owing to the adaptive sampling method, one of half oscillation should be divided into the constant number of segments. These two technique realizes frequency-independent computational costs with constant computational accuracy. This hybrid technique was at first applied to two-dimensional problem of a conducting strip and rectangular cylinder. Expected frequency independence of computational accuracy and time was obtained for these models. The extension to three-dimensional problem was discussed. Contribution from an inner SPP on a planar and curved scatterer could be analyzed using the proposed hybrid technique.

In Chapter 5, the extension of Local-MoM to three-dimensional problems was treated. It was proposed that the EYE function should be applied to both of an incident field and induced currents with the exponent α and β, respectively. Several combinations of α and β were numerically examined and $\alpha = \beta = 0.5$ was obtained as the better condition. The implementation of Local-MoM into an MoM-based commercial simulator WIPL-D was achieved. This implementation indicates that the applicability of Local-MoM is high because an existing simulator is directly usable to realize the Local-MoM and it is unnecessary to newly develop a new simulator. In addition to that, some efficient techniques employed in an existing simulator directly accelerate the Local-MoM computation, such as higher-order basis function and GPU computing. The results for a part of sphere with an unlit region, which is difficult to be treated by HFA, shows that the Local-MoM technique is valid even for the problem where HFA methods cannot work. The Local-MoM has a great advantage in saving memory capacity and it leads to expanding the electrical size of scatterer, which can be handled with the memory capacity of 32GB, from $(40\lambda)^2$ to $(112\lambda)^2$.

6.2 Remarks for Future Studies

Remarks for future studies are listed as follows.

- Analytical expression of localization errors for an arbitrary case.
  The formulation of errors derived in Chapter 2 and Appendix B is limited to the case when θ is 0° or 180° and the observer is at an infinite distance. Derivation of it for an arbitrary case helps to controlling computational accuracy in the localization methods. Furthermore, derivation for any other windowing function is interesting in terms of searching the best function for localization.

- Application of localization methods to other structures with different shapes.
  In this thesis, only simple structures were calculated by the localization methods. In order to enhance the applicability of localization method, they should be applied to complicated structures. A scattering problem with other simple structures such as an elliptical cylinder is still interesting [6.1].

- Fresnel zone number criteria to PO-MoM analysis of three-dimensional problem.
  In [6.2, 3], a Fresnel zone number criterion for PO-MoM was also proposed and applied to two-dimensional problems. The extension of it to three-dimensional problems is expected although there is a possibility that some special techniques should be newly introduced as shown in 2.1.1 and 2.1.2. PO-MoM is recently available in some commercial simulators such as FEKO®. The implementation of the Fresnel zone number criterion into these simulators is also expected.

- Combination use of Local-MoM and the other fast methods.
  The Local-MoM is the method to directly reduce the number of unknowns N and frequency dependence of N. On the other hand, the FMM and MLFMM suppress N's dependence of computational costs. Combination use of Local-MoM and these fast methods would provide further reduction in computational costs.

- Localization of line integrals of equivalent edge currents (EEC)
  In this thesis, localization techniques for surface-radiation-integral type scattering analysis were discussed. Recently, a few examples were reported where Fresnel zone number localization was applied to line integrals of EEC [6.4, 5]. Its application gives a physical interpretation on results by line integral and saves computational time.

References

[6.1] T. Wang, M. Umehara, S. Takeda, T. Miyajima, and K. Kagoshima, "A calculation model of shadowing loss caused by a moving human body and its validation by experiments," *IEICE Technical Report*, vol. 114, no. 295, RCS2014-211, pp.85-90, Nov. 2014 (in Japanese).

[6.2] T. Shijo, M. Oishi, Y. Katakai, N. Omaki, K. Yukimasa, L. Rodriguez, and M. Ando, "Application of the Locality Principle in the Method of Moments for Induced Currents or Fields in Electrically Large Scattering Problems," *IEICE Technical Report*, vol.106, no.561, AP2006-169, pp.109-112, Mar. 2007.

[6.3] K. Ito, T. Shijo, and M. Ando, "Fresnel zone criterion to implement locality in the method of moments and PO-MoM hybrid method for the reduction of unknowns," *IEICE Transaction on Electronics*, vol.E94-C, no.1, pp72-79, Jan. 2011.

[6.4] P. Lu, "Surface-to-line integral reduction in physical optics for curved surfaces by modified edge representation," Ph.D. dissertation, Tokyo Institute of Technology, Mar. 2015.

[6.5] M. Ali, T. Kohama, and M. Ando, "Modified Edge Representation (MER) Consisting of Keller ' s Diffraction Coefficients With Weighted Fringe Waves and Its Localization for Evaluation of Corner Diffraction," *IEEE Transactions on Antennas and Propagation*, vol.63, no.7, pp.3158-3167, July 2015.

Acknowledgement

I would first like to express my spacial appreciation to my supervisor, Professor Makoto Ando for his kind guidance, valuable suggestions and continuous encouragement throughout this research. I would also like to express my gratitude to Professor Jiro Hirokawa for his fruitful advice.

I am deeply grateful to Professor Branko M. Kolundžija of University of Belgrade for his help and supervision on both of the life and research when I stayed in Belgrade, Serbia.

I am grateful to Professors in Tokyo Institute of Technology (Tokyo Tech): Junichi Takada, Atsuhiro Nishikata, Kei Sakaguchi, and Professor Matteo Albani of University of Siena for the evaluation of this dissertation. I also would like to appreciate to Kiyomichi Araki, Shigehisa Arai, Nobuhiko Nishiyama, and Tetsuya Mizumoto of Tokyo Tech for their valuable comments.

Many professors and researchers made valuable comments and questions on my presentations in conferences. I am especially grateful to Professor Keiji Goto of National Defense Agency of Japan and Professor Hiroshi Shirai of Chuo University for their fruitful comments.

I would like to thank to Assistant Professor Takuichi Hirano for discussions in laboratory seminars and his education on the computational electromagnetics. I also wish to express my thanks to Assistant Professor Kimio Sakurai for his support on experiments. I am thankful to secretaries Ms. Keiko Nagao, Ms. Akane Saito, Ms. Chieko Kondo, and Ms. Moto Sugano for their helps on my laboratory life.

I would like to express my gratitude to senior members of diffraction group Dr. Kenichi Sakina, Dr. Ruis Rodrigues, and Dr. Tetsu Shijo for their guidance to diffraction theories. I also wish to express my thanks to members of diffraction group Mr. Keita Ito, Dr. Lu Pengfei, Dr. Maifuz Ali, Mr. Ryosuke Hasaba and Mr. Takuhiko Sato. It is my pleasure to spend a lot of time on fundamental study and stimulating discussion on diffraction theory together with them.

I am grateful to Dr. Miao Zhang, Dr. Hideki Ueda, Dr. Yuanfeng She, Dr. Dongjin Kim, Dr. Takashi Tomura, Dr. Makoto Sano, Dr. Le Vu Hung and Dr. Nguyen Xuan Tung for their comments and encouragements. I thank to the other all the members of Ando and Hirokawa laboratory for a enjoyable laboratory life.

This work was financially supported by G-COE programs and Japan Society for the Promotion of Science (JSPS).

Finally, I express my respects to my parents and my brother for their continuous supports and patience.

List of Publications

A Publications Concerning This Dissertation

A.1 Journal Publications

[1] Takayuki Kohama and Makoto Ando, "Localization of Radiation Integrals Using the Fresnel Zone Numbers," *IEICE Transaction on Electronics* vol.E95-C, no.5, pp.928-935, May. 2012.

[2] Takayuki Kohama and Makoto Ando, "Physical Optics Radiation Integrals with Frequency-Independent Number of Division utilizing Fresnel Zone Number Localization and Adaptive Sampling Method," *IEICE Transaction on Electronics*, Vol.E97-C, No.12, pp.1134-1141, Dec. 2014.

[3] Takayuki Kohama and Makoto Ando, "Implementation of High Frequency Locality in the Method of Moments for 3-Dimensional Scattering Problems," *IEEE Transaction on Antennas and Propagation*, (Conditional Acceptance)

A.2 International Conferences

[1] Takayuki Kohama, Keita Ito, and Makoto Ando, "Abbreviated Analysis of Electromagnetic Fields Based upon Locality of Scattering Phenomena," *International Conference on Microwave Technology and Computational Electromagnetics (ICMTCE)*, B3-001, pp.372-375, May. 2011.

2 Takayuki Kohama, Keita Ito, and Makoto Ando, "Localization of Physical Optics Radiation Integrals Area in Scattering from a Rectangular Plate," *Proceedings of International Symposium on Antennas and Propagation (ISAP)*, Paper ID: WeF1-5, Korea, Oct. 2011.

[3] Takayuki Kohama and Makoto Ando, "Numerical Integration of Physical Optics for 2-Dimensional Scatterer using Fresnel Zone Numbers with Frequency-Independent Computation Time," *Proceedings of URSI Commission B International Symposium on Electromagnetic Theory (EMTS)*, paper no. 23PM3F-05, pp.789-791, Hiroshima, Japan, May 20-24, 2013.

[4] Takayuki Kohama and Makoto Ando, "Novel Techniques for Abbreviated Analysis of High Frequency Scattering Using the Fresnel Zone Numbers," *IEEE International*

Symposium on Antennas and Propagation (AP-S), Session: 533.4, Orlando, FL, USA, July 7-13, 2013.

[5] Takayuki Kohama and Makoto Ando, "Application of the Local-MoM with Reduced Matrix Size to the Dipole Scattering Analysis from a Rectangular Plate," *IEEE International Symposium on Antennas and Propagation (AP-S)*, Session: IF 346.9, Memphis, TN, USA, July 6-13, 2014.

[6] Takayuki Kohama and Makoto Ando, "Applicability of Local-MoM and Frequency Dependence of Computational Cost in Scattering Analysis of a Rectangular Plate from a Dipole," *Proceeding of 1st URSI Atlantic Radio Science Conference*, Paper ID: B01.5, Gran Canaria, Canary Islands, Spain, May 18-22, 2015.

[7] Takayuki Kohama and Makoto Ando, "Implementation of High Frequency Locality to Commercial MoM-based Simulator for 3-Dimensional Scattering Analysis," *IEEE International Symposium on Antennas and Propagation (AP-S)*, Session: WE-UB.5P.2, Vancouver, BC, Canada, July 19-24, 2015.

A.3 Technical Report on Electromagnetic Theory, IEE Japan

[1] Takayuki Kohama, Keita Ito, and Makoto Ando, "Reduction of Computational Load in High frequency EM Analysis Based upon the Locality of Diffraction," *The papers of Technical Meeting on Electromagnetic Theory, IEE Japan*, EMT-10-130, pp.159-164, Nov. 2010. (Japanese)

[2] Takayuki Kohama and Makoto Ando, "Abbreviated Analysis of High Frequency Scattering from a Rectangular Plate Based upon Its Locality," *The papers of Technical Meeting on Electromagnetic Theory, IEE Japan*, EMT-11-129, pp.7-12, Nov. 2011. (Japanese)

[3] Takayuki Kohama and Makoto Ando, "Divisions for Evaluating Radiation Integral in Localization Using the Fresnel Zone Numbers," *The papers of Technical Meeting on Electromagnetic Theory, IEE Japan*, EMT-12-066, pp.7-12, May 2012. (Japanese)

[4] Takayuki Kohama and Makoto Ando, "Frequency-independent Physical Optics Analysis of the Radar Cross Section for 2-dimensional Conducting Strip," *The papers of Technical Meeting on Electromagnetic Theory, IEE Japan*, EMT-12-144, pp.149-154, Nov. 2012. (Japanese)

[5] Takayuki Kohama and Makoto Ando, "Application of the Local-MoM to the Scattering Analysis from the Rectangular Plate," *The papers of Technical Meeting on Electromagnetic Theory, IEE Japan*, EMT-13-135, pp.1-6, Nov. 2013. (Japanese)

[6] Takayuki Kohama and Makoto Ando, "Usefulness of Local-MoM Using Commercial Electromagnetic Simulation Software," *The papers of Technical Meeting on Electromagnetic Theory, IEE Japan*, EMT-14-154, pp.35-39, Nov. 2014. (Japanese)

A.4 Technical Reports on Antennas and Propagation, IEICE Japan

[1] Takayuki Kohama, Keita Ito, and Makoto Ando, "Localization of Physical Optics Radiation Integrals in Scattering from a Rectangular Plate," *IEICE Technical Report*, AP2010-189, pp.95-100, Mar. 2011. (Japanese)

A.5 National Convention Records of IEICE Japan

[1] Takayuki Kohama, Keita Ito, and Makoto Ando, "Weighting Functions for Localization of Radiation Integrals in Scattering Problems," *in Proceedings of 2011 IEICE General Conference*, C-1-6, Mar. 2011. (Japanese)

[2] Takayuki Kohama and Makoto Ando, "Localization of Radiation Integrals for MoM Currents in Scattering from a Rectangular Plate," *in Proceedings of 2011 IEICE Electronics Society Conference*, C-1-24, Sep. 2011. (Japanese)

[3] Takayuki Kohama and Makoto Ando, "Weighting in Localization of Radiation Integrals with Nearby Scattering Centers," *in Proceedings of 2012 IEICE General Conference*, C-1-14, Mar. 2012. (Japanese)

[4] Takayuki Kohama, Takuichi Hirano, Jiro Hirokawa and Makoto Ando, "Application of the Fresnel Zone Numbers to Computational Load Reduction of Radiation Integrals and Preprocess of Numerical Solution in Scattering Problem —Frequency-Independent Solution Based upon the Locality and Reciprocity—" *in Proceedings of 2012 IEICE Electronics Society Conference*, CS-1-7, Sep. 2012. (Japanese)

[5] Takayuki Kohama and Makoto Ando, "Basic Study on the Application of Local-MoM to the 3-Dimensional Scattering Problem" *in Proceedings of 2013 IEICE Electronics Society Conference*, C-1-6, 2013-09. (Japanese)

[6] Takayuki Kohama and Makoto Ando, "Localization of Radiation Integral for Scatterer with an Unilluminated Region and a Wedge Diffraction Point," *in Proceedings of 2015 IEICE Electronics Society Conference*, C-1-8, Sep. 2015. (Japanese)

B Co-authored Publications

B.1 Journal Publications

[1] Maifuz Ali, **Takayuki Kohama** and Makoto Ando, "Modified Edge Representation (MER) Consisting of Keller ' s Diffraction Coefficients With Weighted Fringe Waves and Its Localization for Evaluation of Corner Diffraction," *IEEE Transactions on Antennas and Propagation*, vol.63, no.7, pp.3158-3167, July 2015

B.2 International Conferences

[1] Makoto Ando, **Takayuki Kohama**, Keita Ito, Tetsu Shijo, Takuichi Hirano and Jiro Hirokawa, "High Frequency Locality Embodied in terms of Fresnel Zone Number for Matrix Size Reduction in Method of Moments," *International Conference on Electromagnetics in Advanced Applications (ICEAA)*, pp.1432-1435, Sep. 2011.

[2] Makoto Ando, Lu Pengfei and **Takayuki Kohama**, "Discussion of physical optics surface integration for deep interpretation of GTD," *IEEE-APS Topical Conference on Antennas and Propagation in Wireless Communications (APWC)*, pp.1141-1144, 2-7 Sep. 2012.

[3] Makoto Ando, Maifuz Ali, Pengfei Lu and **Takayuki Kohama**, "Application of Fresnel Zone Numbers Localization for Equivalent Edge Currents Line Integration," *Proceedings of URSI Commission B International Symposium on Electromagnetic Theory (EMTS)*, paper no.: 24PM1F-03, pp.1061-1063, Hiroshima, Japan, May 20-24, 2013.

B.3 Technical Report on Electromagnetic Theory, IEE Japan

[1] Maifuz Ali, **Takayuki Kohama** and Makoto Ando, "Evaluation of Corner Diffraction using Modified Edge Representation (MER) with Fresnel Zone Localization for the Verification of Equivalent Edge Current at Arbitrary Point," *The papers of Technical Meeting on Electromagnetic Theory, IEE Japan*, EMT-13-129, pp. 61-66, Nov. 2013. (English)

B.4 National Convention Records of IEICE Japan

[1] Takuhiko Sato, **Takayuki Kohama** and Makoto Ando, "Analysis of 2-dimensional Multiple Reflection Using Modified Physical Optics," *in Proceedings of 2013 IEICE Electronics Society Conference*, C-1-5, Sep. 2013. (Japanese)

[2] Thanh Phan Do, Kiyomichi Araki, **Takayuki Kohama**, Takuichi Hirano, Jiro Hirokawa and Makoto Ando, "Estimation of antenna gain and radar cross section using Signal Flow Graph for wireless links with multiple reflection between transmitting and receiving antennas," *in Proceedings of 2015 IEICE Electronics Society Conference*, B-1-62, Sep. 2015. (Japanese)

C Awards

[1] Second Half of 2010 Student Best Presentation Award from Technical Committee on Antennas and Propagation of IEICE

[2] 2011 Student Best Presentation Award from Technical Committee on Electromagnetic Theory of IEE Japan

[3] 2013 Student Best Presentation Award from Technical Committee on Electromagnetic Theory of IEE Japan

[4] 2013 Young Researcher's Award of IEICE Japan

Appendix A

Geometrical Properties of Local Area with Elliptical Shape

A.1 Derivation of the Equation of Ellipse

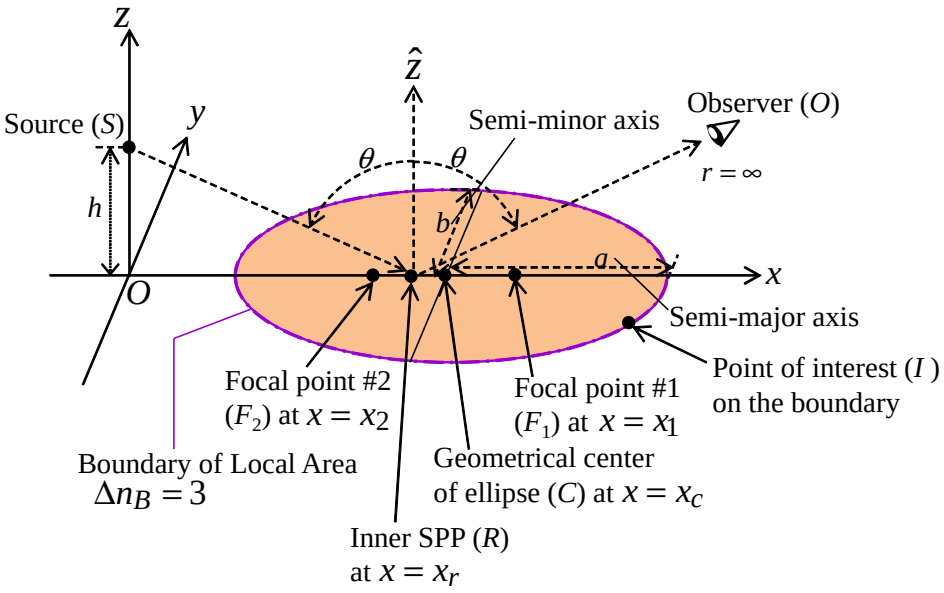

Figure A.1: Geometry of local area for the inner SPP.

A local area defined by the Fresnel zone number criterion becomes an ellipse when a scatterer is planar. Here, some of geometrical properties of the local area are derived. The geometry of a local area for an inner stationary phase point (SPP) is given in Fig. A.1. The observer is infinitely far from the inner SPP and the observation azimuth angle ϕ is set to 0° without loss of generality. The source lies on z-axis with a distance of $h \geq 0$ from the origin. The position vectors for the source, the inner SPP, and a point of interest with respect to the origin are denoted as $\boldsymbol{r}_s$, $\boldsymbol{r}_r$, and $\boldsymbol{r}_i$, respectively, and the unit vector from the origin to the observer is $\hat{r}_o$. In the Cartesian coordinate system, they are expressed as

follows;

$$\boldsymbol{r}_s = (0, 0, h) \tag{A.1}$$
$$\boldsymbol{r}_r = (x_r, 0, 0) \tag{A.2}$$
$$x_r = h\frac{\sin\theta}{|\cos\theta|} \tag{A.3}$$
$$\boldsymbol{r}_i = (x, y, 0) \tag{A.4}$$
$$\hat{r}_o = (\sin\theta, 0, \cos\theta) \tag{A.5}$$

According to the Fresnel zone number criterion, the boundary of local area is expressed as

$$|\boldsymbol{r}_i - \boldsymbol{r}_s| + |\boldsymbol{r}_r - \boldsymbol{r}_s| - (\boldsymbol{r}_i - \boldsymbol{r}_r) \cdot \hat{r}_o = \frac{\lambda}{2}\Delta n_B \tag{A.6}$$

where λ is the wavelength and Δn_B is the parameter to determine size of local area. By substituting (A.1) to (A.5) for (A.6), we obtain

$$\begin{aligned}
&\sqrt{x^2 + y^2 + h^2} + h\frac{\sin\theta}{|\cos\theta|} - \left(x - h\frac{\sin\theta}{|\cos\theta|}\right)\sin\theta = \frac{\lambda}{2}\Delta n_B \\
\Longleftrightarrow &x^2 + y^2 + h^2 = \left\{\frac{\lambda}{2}\Delta n_B - h\frac{\sin\theta}{|\cos\theta|} + \left(x - h\frac{\sin\theta}{|\cos\theta|}\right)\sin\theta\right\}^2 \\
\Longleftrightarrow &\frac{(x - x_c)}{a^2} + \frac{y^2}{b^2} = 1
\end{aligned} \tag{A.7}$$

where a and b are the lengths of semi-major axis and semi-minor axis, respectively, and x_c denotes the x position of center of ellipse. They are expressed as

$$a = \frac{\sqrt{\left(\frac{\lambda}{2}\Delta n_B\right)^2 + 2h\left(\frac{\lambda}{2}\Delta n_B\right)|\cos\theta|}}{\cos^2\theta} = \frac{b}{|\cos\theta|} \tag{A.8}$$
$$b = \frac{\sqrt{\left(\frac{\lambda}{2}\Delta n_B\right)^2 + 2h\left(\frac{\lambda}{2}\Delta n_B\right)|\cos\theta|}}{|\cos\theta|} \tag{A.9}$$
$$x_c = \frac{\left(h|\cos\theta| + \frac{\lambda}{2}\Delta n_B\right)\sin\theta}{\cos^2\theta} = x_r + \frac{\frac{\lambda}{2}\Delta n_B \sin\theta}{\cos^2\theta}. \tag{A.10}$$

Obviously, x_c doesn't coincide with x_r except the case of $\sin\theta = 0$.

The x positions for two focal points denoted as x_1 and x_2 are obtained by the following

equations;

$$\begin{aligned} x_1 =& x_c + \sqrt{a^2 - b^2} = x_c + b\,|\tan\theta| \\ =& x_r + \frac{\frac{\lambda}{2}\Delta n_B \sin\theta + \sqrt{\left(\frac{\lambda}{2}\Delta n_B\right)^2 + 2h\left(\frac{\lambda}{2}\Delta n_B\right)|\cos\theta|}\,|\sin\theta|}{\cos^2\theta} \end{aligned} \tag{A.11}$$

$$\begin{aligned} x_2 =& x_c - \sqrt{a^2 - b^2} = x_c - b\,|\tan\theta| \\ =& x_r + \frac{\frac{\lambda}{2}\Delta n_B \sin\theta - \sqrt{\left(\frac{\lambda}{2}\Delta n_B\right)^2 + 2h\left(\frac{\lambda}{2}\Delta n_B\right)|\cos\theta|}\,|\sin\theta|}{\cos^2\theta} \end{aligned} \tag{A.12}$$

Here, the relationship of

$$\begin{aligned} \sqrt{a^2 - b^2} =& \sqrt{\left(\frac{b}{|\cos\theta|}\right)^2 - b^2} \\ =& b\sqrt{\frac{1}{\cos^2\theta} - 1} \\ =& b\,|\tan\theta| \end{aligned} \tag{A.13}$$

is utilized. As (A.11) and (A.12) shows, neither of the two focal point coincides with the inner SPP except the case of $\sin\theta = 0$.

A.2 A True Circle Case

When $\sin\theta = 0$, the local area becomes a true circle. The radius R $(= a = b)$ of the circle is obtained by substituting $|\cos\theta| = 1$ for (A.8) and (A.9).

$$R = \sqrt{\left(\frac{\lambda}{2}\Delta n_B\right)^2 + 2h\left(\frac{\lambda}{2}\Delta n_B\right)} \tag{A.14}$$

As we explained before, only in this case, the center of ellipse and the inner SPP are coincident.

Appendix B

Error Due to the Localization

B.1 Integral Form of a Scattered Field from a Local Area

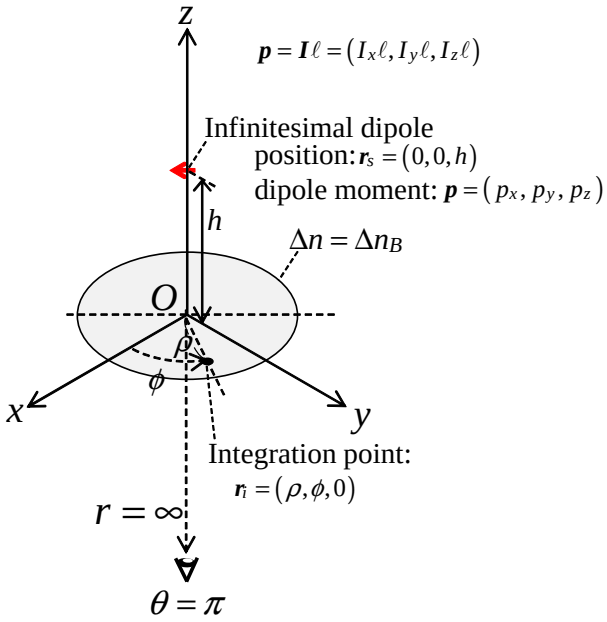

Figure B.1: Geometry of the problem.

In Appendix B, an error due to the localization is analytically derived. The geometry of the problem is given in Fig. B.1. A scatterer is an infinite plane of perfect electric conductor (PEC) at $z = 0$ and a source lies on z-axis with a distance of $h \geq 0$ from the origin. The normal unit vector of the plane $\hat{n}$ is identical to $\hat{z}$. The analytical expression can be obtained only for $\sin\theta = 0$ case. Here, the case when the observer is located at $\theta = \pi$ and $r = \infty$ is treated. The infinitesimal dipole moment is denoted as $\boldsymbol{p} = \boldsymbol{I}\ell$ where $\boldsymbol{I}$ is the electric current vector and ℓ is the length of dipole. The position vectors for the source, integration point, and unit vector to the observer with respect to the origin are

denoted as $\boldsymbol{r_s}$, $\boldsymbol{r_i}$ and $\hat{r_o}$, respectively. They are expressed as follows;

$$\boldsymbol{r_s} = (0, 0, h) = h\hat{z} \tag{B.1}$$
$$\boldsymbol{r_i} = (\rho \sin\phi, \rho\cos\phi, 0) = \rho\hat{\rho} \tag{B.2}$$
$$\hat{r_o} = (0, 0, -1) = -\hat{z} \tag{B.3}$$

We define the vector $\boldsymbol{R}$ as $\boldsymbol{R} = \boldsymbol{r}_i - \boldsymbol{r}_s = \rho\hat{\rho} - h\hat{z}$. Using $\boldsymbol{R}$ and (B.1) to (B.3), the PO currents $\boldsymbol{J}_{PO}$ is expressed as follows;

$$\boldsymbol{J}_{PO} = 2\hat{n} \times \boldsymbol{H}^i \tag{B.4}$$
$$\boldsymbol{H}^i = \frac{e^{-jkR}}{j4\pi R} k \left(-1 - \frac{1}{jkR}\right) \boldsymbol{p} \times \hat{R} \tag{B.5}$$
$$R = |\boldsymbol{R}| = \sqrt{\rho^2 + h^2} \tag{B.6}$$
$$\hat{R} = \frac{\boldsymbol{R}}{R} = \frac{\rho\hat{\rho} - h\hat{z}}{R} = \frac{\rho\hat{\rho} - h\hat{z}}{\sqrt{\rho^2 + h^2}} \tag{B.7}$$

where k is the wavenumber as $k = 2\pi/\lambda$ and λ is the wavelength. Note that the induced currents $\boldsymbol{J}$ on the infinite PEC plane is rigorously identical to PO's currents $\boldsymbol{J}_{PO}$.

Let us consider the radiation integral with a windowing function $W(\Delta n/\Delta n_B)$ for the local area where $\Delta n \leq \Delta n_B$ holds. Here, $W(\Delta n/\Delta n_B)$ is not necessarily the EYE function of (B.8).

$$EYE\left(\frac{\Delta n}{\Delta n_B}\right) = \begin{cases} \frac{1}{2}\left\{\cos\left(\frac{\Delta n}{\Delta n_B}\pi\right) + 1\right\} & \Delta n \leq \Delta n_B \\ 0 & \text{otherwise} \end{cases} \tag{B.8}$$

As for the definition of Δn and Δn_B, please refer to the chapter 2.

By substituting (B.5) for (B.4), we obtain

$$\begin{aligned} \boldsymbol{J}_{PO} &= \frac{ke^{-jkR}}{j2\pi R}\left(-1 - \frac{1}{jkR}\right)\hat{n} \times \left(\boldsymbol{p} \times \hat{R}\right) \\ &= \frac{ke^{-jkR}}{j2\pi R}\left(-1 - \frac{1}{jkR}\right)\left\{\left(\hat{n}\cdot\hat{R}\right)\boldsymbol{p} - (\hat{n}\cdot\boldsymbol{p})\,\hat{R}\right\} \\ &= \frac{ke^{-jkR}}{j2\pi R}\left(-1 - \frac{1}{jkR}\right)\left\{-\frac{h}{R}\boldsymbol{p} - (\hat{n}\cdot\boldsymbol{p})\,\hat{R}\right\}. \end{aligned} \tag{B.9}$$

From the definition of Δn, the following equation is obtained.

$$\begin{aligned} \sqrt{\rho^2 + h^2} - h &= \frac{\lambda}{2}\cdot\Delta n \\ \Longleftrightarrow \rho &= \sqrt{\left(\frac{\lambda}{2}\cdot\Delta n\right)^2 + \lambda\cdot\Delta n\cdot h} \end{aligned} \tag{B.10}$$

In the cylindrical coordinate system, the integration area is expresses as $0 \leq \rho \leq \rho_{\max}$ and $0 \leq \phi \leq 2\pi$ where $\rho_{\max}$ is given by replacing Δn with Δn_B.

Here, an electric vector potential $\boldsymbol{A}^J$ is derived. The free-space Green's function for the Helmholtz equation is denoted as $G(\boldsymbol{r}_i; \boldsymbol{r}_o) = \exp(-jk|\boldsymbol{r}_i - \boldsymbol{r}_o|) / (4\pi|\boldsymbol{r}_i - \boldsymbol{r}_o|)$. Assuming the far field approximation and $\theta = \pi$, the exponential term is identical to 1 and the attenuation of $1/|\boldsymbol{r}_i - \boldsymbol{r}_o|$ is ignored. So we obtain

$$\begin{aligned}
\boldsymbol{A}^J &= \mu \iint_{\Delta n \leq \Delta n_B} W\left(\frac{\Delta n}{\Delta n_B}\right) \boldsymbol{J}_{PO} G(\boldsymbol{r}_i; \boldsymbol{r}_o)\, dS \\
&= \frac{\mu k}{j8\pi^2} \iint_{\Delta n \leq \Delta n_B} W\left(\frac{\Delta n}{\Delta n_B}\right) e^{-jkR} \left(\frac{1}{R} + \frac{1}{jkR^2}\right) \left\{\frac{h}{R}\boldsymbol{p} + (\hat{n}\cdot\boldsymbol{p})\,\hat{R}\right\} dS \\
&= \frac{\mu k}{j8\pi^2} \int_{\rho=0}^{\rho_{\max}} \int_{\phi=0}^{2\pi} W\left(\frac{\Delta n}{\Delta n_B}\right) e^{-jkR} \left(\frac{1}{R} + \frac{1}{jkR^2}\right) \left\{\frac{h}{R}\boldsymbol{p} + (\hat{n}\cdot\boldsymbol{p})\,\hat{R}\right\} \rho\, d\rho d\phi \\
&= \frac{\mu k}{j8\pi^2} \int_{\rho=0}^{\rho_{\max}} W\left(\frac{\Delta n}{\Delta n_B}\right) e^{-jkR} \left(\frac{1}{R} + \frac{1}{jkR^2}\right) \rho \left[\int_{\phi=0}^{2\pi} \left\{\frac{h}{R}\boldsymbol{p} + (\hat{n}\cdot\boldsymbol{p})\,\hat{R}\right\} d\phi\right] d\rho.
\end{aligned} \tag{B.11}$$

where μ is the magnetic permeability.

Let us consider the integration regarding ϕ. The first term is the constant value for ϕ. From the rotational symmetry, only the z component remains after the integration of the second term. Moreover, the z component finally vanishes when we consider a far field for $\theta = \pi$ because the far electric field $\boldsymbol{E}^S$ is given as follows;

$$\boldsymbol{E}^S = -j\omega \boldsymbol{A}^J_{\perp} \tag{B.12}$$

$$\boldsymbol{A}^J_{\perp} = \boldsymbol{A}^J - \hat{r}_o\left(\hat{r}_o \cdot \boldsymbol{A}^J\right) = -\hat{r}_o \times \left(\hat{r}_o \times \boldsymbol{A}^J\right) \tag{B.13}$$

where ω is the angular frequency.

Considering (B.3), (B.11), and (B.13), (B.12) is converted to a single integral form regarding ρ.

$$\begin{aligned}
\boldsymbol{E}^S &= \frac{\omega\mu k}{8\pi^2} \int_{\rho=0}^{\rho_{\max}} W\left(\frac{\Delta n}{\Delta n_B}\right) e^{-jkR} \left(\frac{1}{R} + \frac{1}{jkR^2}\right) \rho \frac{2\pi h}{R} \left\{\hat{r}_o \times (\hat{r}_o \times \boldsymbol{p})\right\} d\rho \\
&= \frac{\omega\mu k h}{4\pi} \left\{\hat{r}_o \times (\hat{r}_o \times \boldsymbol{p})\right\} \int_{\rho=0}^{\rho_{\max}} W\left(\frac{\Delta n}{\Delta n_B}\right) e^{-jkR} \left(\frac{1}{R} + \frac{1}{jkR^2}\right) \frac{\rho}{R} d\rho \\
&= \boldsymbol{E}_0 I_L
\end{aligned} \tag{B.14}$$

where

$$\boldsymbol{E}_0 = \frac{\omega\mu kh}{4\pi} e^{-jkh} \{\hat{r}_o \times (\hat{r}_o \times \boldsymbol{p})\} \tag{B.15}$$

$$I_L = \int_{\rho=0}^{\rho_{\max}} W\left(\frac{\Delta n}{\Delta n_B}\right) e^{-jkR} \left(\frac{1}{R} + \frac{1}{jkR^2}\right) \frac{\rho}{R} d\rho \tag{B.16}$$

Here, the variable of integration I_L is replaced with Δn.

$$\begin{aligned} \Delta n &= \frac{2}{\lambda}\left(\sqrt{\rho^2 + h^2} - h\right) \\ &= \frac{2}{\lambda}(R - h) \end{aligned} \tag{B.17}$$

$$\iff \quad d\Delta n = \frac{2}{\lambda} \cdot \frac{\rho}{\sqrt{\rho^2 + h^2}} d\rho$$

$$\iff \frac{\lambda}{2} d\Delta n = \frac{\rho}{R} d\rho \tag{B.18}$$

Using (B.17) and (B.18), I_L is converted to the integration for Δn as follows.

$$\begin{aligned} I_L &= \int_{\rho=0}^{\rho_{\max}} W\left(\frac{\Delta n}{\Delta n_B}\right) e^{-jkR} \left(\frac{1}{R} + \frac{1}{jkR^2}\right) \frac{\rho}{R} d\rho \\ &= \int_{\Delta n=0}^{\Delta n_B} W\left(\frac{\Delta n}{\Delta n_B}\right) e^{-jk\left(\frac{\lambda}{2}\Delta n + h\right)} \left\{ \frac{1}{\frac{\lambda}{2}\Delta n + h} + \frac{1}{jk\left(\frac{\lambda}{2}\Delta n + h\right)^2} \right\} \frac{\lambda}{2} d\Delta n \\ &= \int_{\Delta n=0}^{\Delta n_B} W\left(\frac{\Delta n}{\Delta n_B}\right) \left\{ \frac{e^{-j\pi\Delta n}}{\Delta n + \frac{2}{\lambda}h} + \frac{e^{-j\pi\Delta n}}{j\pi\left(\Delta n + \frac{2}{\lambda}h\right)^2} \right\} d\Delta n \end{aligned} \tag{B.19}$$

We later evaluate I_L. The discussion so far is valid for any $W(\Delta n/\Delta n_B)$.

B.2 $W(\Delta n/\Delta n_B) = EYE(\Delta n/\Delta n_B)$ Case

We introduce some of the special functions. The sine integral and cosine integral defined by (B.20) and (B.21) are used to introduce $\mathrm{E}(x)$.

$$\mathrm{si}(x) = -\int_x^{\infty} \frac{\sin t}{t} dt \tag{B.20}$$

$$\mathrm{ci}(x) = -\int_x^{\infty} \frac{\cos t}{t} dt \tag{B.21}$$

$$\mathrm{E}(x) = -\int_x^{\infty} \frac{e^{-jt}}{t} dt = \mathrm{ci}(x) - j\,\mathrm{si}(x) \tag{B.22}$$

The asymptotic formulas of these for $x \gg 1$ are given as

$$\mathrm{si}(x) \sim -\frac{\cos x}{x} \tag{B.23}$$

$$\mathrm{ci}(x) \sim \frac{\sin x}{x} \tag{B.24}$$

$$\mathrm{E}(x) \sim \frac{je^{-jx}}{x}. \tag{B.25}$$

For the later discussion, we derive the following formulations.

$$\begin{aligned}\int \frac{e^{-jbt}}{t+a}dt &= \int \frac{e^{-jb\left(\frac{u}{b}-a\right)}}{\frac{1}{b}u}\frac{1}{b}du \qquad (u = b(t+a) \text{ is used}) \\ &= e^{+jba}\int \frac{e^{-ju}}{u}du \end{aligned} \tag{B.26}$$

$$\int \frac{e^{-jt}}{t^2}dt = -\frac{e^{-jt}}{t} - j\int \frac{e^{-jt}}{t}dt \tag{B.27}$$

$$\begin{aligned}\int \frac{e^{-jbt}}{(t+a)^2}dt &= \int \frac{e^{-jb\left(\frac{u}{b}-a\right)}}{\left(\frac{u}{b}\right)^2}\frac{1}{b}du \qquad (u = b(t+a) \text{ is used}) \\ &= -be^{+jba}\left(\frac{e^{-ju}}{u} + j\int \frac{e^{-ju}}{u}du\right) \end{aligned} \tag{B.28}$$

Here, we derive the rigorous solution by two ways. First one is based on the image theory. At first, the incident field $\boldsymbol{E}^i$ from the actual (not image) source is given by

$$\boldsymbol{E}^i = \frac{e^{-jkR}}{j4\pi R}k\eta\left[\left\{-1 - \frac{3}{jkR} - \frac{3}{(jkR)^2}\right\}\left(\boldsymbol{p}\cdot\hat{R}\right)\boldsymbol{p} + \left\{-1 + \frac{1}{jkR} + \frac{1}{(jkR)^2}\right\}\boldsymbol{p}\right]. \tag{B.29}$$

Assuming a far field with $R \to \infty$ and $\theta = \pi$, (B.29) is converted into

$$\begin{aligned}\boldsymbol{E}^i &= \frac{e^{+jk\boldsymbol{r}_s\cdot\hat{r}_o}}{j4\pi}k\eta\left\{\boldsymbol{p} - (\boldsymbol{p}\cdot\hat{r}_o)\boldsymbol{p}\right\} \\ &= -\frac{e^{+jk\boldsymbol{r}_s\cdot\hat{r}_o}}{j4\pi}k\eta\left\{\hat{r}_o\times(\hat{r}_o\times\boldsymbol{p})\right\}. \end{aligned} \tag{B.30}$$

Considering the image theory and $\theta = \pi$, $\boldsymbol{p}$ in (B.30) is replaced with $-\boldsymbol{p}$ and $\hat{r}_o\cdot\boldsymbol{r}_s = -h$ is used. We obtain the incident far field from the image source $\boldsymbol{E}_{\mathrm{image}}$ as follows;

$$\boldsymbol{E}_{\mathrm{image}} = \frac{e^{-jkh}}{j4\pi}k\eta\left\{\hat{r}_o\times(\hat{r}_o\times\boldsymbol{p})\right\} \tag{B.31}$$

The second way is to evaluate I_L with $W(\Delta n/\Delta n_B) = 1$ and $\Delta n_B \to \infty$. Only $W(\Delta n/\Delta n_B) = 1$ is at first applied to (B.16).

$$\begin{aligned} I_L &= \int_{\Delta n=0}^{\Delta n_B} \left\{ \frac{e^{-j\pi\Delta n}}{\Delta n + \frac{2}{\lambda}h} + \frac{e^{-j\pi\Delta n}}{j\pi\left(\Delta n + \frac{2}{\lambda}h\right)^2} \right\} d\Delta n \\ &= e^{+jkh} \int_{u=kh}^{k\left(h+\frac{\lambda}{2}\Delta n_B\right)} \left(\frac{e^{-ju}}{u} + \frac{e^{-ju}}{ju^2} \right) du \\ &= e^{+jkh} \left[\mathrm{E}(u) - \frac{e^{-ju}}{ju} - \mathrm{E}(u) \right]_{u=kh}^{k\left(h+\frac{\lambda}{2}\right)\Delta n_B} \\ &= -e^{+jkh} \left[\frac{e^{-ju}}{ju} \right]_{u=kh}^{k\left(h+\frac{\lambda}{2}\right)\Delta n_B} \end{aligned} \tag{B.32}$$

And then $\Delta n_B \to \infty$ is applied.

$$\begin{aligned} I_\infty &= \lim_{\Delta n_B \to \infty} I_L \\ &= -e^{+jkh} \left(-\frac{e^{-jkh}}{jkh} \right) \\ &= \frac{1}{jkh} \end{aligned} \tag{B.33}$$

By replacing I_∞ with I_L and using $\omega\mu = k\eta$, we again obtain the reference of far electric field $\boldsymbol{E}_{\mathrm{ref}}$ as follows.

$$\begin{aligned} \boldsymbol{E}_{\mathrm{ref}} &= \boldsymbol{E}_0 I_\infty \\ &= \frac{\omega\mu kh}{4\pi} e^{-jkh} \left\{ \hat{r}_o \times (\hat{r}_o \times \boldsymbol{p}) \right\} \frac{1}{jkh} \\ &= \frac{e^{-jkh}}{j4\pi} k\eta \left\{ \hat{r}_o \times (\hat{r}_o \times \boldsymbol{p}) \right\} \end{aligned} \tag{B.34}$$

This is totally identical to (B.31). So we define $\boldsymbol{E}^S_{\mathrm{Exact}}$ as $\boldsymbol{E}^S_{\mathrm{Exact}} = \boldsymbol{E}_{\mathrm{ref}} = \boldsymbol{E}_{\mathrm{image}} = \boldsymbol{E}_0 I_\infty$.

Next, we evaluate I_L with $W(\Delta n/\Delta n_B) = EYE(\Delta n/\Delta n_B)$ using

$$\begin{aligned} \frac{1}{2}\left\{ \cos\left(\frac{\Delta n}{\Delta n_B}\pi \right) + 1 \right\} &= \frac{1}{2} + \frac{1}{2}\cos\left(\frac{\Delta n}{\Delta n_B}\pi \right) \\ &= \frac{1}{2} + \frac{1}{4}\left\{ \exp\left(+j\frac{\Delta n}{\Delta n_B}\pi \right) + \exp\left(-j\frac{\Delta n}{\Delta n_B}\pi \right) \right\}. \end{aligned} \tag{B.35}$$

By substituting (B.35), we obtain the following formulation.

$$I_L = \frac{1}{2}I_0 + \frac{1}{4}I_+ + \frac{1}{4}I_- \tag{B.36}$$

$$\begin{aligned}
I_0 =& \int_{\Delta n=0}^{\Delta n_B} \left\{ \frac{e^{-j\pi\Delta n}}{\Delta n + \frac{2}{\lambda}h} + \frac{e^{-j\pi\Delta n}}{j\pi\left(\Delta n + \frac{2}{\lambda}h\right)^2} \right\} d\Delta n \\
=& -e^{+jkh}\left[\frac{e^{-ju}}{ju}\right]_{u=kh}^{k\left(h+\frac{\lambda}{2}\Delta n_B\right)} \\
=& -\frac{e^{+jkh}}{j}\left\{ \frac{e^{-jk\left(h+\frac{\lambda}{2}\Delta n_B\right)}}{k\left(h+\frac{\lambda}{2}\Delta n_B\right)} - \frac{e^{-jkh}}{kh} \right\} \\
=& -\frac{1}{j}\left\{ \frac{e^{-j\pi\Delta n_B}}{k\left(h+\frac{\lambda}{2}\Delta n_B\right)} - \frac{1}{kh} \right\}
\end{aligned} \tag{B.37}$$

$$\begin{aligned}
I_+ =& \int_{\Delta n=0}^{\Delta n_B} \left\{ \frac{e^{-j\pi\Delta n\left(1+\frac{1}{\Delta n_B}\right)}}{\Delta n + \frac{2}{\lambda}h} + \frac{1}{j\pi}\frac{e^{-j\pi\Delta n\left(1+\frac{1}{\Delta n_B}\right)}}{\left(\Delta n + \frac{2}{\lambda}h\right)^2} \right\} d\Delta n \\
=& e^{+jkh\left(1+\frac{1}{\Delta n_B}\right)}\left[\mathrm{E}(u)\right]_{u=kh\left(1+\frac{1}{\Delta n_B}\right)}^{k\left(h+\frac{\lambda}{2}\Delta n_B\right)\left(1+\frac{1}{\Delta n_B}\right)} \\
& -\frac{1}{j}\left(1+\frac{1}{\Delta n_B}\right)e^{+jkh\left(1+\frac{1}{\Delta n_B}\right)}\left[\frac{e^{-ju}}{u} + j\,\mathrm{E}(u)\right]_{u=kh\left(1+\frac{1}{\Delta n_B}\right)}^{k\left(h+\frac{\lambda}{2}\Delta n_B\right)\left(1+\frac{1}{\Delta n_B}\right)} \\
=& -\frac{1}{j}\left(1+\frac{1}{\Delta n_B}\right)e^{+jkh\left(1+\frac{1}{\Delta n_B}\right)}\left[\frac{e^{-ju}}{u}\right]_{u=kh\left(1+\frac{1}{\Delta n_B}\right)}^{k\left(h+\frac{\lambda}{2}\Delta n_B\right)\left(1+\frac{1}{\Delta n_B}\right)} \\
& -\frac{1}{\Delta n_B}e^{+jkh\left(1+\frac{1}{\Delta n_B}\right)}\left[\mathrm{E}(u)\right]_{u=kh\left(1+\frac{1}{\Delta n_B}\right)}^{k\left(h+\frac{\lambda}{2}\Delta n_B\right)\left(1+\frac{1}{\Delta n_B}\right)}
\end{aligned} \tag{B.38}$$

$$\begin{aligned}
I_- =& \int_{\Delta n=0}^{\Delta n_B} \left\{ \frac{e^{-j\pi\Delta n\left(1-\frac{1}{\Delta n_B}\right)}}{\Delta n + \frac{2}{\lambda}h} + \frac{1}{j\pi}\frac{e^{-j\pi\Delta n\left(1-\frac{1}{\Delta n_B}\right)}}{\left(\Delta n + \frac{2}{\lambda}h\right)^2} \right\} d\Delta n \\
=& e^{+jkh\left(1-\frac{1}{\Delta n_B}\right)}\left[\mathrm{E}(u)\right]_{u=kh\left(1-\frac{1}{\Delta n_B}\right)}^{k\left(h+\frac{\lambda}{2}\Delta n_B\right)\left(1-\frac{1}{\Delta n_B}\right)} \\
& -\frac{1}{j}\left(1-\frac{1}{\Delta n_B}\right)e^{+jkh\left(1-\frac{1}{\Delta n_B}\right)}\left[\frac{e^{-ju}}{u} + j\,\mathrm{E}(u)\right]_{u=kh\left(1-\frac{1}{\Delta n_B}\right)}^{k\left(h+\frac{\lambda}{2}\Delta n_B\right)\left(1-\frac{1}{\Delta n_B}\right)} \\
=& -\frac{1}{j}\left(1-\frac{1}{\Delta n_B}\right)e^{+jkh\left(1-\frac{1}{\Delta n_B}\right)}\left[\frac{e^{-ju}}{u}\right]_{u=kh\left(1-\frac{1}{\Delta n_B}\right)}^{k\left(h+\frac{\lambda}{2}\Delta n_B\right)\left(1-\frac{1}{\Delta n_B}\right)} \\
& +\frac{1}{\Delta n_B}e^{+jkh\left(1-\frac{1}{\Delta n_B}\right)}\left[\mathrm{E}(u)\right]_{u=kh\left(1-\frac{1}{\Delta n_B}\right)}^{k\left(h+\frac{\lambda}{2}\Delta n_B\right)\left(1-\frac{1}{\Delta n_B}\right)}
\end{aligned} \tag{B.39}$$

Note that (B.39) is invalid for $\Delta n_B = 1$. In that case, (B.40) is used instead.

$$I_- = \left[\ln u - \frac{u}{j\pi}\right]_{u=\frac{2h}{\lambda}}^{1+\frac{2h}{\lambda}} \tag{B.40}$$

We here define $\kappa = I_L/I_\infty$ as the ratio of the localization's result to the exact solution.

B.3 Asymptotic Formula of I_L and κ

From now, we derive the asymptotic formula of (B.36). When $kh \gg 1$ and $\Delta n_B \geq 2$, $x \gg 1$ for $\mathrm{E}(x)$ holds. By using (B.25), (B.36), (B.38), (B.39) and κ are approximated as

$$\begin{aligned}
I_+ \sim & -\frac{1}{j}\left(1+\frac{1}{\Delta n_B}\right) e^{+jkh\left(1+\frac{1}{\Delta n_B}\right)} \left[\frac{e^{-ju}}{u}\right]_{u=kh\left(1+\frac{1}{\Delta n_B}\right)}^{k\left(h+\frac{\lambda}{2}\Delta n_B\right)\left(1+\frac{1}{\Delta n_B}\right)} \\
& -\frac{1}{\Delta n_B} e^{+jkh\left(1+\frac{1}{\Delta n_B}\right)} \left[\frac{je^{-ju}}{u}\right]_{u=kh\left(1+\frac{1}{\Delta n_B}\right)}^{k\left(h+\frac{\lambda}{2}\Delta n_B\right)\left(1+\frac{1}{\Delta n_B}\right)} \\
= & -\frac{1}{j} e^{+jkh\left(1+\frac{1}{\Delta n_B}\right)} \left[\frac{e^{-ju}}{u}\right]_{u=kh\left(1+\frac{1}{\Delta n_B}\right)}^{k\left(h+\frac{\lambda}{2}\Delta n_B\right)\left(1+\frac{1}{\Delta n_B}\right)} \\
= & -\frac{1}{j}\left\{\frac{e^{-j\pi(\Delta n_B+1)}}{k\left(h+\frac{\lambda}{2}\Delta n_B\right)\left(1+\frac{1}{\Delta n_B}\right)} - \frac{1}{kh\left(1+\frac{1}{\Delta n_B}\right)}\right\}
\end{aligned} \tag{B.41}$$

$$\begin{aligned}
I_- \sim & -\frac{1}{j}\left(1-\frac{1}{\Delta n_B}\right) e^{+jkh\left(1-\frac{1}{\Delta n_B}\right)} \left[\frac{e^{-ju}}{u}\right]_{u=kh\left(1-\frac{1}{\Delta n_B}\right)}^{k\left(h+\frac{\lambda}{2}\Delta n_B\right)\left(1-\frac{1}{\Delta n_B}\right)} \\
& +\frac{1}{\Delta n_B} e^{+jkh\left(1-\frac{1}{\Delta n_B}\right)} \left[\frac{je^{-ju}}{u}\right]_{u=kh\left(1-\frac{1}{\Delta n_B}\right)}^{k\left(h+\frac{\lambda}{2}\Delta n_B\right)\left(1-\frac{1}{\Delta n_B}\right)} \\
= & -\frac{1}{j} e^{+jkh\left(1-\frac{1}{\Delta n_B}\right)} \left[\frac{e^{-ju}}{u}\right]_{u=kh\left(1-\frac{1}{\Delta n_B}\right)}^{k\left(h+\frac{\lambda}{2}\Delta n_B\right)\left(1-\frac{1}{\Delta n_B}\right)} \\
= & -\frac{1}{j}\left\{\frac{e^{-j\pi(\Delta n_B-1)}}{k\left(h+\frac{\lambda}{2}\Delta n_B\right)\left(1-\frac{1}{\Delta n_B}\right)} - \frac{1}{kh\left(1-\frac{1}{\Delta n_B}\right)}\right\}
\end{aligned} \tag{B.42}$$

$$
\begin{aligned}
I_L \sim & \frac{1}{4jkh}\left(2+\frac{1}{1-\frac{1}{\Delta n_B}}+\frac{1}{1+\frac{1}{\Delta n_B}}\right)-\frac{e^{-j\pi\Delta n_B}}{4jk\left(h+\frac{\lambda}{2}\Delta n_B\right)}\left(2+\frac{e^{+j\pi}}{1-\frac{1}{\Delta n_B}}+\frac{e^{-j\pi}}{1+\frac{1}{\Delta n_B}}\right) \\
= & \frac{1}{4jkh}\left\{2+\frac{2}{1-\left(\frac{1}{\Delta n_B}\right)^2}\right\}-\frac{e^{-j\pi\Delta n_B}}{4jkh\left(1+\frac{\pi\Delta n_B}{kh}\right)}\left\{2-\frac{2}{1-\left(\frac{1}{\Delta n_B}\right)^2}\right\} \qquad \text{(B.43)}
\end{aligned}
$$

$$
\begin{aligned}
\kappa = & \frac{I_0}{I_\infty} \\
= & jkhI_0 \\
= & \frac{1}{4}\left\{2+\frac{2}{1-\left(\frac{1}{\Delta n_B}\right)^2}\right\}-\frac{e^{-j\pi\Delta n_B}}{4\left(1+\frac{\pi\Delta n_B}{kh}\right)}\left\{2-\frac{2}{1-\left(\frac{1}{\Delta n_B}\right)^2}\right\} \qquad \text{(B.44)}
\end{aligned}
$$

(B.44) shows that

- The absolute value of κ is always more than 1.
- The absolute value of κ takes the local minimum when Δn_B is an odd integer number (Note that $\Delta n_B \geq 2$ is already assumed).
- The imaginary part of κ becomes 0 when Δn_B is an integer number. That is, the phase of κ in terms of a complex number becomes 0.
- As h gets larger for an fixed odd integer number of Δn_B, κ goes to 1.
- As Δn_B gets larger for a fixed value of h, κ goes to 1.